



Karlsruhe Institute of Technology

Karlsruhe Institute of Technology

Department of Chemical and Process Engineering

Engler-Bunte-Institute

Division of Combustion Technology

MASTER'S THESIS

Effect of stretch on the burning velocity of laminar and turbulent premixed flames

by

— *Thorsten Zirwes* —

Advisor: Dr.-Ing. Feichi Zhang

Reviewer: Prof. Dr.-Ing. Henning Bockhorn

July 29, 2016

Ich versichere wahrheitsgemäß, die Arbeit selbstständig angefertigt, keine anderen als die angegebenen Quellen und Hilfsmittel benutzt zu haben, die wörtlich oder inhaltlich übernommenen Stellen als solche kenntlich gemacht zu haben und die Satzung des Karlsruher Instituts für Technologie zur Sicherung guter wissenschaftlicher Praxis beachtet zu haben.

July 29, 2016
(Thorsten Zirwes)

Abstract

Steady and unsteady laminar premixed methane/air and hydrogen/air plane-jet flames with different equivalence ratios ranging from fuel-lean to fuel-rich are investigated under atmospheric conditions using DNS with detailed molecular transport and chemistry. The objective is to gain a deeper understanding of the influence of unsteady and nonuniform stretching on flame propagation.

A nonuniform velocity profile used at the inlet leads to a stretched flame. For steady-state flames, consumption speeds, flame stretch, curvature, strain and Markstein numbers are evaluated. By increasing the mass flow rate at the inlet, the flames become longer and different Markstein numbers are obtained.

The inflow is then harmonically excited with different frequencies and the flames oscillate in the unsteady flow. For these unsteady flames, flame relaxation times are evaluated from the phase shift between the movement of the flame and the fluid flow velocity at the flame surface. The amplitude of the flame front movement is attenuated with increasing frequency and chemical time scale. Also, the phase shift between the movement of the flame and the local flow field becomes larger with increasing frequency or chemical time scale. Due to the flame relaxation time, different Markstein numbers are obtained from different phase angles within one oscillation period. Time averaged and frequency dependent Markstein numbers are computed which become smaller with decreasing frequency. This behavior can be reproduced by a power function in dependence on the Damköhler number.

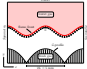
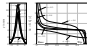
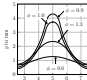

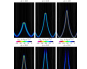
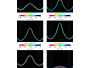
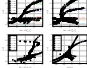

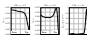

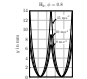
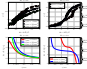
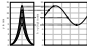

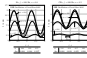
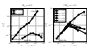
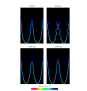
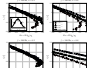
Contents


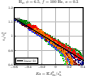
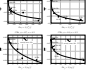
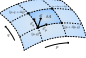

	Page
1 Introduction	1
1.1 Motivation	1
1.2 Objectives	2
1.3 Outline	3
2 Flame-Turbulence Interaction	4
2.1 Flames in Laminar Flows	4
2.2 Flames in Turbulent Flows	5
2.3 Local Flame Speeds	9
2.3.1 Unstretched Laminar Flame Speed	9
2.3.2 Displacement Speed	10
2.3.3 Consumption Speed	14
2.4 Flame Stretch	16
2.4.1 Lewis Number	18
2.4.2 Markstein Number	19
2.4.3 Flame Stretch in Turbulent Flows	22
3 Simulation of Turbulent Flames	25
3.1 Modeling of Turbulent Premixed Combustion	25
3.2 Direct Numerical Simulation	27
3.3 Implementation Details	27
3.3.1 Governing Equations	28
3.3.2 Thermodynamic Properties	30
3.3.3 Transport Properties	30
3.3.4 Chemical Source Terms	33
4 Steady-State Flames	37
4.1 Numerical Setup	37
4.1.1 Computational Domain and Boundary Conditions	37
4.2 Choice of Setup	40
4.3 Results	40

5	Oscillating Flames	51
5.1	Numerical Setup	51
5.2	Flame Relaxation Times	51
5.3	Unsteady Markstein Numbers	57
6	Summary and Outlook	61
6.1	Summary	61
6.2	Outlook	62
	Appendix A Derivation of Stretch	63
A.1	Geometric Derivation of Stretch	63
A.2	Reynolds Transport Theorem	69
A.3	Volume Element Analogy	74
	Appendix B Reaction Mechanisms	77
B.1	Hydrogen Mechanism by Li et al.	77
B.2	Methane Mechanism by Kee et al.	78
	Bibliography	80

List of Figures

1.1		World energy production	1
2.1		Schematic drawing of a laminar premixed Bunsen flame	4
2.2		Schematic drawing of a turbulent premixed Bunsen flame	6
2.3		Normalized flame speed over turbulent area growth	7
2.4		Turbulent flame speed over turbulent fluctuations	8
2.5		Unstretched laminar flame speed	9
2.6		Spherically expanding flame	11
2.7		Displacement speed at the tip of a Bunsen flame	13
2.8		Extrema of displacement speeds	13
2.9		Illustration of stretch	16
2.10		Mechanisms leading to stretch	17
2.11		Laminar flame speeds of methane/air over equivalence ratio	19
2.12		Lewis number effect	20
2.13		DNS results of flame speed and stretch	22
2.14		Turbulent flame speed in dependence on turbulent fluctuations	23

4.1		Computational domain and boundary conditions	38
4.2		Hydrogen flame shapes and stretch	41
4.3		Methane flame shapes	41
4.4		Normalized stretch rates along the flame surface	42
4.5		Hydrogen reaction rates	44
4.6		Methane reaction rates	45
4.7		Correlations for consumption speeds of hydrogen flames	46
4.8		Correlations for consumption speeds of methane flames	47
4.9		Local equivalence ratios along the flame surface	48
4.10		Markstein numbers for methane and hydrogen	49
4.11		Shapes of hydrogen flames for different mass flow rates	49
4.12		Effect of different mass flow rates	50
5.1		Movement of the flame during oscillation	52
5.2		Oscillations of different flames for fixed amplitudes	53
5.3		Oscillations of different flames for a fixed frequency	54
5.4		Flame relaxation times over Damköhler numbers	55
5.5		Unstable flame behavior for high frequencies	56
5.6		Flame speed for different phase angles for rich hydrogen	57

5.7		Flame speed for different phase angles for lean hydrogen	58
5.8		Exmample for the computation of mean Markstein numbers	59
5.9		Averaged Markstein numbers	60
A.1		Surface local coordinate system	63
A.2		Visualization of the Reynolds transport theorem	71

List of Tables

4.1 Boundary conditions 39

4.2 Parameters for the methane and hydrogen flames 39

Introduction

Combustion is the most important source for energy production. Over 80 % of the world's primary energy consumption is supplied by burning fossil fuels [14]. More than 65 % of the world's electricity is generated by combustion [43]. Because of the high energy density of hydrocarbon fuels, combustion is the main power source in transportation. Many industrial processes, like the production of metals, ceramics or cement, rely on high temperatures generated by combustion [92].

1.1 Motivation

Over the next decades, improving the efficiency of combustion processes will be more important than ever. British Petroleum predicts that in the next 20 years global energy demand will increase by 34 % as a result of the growing world population. In 2035, 80 % of the global energy will be supplied by burning fossil fuels (Figure 1.1). Oil will still provide the bulk of transport fuels with 88 % [14]. At the same time, regulations regarding the emission of greenhouse gases and other toxic products are becoming more and more restrictive. In 2014, EU leaders agreed to new energy targets for the year 2030.

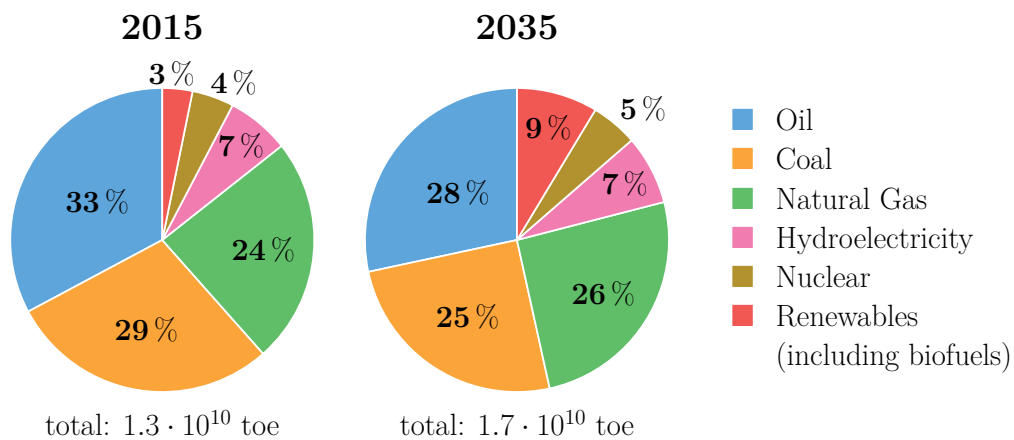


Figure 1.1: World energy production in tonnes of oil equivalent (toe) [14].

These include improving the overall energy efficiency by 27 % and reducing greenhouse gas emissions to 40 % of the emission levels of 1990 [25]. To meet the increasing energy demands while fulfilling the goals set to slow down climate change, combustion processes have to become cleaner and more efficient. For example, the thermal efficiencies of internal gasoline combustion engines used in automobiles only range from 10 % to 25 % [88]. Another for improving improve the efficiency of combustion processes arises from the limited fossil fuel resources. In many sectors, the cost of fuels is a limiting factor too. In aviation, the cost of fuels make up more than 35 % of airlines' expenses. This might further increase in the future when the prices for oil rise as oil from remaining reserves becomes more difficult to extract [70].

These challenges demonstrate that more research is needed to gain a deeper understanding of combustion processes in order to generate energy more efficiently in the future. In the last decades, numerical simulations in the field of Computational Fluid Dynamics (CFD) have proven to be an effective way of studying combustion processes. They help to optimize existing processes and enable the development of new technologies.

1.2 Objectives

Most technical combustion processes take place in turbulent flows [71]. The interaction of the turbulent flow field and a flame plays an important role for the efficiency of combustion processes and is still not fully understood [75]. Experimental investigation of these processes is often very time and cost intensive because of extreme conditions like high temperatures and pressures. Additionally, the small time and length scales in turbulent combustion make direct measurements difficult [51].

An alternative to experimental investigation of turbulent flames is Direct Numerical Simulation (DNS). It is a simulation technique where the full range of time and length scales is resolved, making it possible to study the fundamental interactions between turbulence and flames in a way that experiments cannot achieve [75]. Because of the accurate resolution of the flow and the detailed modeling of complex chemical reactions, DNS requires very high computational resources which has only been made possible in the last few decades with the increasing computational power of supercomputers [56]. The results and insights gained from DNS help to understand the underlying physical phenomena and can be used to improve simulation techniques which save most of the computational requirements by simplifying the way turbulence and combustion is modeled [51] (see chapter 3).

The focus of this work is to study the effect of flame stretch and unsteady velocity fluctuations on local burning velocities. In turbulent flows the flame surface is stretched due to flow inhomogeneities. This alters the structure of the flame locally and thereby local flame speeds [75]. First, stationary flames are simulated to investigate the general effect of

stretch in steady-state flows. The influence of stretch on the local flame dynamics, like reaction rates, is investigated and the influence of different stretch contributions, like strain and curvature, on flame speeds are evaluated. To study the effect of unsteady stretching, the previously investigated steady-state flames are excited by harmonically oscillating flows. Correlations of stretch and local flame speeds from the unsteady flames are compared to the steady-state flames, flame relaxation times are evaluated and time averaged Markstein numbers are computed to describe the frequency dependency of local burning velocities on stretch.

1.3 Outline

Chapter 2 presents the theoretical basics of the interaction of turbulence and combustion with respect to local flame speeds. Different definitions of flame speed are discussed, the concept of flame stretch is introduced and the Lewis and Markstein numbers are explained.

Chapter 3 gives a brief overview of simulation techniques used to simulate turbulent flames. The focus lies on the description of direct numerical simulation of combustion processes. Steady-state flames are investigated in chapter 4. The correlation of stretch and flame speed is evaluated by computing Markstein numbers of fuel-lean and fuel-rich hydrogen and methane flames.

In chapter 5, the steady-state flames from the previous chapter are harmonically excited. The effect of unsteady stretching is demonstrated by averaging instantaneous Markstein numbers over different phase angles to obtain an effective Markstein number. The results of this thesis are summarized in chapter 6 with an outlook for future work.

Flame-Turbulence Interaction

This chapter gives a short introduction to the characteristics of turbulent flows and how they interact with premixed flames. Important quantities that are used throughout this thesis—like flame speed and flame thickness—are defined. The chapter ends with an overview of the concept of flame stretch and its effects on laminar and turbulent flames and shows examples of modeling approaches found in the literature.

2.1 Flames in Laminar Flows

On the left of Figure 2.1, a Bunsen-type flame is shown schematically. The flow coming from the burner is laminar and consists of premixed fuel and oxidizer, leading to a conically shaped flame. The ratio of fuel and oxidizer in the unburnt mixture can be described by the equivalence ratio ϕ which is the ratio of the oxidizer mass fraction Y_{O_x} and fuel mass fraction Y_F at stoichiometric conditions (st) divided by the mass fraction ratio of the

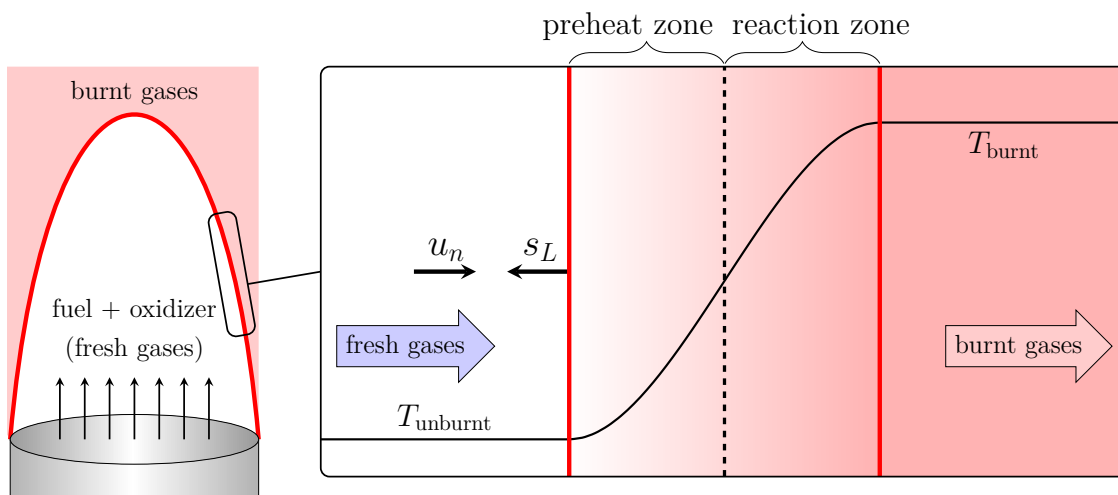


Figure 2.1: Schematic drawing of a laminar premixed Bunsen flame (left) and temperature profile in the flame front (right). The flame moves with the flame speed s_L toward the fresh gases, which move with u_n .

actual mixture:

$$\phi \equiv \frac{(Y_{Ox}/Y_F)_{st}}{Y_{Ox}/Y_F} \quad (2.1)$$

Flames where fuel and oxidizer are not mixed before combustion (diffusion flame) are not in the scope of this thesis.

In premixed flames, chemical reactions take place in a thin reaction zone. On the right of Figure 2.1, the profile of temperature T normal to the flame front is shown schematically. As the fuel/oxidizer mixture from the burner passes through the flame front, its temperature increases due to the heat released in the reaction zone from the unburnt temperature T_{unburnt} to the exhaust temperature T_{burnt} . The characteristic length scale of a flame is the flame thickness δ , often defined to be the thickness of the reaction zone. In this thesis, flame thickness is always calculated in terms of the thermal thickness δ_{th} [75]:

$$\delta_{th} \equiv \frac{\max(T) - \min(T)}{\max(|\frac{\partial T}{\partial n}|)} \quad (2.2)$$

where $\frac{\partial T}{\partial n}$ is the temperature gradient inside the flame front in its normal direction.

If the flame is in steady state, it burns with the same speed s_L toward the fresh gases as it is convected away by the flow with u_n , which is the gas velocity of the fresh gases normal to the flame front. The burning velocity or flame speed s_L is a measure of how fast the flame propagates against the fresh gas (for more details about the local flame speed s_L see section 2.3). Flame speeds are an important quantity because they can be used to predict the length of a flame, how much heat can be released and if flash-backs can occur [75]. The chemical time scale or flame transit time τ_c is defined by

$$\tau_c \equiv \delta/s_L \quad (2.3)$$

It is the characteristic time scale of a flame.

2.2 Flames in Turbulent Flows

Turbulence is characterized by a broadband of fluctuations of the fluid velocity. In turbulent flows, large eddies are generated which break down in size until they dissipate their kinetic energy into heat (energy cascade). The characteristic length scale of the large, energy carrying eddies is the integral length scale L_t . The smallest eddies reach the Kolmogorov length η before dissipating. The interaction of these eddies of different sizes, energies and rotational frequencies leads to the fluctuations observed in turbulent flows. These fluctuations are generally described statistically by the root mean squared of the velocity fluctuations u' [89].

In turbulent combustion, eddies stretch the flame front leading to an increase in flame

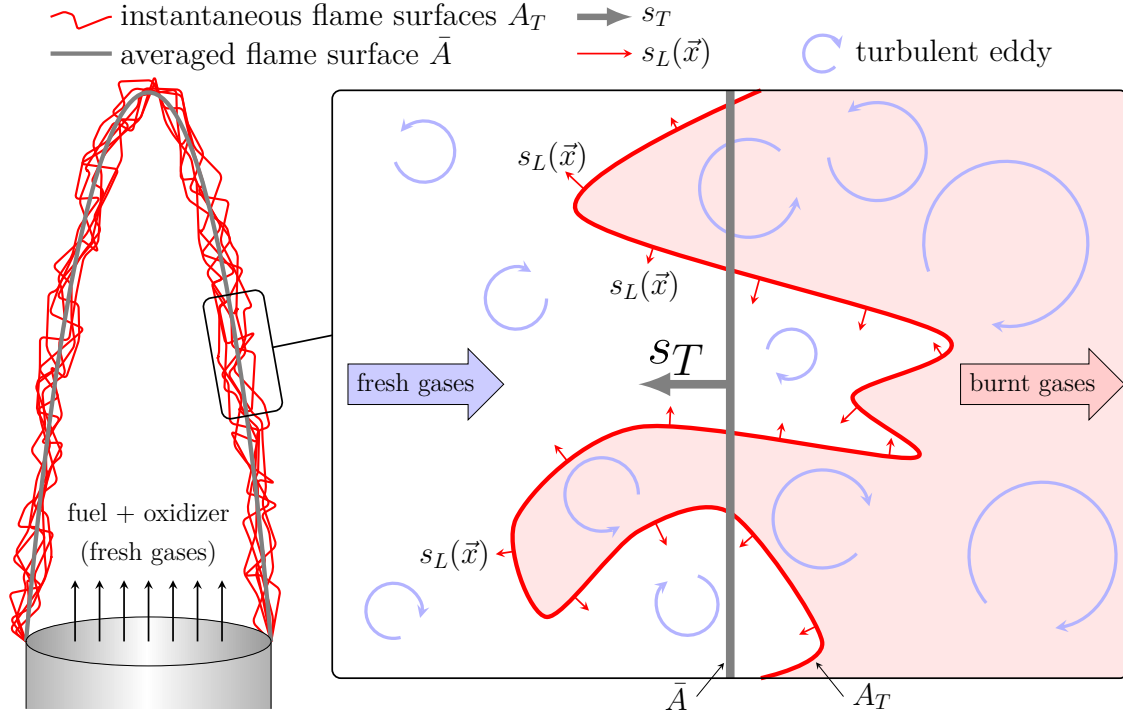


Figure 2.2: Schematic drawing of a turbulent premixed Bunsen flame.

surface area compared to a laminar flame and therewith an increased volumetric heat production. Together with the fact that turbulent fluctuations enhance the mixing of chemical reactants, this is the reason why most technical combustion processes take place in turbulent flows [71].

A turbulent Bunsen flame is depicted schematically on the left of Figure 2.2. The turbulent flow distorts the flame front so that at each moment in time the instantaneous flame surfaces have different shapes. Compared to the laminar Bunsen flame in Figure 2.1 the flame fronts are unsteady and irregularly wrinkled [26]. As eddies pass through the flame front (on the right of Figure 2.2), they deform the flame front. In general, the flame thickness and flame speeds $s_L(\vec{x})$ are different at each point \vec{x} on the flame front because each element on the flame front experiences different stretch rates [59] (see section 2.3 and section 2.4).

In most simulations the instantaneous flame fronts A_T and their thickness are not resolved in order to save computing time. Instead, the flame is described by an averaged flame surface \bar{A} which propagates with an integral velocity s_T . To compute the correct consumption of fuel with regards to conservation of mass, the turbulent flame speed s_T is introduced [75]:

$$\rho^u Y_F^u s_T \bar{A} = \rho^u Y_F^u \bar{s}_L A_T \quad (2.4)$$

where Y_F^u is the mass fraction of the fuel and ρ^u the density of the unburnt gas. The

amount of fuel passing through the averaged area \bar{A} with the speed s_T must be the same as the fuel passing through the area A_T with \bar{s}_L on the unburnt side of the flame front. Because s_T describes an integral consumption rate of chemical reactants, it is used in many combustion models [71]. The area averaged local flame speed \bar{s}_L is [95]:

$$\bar{s}_L = \frac{1}{A_T} \int_{A_T} s_L(\vec{x}) dA \quad (2.5)$$

Eq. (2.4) can be rearranged to [57]:

$$\frac{s_T}{\bar{s}_L} = \frac{A_T}{\bar{A}} \quad (2.6)$$

If the increase in surface area A_T/\bar{A} and the average local flame speed \bar{s}_L are known, the turbulent flame speed can be calculated.

Combustion models, like the flame surface density model, provide models for A_T/\bar{A} which is called wrinkling factor [75]. But because the influence of turbulent fluctuations on the local flame speeds is still not fully understood [57, 59], \bar{s}_L is often assumed to be the flame speed of an unstretched, laminar flame s_L^0 and therefore constant:

$$\frac{s_T}{s_L^0} \approx \frac{A_T}{\bar{A}}, \quad s_L^0 = \text{const} \quad (2.7)$$

However, experiments [57, 59, 95] have shown that in general $\bar{s}_L \neq s_L^0$. It depends not only on the fuel type and equivalence ratio ϕ , but also on the flow conditions. Figure 2.3 shows experimental data of spherically expanding turbulent flames. The assumption of

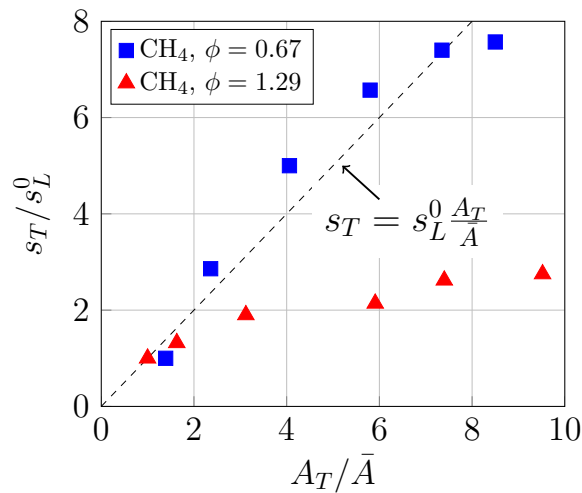


Figure 2.3: Normalized turbulent flame speed over turbulent area growth from experimental measurements of turbulent spherically expanding flames [94, 95].

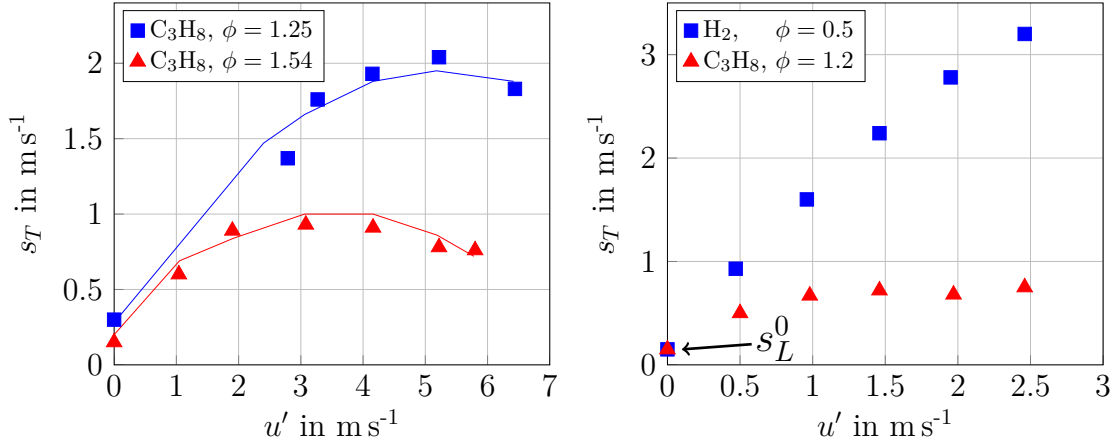


Figure 2.4: Turbulent flame speed over turbulent fluctuation intensity. Continuous lines are fits to the experimental data [45, 59, 67].

$s_T \approx s_L^0$ is approximately valid for fuel-lean mixtures of methane CH_4 at $\phi = 0.67$ (■) but not for fuel-rich mixtures at $\phi = 1.29$ (▲). As the flow becomes more turbulent and A_T increases, s_T does not increase linearly with A_T/\bar{A} because \bar{s}_L is also a function of the turbulent fluctuations.

Other experiments where the turbulent flame speed is measured for different turbulent fluctuation intensities show similar results. On the left of Figure 2.4, the turbulent flame speed increases as the flow becomes more turbulent. However, for very high u' , the turbulent flame speed decreases [57, 59, 94]. Because the flame surface does not decrease substantially even for high u' , the decrease of s_T is caused by the decreasing local flame speed \bar{s}_L [95].

On the right of Figure 2.4, two different fuels, hydrogen H_2 (■) and propane (▲), with the same laminar flame speed s_L^0 were measured. Although they have the same laminar flame speed, their turbulent flame speeds behave very differently as the flow becomes more turbulent. Simple models [2, 75], like

$$s_T \approx s_L^0 + u' \quad (2.8)$$

fail to reproduce these effects. Other models derived from dimensional analysis, like the relation proposed by Borghi [7]

$$s_T \approx s_L^0 Re_T \frac{\delta^0}{L_t}, \quad Re_T = \frac{u' L_t}{\nu} \quad (2.9)$$

where Re_T is the turbulent Reynolds number and ν the kinematic viscosity, or the Schmid model [79] derived from asymptotic theory

$$s_T \approx s_L^0 + u' \left(1 + Da_t^{-2}\right)^{-\frac{1}{4}} \quad (2.10)$$

where Da_t is the turbulent Damköhler number [75, 79], compute the turbulent flame speed without taking variable local flame speeds into account. Therefore, the results from Figure 2.4 cannot be reproduced by them. Empirical correlations [8] exist too, which include thermo-physical properties of the flame via the Lewis number Le (see subsection 2.4.1):

$$s_T \approx 0.88 u' \left(0.157 \frac{u'}{s_L^0} Da_t^{-\frac{1}{2}} Le \right)^{-0.3} \quad (2.11)$$

Other empiric models [71] need to be adjusted to the specific setup used in the experiment

$$s_T \approx s_L^0 + s_L^0 C \left(\frac{u'}{s_L^0} \right)^n \quad (2.12)$$

where C and n are model parameters.

2.3 Local Flame Speeds

Until now, local flame speeds were denoted by s_L . In practice, local flame speeds in simulations have to be computed from one of two methods: from the consumption of a chemical species or energy within the flame front, yielding the consumption speed s_c , or from the movement of the flame surface resulting in the displacement speed s_d [42, 75]. As described above, s_L (which may be s_c or s_d) is often assumed to be the flame speed of unstretched laminar flames s_L^0 . In the next subsections, the unambiguously defined unstretched flame speed s_L^0 is explained and two general methods of computing local flame speeds in terms of s_d and s_c are described.

2.3.1 Unstretched Laminar Flame Speed

Unstretched laminar flame speed s_L^0 is an important reference parameter for the characterization of flames [71]. It is the speed at which a flame front moves relative to the fresh gas flow. It is uniquely defined for flames that are planar (no curvature), unstretched (uniform

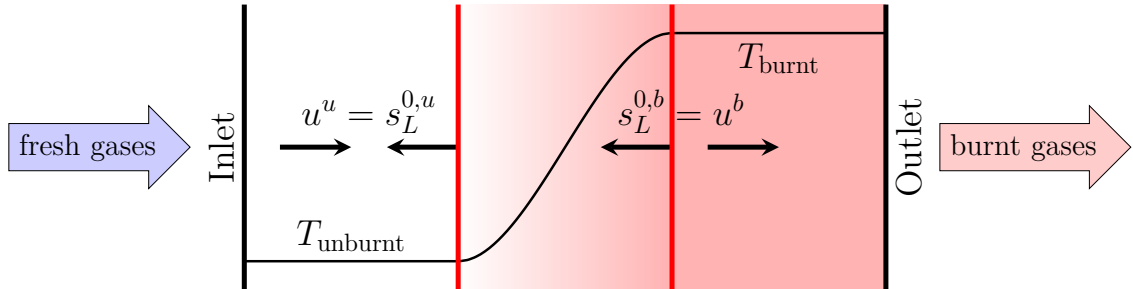


Figure 2.5: Unstretched laminar flame speed relative to the unburnt and burnt gases.

laminar flow field) and in steady state. In this case, all points on the flame surface move with the same velocity. It is the only case where the local flame speed is unambiguous [56] and the same if expressed as displacement speed s_d or consumption speed s_c (see following subsections). In Figure 2.5, a common setup for computing laminar unstretched flame speeds s_L^0 is depicted: a one-dimensional flame (in Cartesian coordinates) is placed in a laminar flow. The inlet velocity is adjusted so that the flame moves with the same speed toward the fresh gases as it is convected away by the flow. As the gas passes through this stationary flame front it accelerates due to thermal expansion. The laminar flame speed can be defined to be equal to the inlet velocity $s_L^0 \equiv s_L^{0,u} = u^u$ or to the burnt gas velocity at the outlet $s_L^0 \equiv s_L^{0,b} = u^b$. Because of conservation of mass, unburnt and burnt gas velocities can be computed from

$$u^u \rho^u = \rho^b u^b \quad (2.13)$$

where ρ^u is the density of the unburnt gas and ρ^b the density of the burnt gas. In this thesis, the unstretched laminar flame speed is always measured relative to the unburnt mixture $s_L^0 \equiv s_L^{0,u}$.

2.3.2 Displacement Speed

In general, flame fronts are not stationary so that the method described above cannot be used to determine local flame speeds. An obvious method is to measure the absolute velocity of the flame surface \vec{w} and the fluid velocity \vec{u} . Because the flame speed is the relative movement of the flame to the flow, the local flame speed can be computed in terms of the displacement speed s_d from [75]:

$$s_d = (\vec{w} - \vec{u}) \cdot \vec{n} = \vec{w} \cdot \vec{n} - \vec{u} \cdot \vec{n} \quad (2.14)$$

where \vec{n} is the unit normal vector of the flame surface pointing towards the fresh gases. For example in Figure 2.5, the absolute velocity of the flame is $\vec{w} \cdot \vec{n} = 0$ because the flame front is stationary. Therefore, on the fresh gas side the displacement speed is:

$$s_d^u = \vec{w} \cdot \vec{n} - \vec{u} \cdot \vec{n} = 0 - (u^u (-1)) = u^u = s_L^0 \quad (2.15)$$

For a spherically expanding flame, the absolute velocity of the flame $\vec{w} \cdot \vec{n}$ can be measured in terms of the temporal change of the flame radius r_f :

$$\vec{w} \cdot \vec{n} = \frac{dr_f}{dt} \quad (2.16)$$

The fluid velocity at the burnt side of the flame front is zero (see Figure 2.6). Therefore,

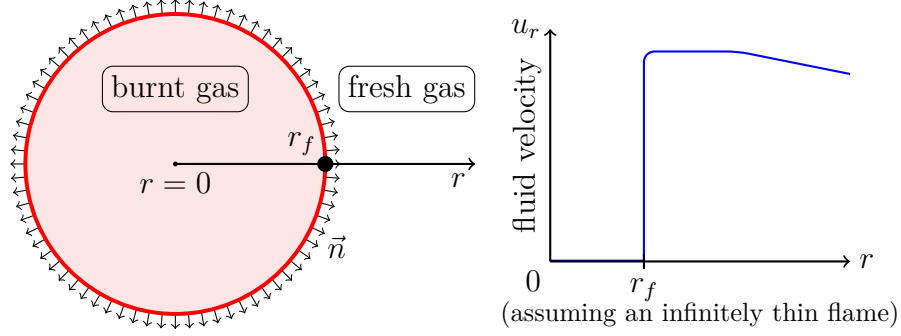


Figure 2.6: Idealized spherically expanding flame.

the displacement speed at the burnt side of the flame front s_d^b becomes:

$$s_d^b = \vec{w} \cdot \vec{n} - \vec{u} \cdot \vec{n} = \frac{dr_f}{dt} - 0 = \frac{dr_f}{dt} \quad (2.17)$$

The displacement speed in relation to the unburnt gases s_d^u can be approximated via the density change throughout the flame front, leading to the density weighted displacement speed s_d^* :

$$s_d^u \approx s_d^* = \frac{\rho^b}{\rho^u} \frac{dr_f}{dt} \quad (2.18)$$

In simulations, the displacement speed can be determined in terms of the normal component of the velocity of an iso-surface representing the flame front. If the flame front is defined by an iso-surface of the scalar field φ at the value φ_{iso} , the displacement speed at that iso-surface is [34]:

$$s_d(\varphi_{\text{iso}}) = \pm \left(\frac{1}{|\nabla\varphi|} \frac{D\varphi}{Dt} \right)_{\varphi=\varphi_{\text{iso}}} \quad (2.19)$$

$\frac{D\varphi}{Dt}$ is the substantial derivative of the quantity φ and the sign is positive, if the spatial gradient of φ is negative from the unburnt to the burnt side of the flame (like for the fuel concentration), and the sign is negative if ϕ increases from the unburnt to the burnt side (for example temperature). Defining the flame front by an iso-surface of the mass fraction of the fuel species $\varphi = Y_F$ allows to simplify the expression for the displacement speed. The substantial derivative in Eq. (2.19) can be replaced by the conservation of species mass (also see Eq. (3.4)):

$$\rho \frac{DY_F}{Dt} = \dot{\omega}_F + \nabla \cdot (\rho D_{m,F} \nabla Y_F) \quad (2.20)$$

where $\dot{\omega}_F$ is the reaction rate of the fuel, ρ the density and $D_{m,F}$ the diffusion coefficient

of the fuel into the mixture. Together with the definition of the surface unit normal vector

$$\vec{n} = \left(\frac{\nabla Y_F}{|\nabla Y_F|} \right)_{Y_F=Y_{F,\text{iso}}} \quad (2.21)$$

the displacement speed can be developed into [27, 71]:

$$s_d(Y_{F,\text{iso}}) = \underbrace{-\frac{\dot{\omega}_F}{\rho|\nabla Y_F|}}_{\text{chemical reaction}} \underbrace{-D_{m,F}\kappa}_{\text{tangential diffusion}} \underbrace{-\frac{1}{\rho|\nabla Y_F|}\frac{\partial}{\partial n}\left(\rho D_{m,F}\frac{\partial Y_F}{\partial n}\right)}_{\text{normal diffusion}} \quad (2.22)$$

where $\kappa = \nabla \cdot \vec{n}$ is the curvature of the flame surface. Eq. (2.22) has the advantage that the influence of chemical reactions and the diffusion of fuel in the normal and tangential direction of the flame surface on the displacement speed can be studied separately.

There are some drawbacks when computing local flame speeds s_L in terms of displacement speeds. One of the main drawbacks is that the displacement speed depends on the choice of iso-surface [18, 57]. Because the displacement speed is measured relative to the flow velocity, it increases as the flow accelerates due to thermal expansion. To relate the displacement speed at a specific iso-surface to the unburnt gas velocity, the density weighted displacement speed s_d^* is generally used [19]:

$$s_d^* = s_d(\varphi_{\text{iso}}) \frac{\rho(\varphi_{\text{iso}})}{\rho^u} \neq s_d(\varphi^u) = s_d^u \quad (2.23)$$

But as explained further below (on the right of Figure 2.8), the density weighted displacement speed s_d^* is not always equal to the displacement speed measured at iso-surfaces at the unburnt gas s_d^u . This has been shown in numerical simulations of spherically expanding flames [35]. For highly stretched flames, this discrepancy can be large [56]. Because the flame has a finite thickness, there is no obvious choice which iso-surface best captures the behavior of the flame. This makes it hard to compare experimental data where the exact position within the flame front might be unknown.

Because the displacement speed measures the speed of an abstract mathematical iso-surface, it has no clear physical meaning. This is illustrated by the range of values s_d can assume. For example, consider the stationary laminar Bunsen flame in Figure 2.7. Because the flame is stationary, its surface does not move so that the absolute moving speed $\vec{w} \cdot \vec{n}$ is zero. The highest fluid velocities u_{max} are at the tip. At the unburnt side of the flame front the displacement speed becomes:

$$s_d^u = (\vec{w} \cdot \vec{n} - \vec{u} \cdot \vec{n}) = 0 - (u_{\text{max}}(-1)) = u_{\text{max}} \quad (2.24)$$

As long as the flame burns stably, the velocity u_{max} in the burner can be increased

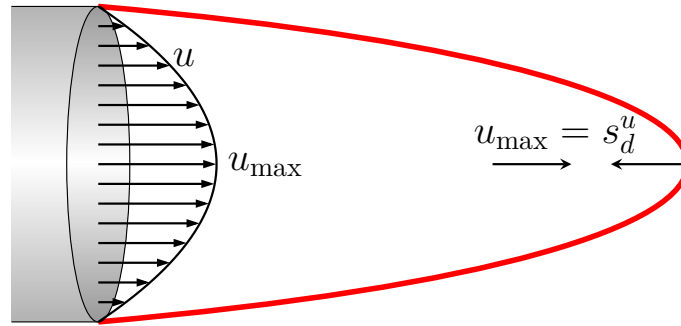


Figure 2.7: The displacement speed at the tip of a stationary Bunsen flame is equal to the maximum of the fluid velocity on the unburnt side of the flame.

so that arbitrarily high displacement speeds can be achieved. In numerical simulations, displacement speeds of $s_d \approx 8s_L^0$ have been achieved for this setup [73,75]. Another example where very high displacement speeds appear is when two flame fronts merge and form a cusp (on the left of Figure 2.8). As the two surfaces move toward each other, the point at the tip of the cusp appears to move with very high speeds (in some cases up to $20s_L^0$ [72]) while the surfaces merge.

In contrast to this, there are several situations where displacement speeds can become negative, which has less meaning in the context of flame speeds. If a flame is locally quenched and no chemical reactions take place, there is still a mass fraction gradient and therewith an iso-surface of the fuel mass fraction representing the flame front. At those locations the displacement speed is not zero but may be negative [57]. Similarly, in highly stretched flames the diffusive terms in Eq. (2.22) can become larger than the (positive) reaction term due to high concentration gradients [18,56], resulting in negative displacement speeds.

Another example for negative displacement speeds is changing flame thickness. If the

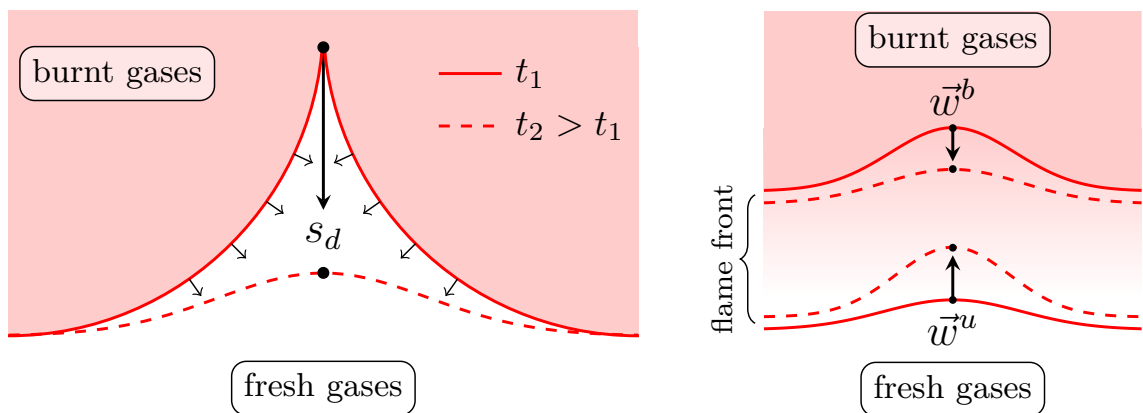


Figure 2.8: Merging of two flame fronts (left) leading to very high displacement speeds at the tip and changing flame thickness (right) resulting in negative displacement speed [72].

flame thickness stays constant over time, each iso-surface within the flame front moves with the same absolute speed $\vec{w} \cdot \vec{n}$ since the flame thickness can be defined by the distance between iso-surfaces near the burnt and unburnt side. Due to high stretching however, the flame front can change its thickness. By definition, the displacement speed is negative if $(\vec{w} - \vec{u}) \cdot \vec{n} < 0$. On the right of Figure 2.8, an iso-surface near the unburnt side moves with \vec{w}^u and an iso-surface near the burnt side moves with \vec{w}^b . Not only is $\vec{w}^u \neq \vec{w}^b$ but they also have opposite sign because they move toward each other, decreasing the thickness of the flame front. Depending on which iso-surface is chosen to represent the flame front, negative displacement speeds can appear. This is often observed in DNS [18, 72]. Because different iso-surfaces do not move with the same absolute velocity \vec{w} , the normalized displacement speed at an arbitrary iso-surface is not the same as the displacement speed of an iso-surface at the unburnt side of the flame ($s_d^* \neq s_d^u$). This makes it hard to use displacement speeds because they differ not only along the flame front but also at different layers within it.

2.3.3 Consumption Speed

The consumption speed measures the speed of a flame in terms of the consumption of chemical reactants or energy [57]. This is derived for the consumption of fuel below. Consider the case of the unstretched one-dimensional flame in Figure 2.5. In general, the conservation of species mass for the fuel is:

$$\rho \frac{\partial Y_F}{\partial t} + \rho \vec{u} \cdot \nabla Y_F = \nabla \cdot (\rho D_{m,F} \nabla Y_F) + \dot{\omega}_F \quad (2.25)$$

where the mass diffusion is formulated in a Fick-like way (see also Eq. (3.4)). For the one-dimensional Cartesian case, this becomes:

$$\rho u \frac{\partial Y_F}{\partial x} = \frac{\partial}{\partial x} \left(\rho D_{m,F} \frac{\partial Y_F}{\partial x} \right) + \dot{\omega}_F \quad (2.26)$$

where the time derivative is zero because the flame is in steady state. Integrating this over the whole domain yields:

$$\int_{-\infty}^{+\infty} \rho u \frac{\partial Y_F}{\partial x} dx = \int_{-\infty}^{+\infty} \frac{\partial}{\partial x} \left(\rho D_{m,F} \frac{\partial Y_F}{\partial x} \right) dx + \int_{-\infty}^{+\infty} \dot{\omega}_F dx \quad (2.27)$$

Because of conservation of mass, ρu is constant in this setup so that the integrals reduce to:

$$\rho u [Y_F]_{-\infty}^{+\infty} = \underbrace{\left[\rho D_{m,F} \frac{\partial Y_F}{\partial x} \right]_{-\infty}^{+\infty}}_{=0} + \int_{-\infty}^{+\infty} \dot{\omega}_F dx \quad (2.28)$$

At $x = -\infty$ is the unburnt gas and at $x = +\infty$ the burnt gas. Because no gradients exist at the boundaries, $\frac{\partial}{\partial x} = 0$ and the diffusion term vanishes. Choosing $\rho u = \rho^u u^u = \rho^u s_c$ yields:

$$\rho^u s_c (Y_F^b - Y_F^u) = \int_{-\infty}^{+\infty} \dot{\omega}_F dx \quad (2.29)$$

In general, this integration has to be performed normal to the flame surface so that the general definition of consumption speed is [56]

$$s_c \equiv -\frac{1}{\rho^u (Y_F^u - Y_F^b)} \int_{-\infty}^{+\infty} \dot{\omega}_F dn \quad (2.30)$$

where dn is the direction normal to the flame surface. Therefore, the consumption speed has to be computed for each point on the flame surface by integrating along a line in the normal direction. Only for the unstretched, one-dimensional flame used in this derivation, $s_c = u^u = s_d^* = s_L^0$ is true [75].

The consumption speed has some advantages over the displacement speed. Because it is determined by integrating over the whole flame thickness in the flame normal direction, only one value of s_c exists at each point along the flame front. It is therefore not sensitive to the choice of iso-surface [75]. Consumption speeds generally cannot become negative because the integral in Eq. (2.30) is always greater or equal to zero. At points where the flame is locally quenched and no reactions take place, the consumption speed becomes zero.

As shown above, displacement speeds at the tip of a stationary Bunsen flame can be an order of magnitude higher than s_L^0 . In the same simulation of the stationary Bunsen flame (Figure 2.7) where the displacement speed at the tip was found to be $8s_L^0$ [75], the local consumption speed was still $s_c \approx s_L^0$ which is expected for flames which are insensitive to curvature and stretch ($Le \approx 1$ and $Ma \approx 0$, see the next sections). The reason for this discrepancy can be explained by considering the different terms in the balance equation for the mass fraction of the fuel (see Eq. (3.4)): As the inflow velocity rises, the convective term becomes larger. This is not balanced by reaction rates, since this flame is insensitive to stretch, but instead by the diffusive fluxes in the tangential direction, due to the high curvature (see Section 2.4.1 and Chapter 4). Because the diffusive flux is not considered in the computation of s_c in Eq. (2.30), $s_c \approx s_L^0$. As explained above, $s_d \gg s_L^0$ due to the geometric constraint $\vec{w} \cdot \vec{n} = \vec{u} \cdot \vec{n} + s_d = 0$ for this steady-state flame and the high diffusive fluxes causing a value of s_d that is much larger than s_c .

Because the consumption speed measures the consumption rate of fuel, it has a clear physical meaning and is more useful for combustion modeling than the displacement speed [75]. The surface averaged local flame speed \bar{s}_L in Eq. (2.5) was introduced to compute the turbulent flame speed s_T . Because s_c directly measures the consumption of fuel it should be used to compute local flame speeds s_L . However, consumption speeds

cannot be measured experimentally [75]. In general, the integration in Eq. (2.30) has to be performed over a limited distance so that no other parts of the flame are crossed. This has to be taken into account in highly wrinkled flames [91].

2.4 Flame Stretch

Karlovitz [44] identified flame stretch as the main influence on local flame dynamics. Flame stretch \mathbb{K} is defined as the logarithmic change of surface area of a surface area element A [97]:

$$\mathbb{K} \equiv \frac{1}{A} \frac{dA}{dt} \quad (2.31)$$

Each surface element on the surface of a flame experiences different stretching based on the local flow conditions. The area of a surface element on the flame front changes only if points on the surface move with different velocities \vec{w} . In Figure 2.9 points on the surface move in different directions with different speeds leading to an increase in area of the surface element spanned by them. Therefore, stretch can also be expressed as the divergence on the surface of the absolute velocity \vec{w} [78]:

$$\mathbb{K} = \nabla_t \cdot \vec{w} \quad (2.32)$$

where ∇_t is the gradient along the flame surface in its tangential direction.

By splitting the absolute velocity into its components tangential and normal to the

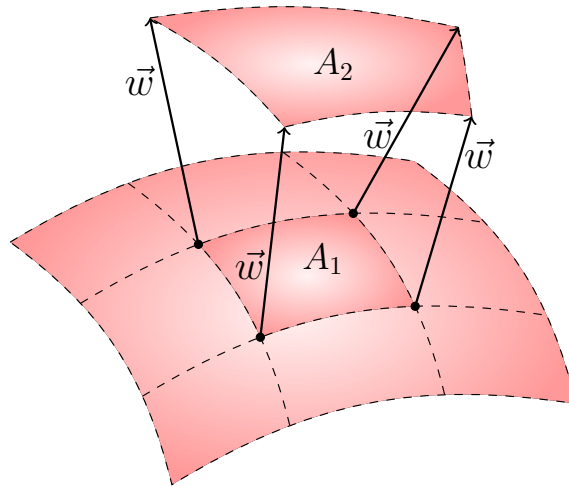


Figure 2.9: Points along the surface move with different velocities \vec{w} , leading to an increase in surface area ($A_2 > A_1$).

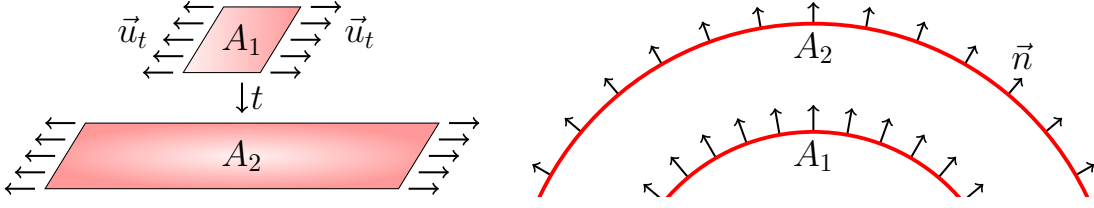


Figure 2.10: Mechanisms leading to stretch: tangential stretching \mathbb{K}_t (left) and normal stretching \mathbb{K}_n (right), both increasing the flame surface over time ($A_2 > A_1$).

surface $\vec{w} = \vec{w}_t + \vec{w}_n$, the stretch from Eq. (2.32) can be developed into [22]:

$$\mathbb{K} = \nabla_t \cdot \vec{w} = \nabla_t \cdot \vec{w}_t + \nabla_t \cdot \vec{w}_n = \underbrace{\nabla_t \cdot \vec{u}_t}_{\mathbb{K}_t} + \underbrace{(\vec{u} \cdot \vec{n} + s_d)}_{\mathbb{K}_n} \kappa \quad (2.33)$$

\vec{u}_t is the fluid velocity in the tangential direction of the flame surface and κ the flame front curvature. In this way, the two mechanisms leading to an increase in flame surface area and thereby stretch are

- stretching tangential to the surface \mathbb{K}_t
- and the movement of a curved surface in its normal direction \mathbb{K}_n .

On the left of Figure 2.10, the fluid velocity tangential to the surface \vec{u}_t pulls a planar flame apart causing tangential straining \mathbb{K}_t . On the right, a positively curved flame moves normal to itself with the overall velocity $\vec{u} \cdot \vec{n} + s_d$ (\mathbb{K}_n) which results in the total normal stretch \mathbb{K}_n and an increase in flame surface area.

Stretch can also be split into the influence of the fluid velocity gradients \mathbb{K}_s and the flame propagation of a curved flame \mathbb{K}_c . Because the movement of the flame is caused by the convection with the fluid flow \vec{u} and the flame's own propagation in the normal direction $s_d \vec{n}$, the absolute velocity of a flame is [56]:

$$\vec{w} = \vec{u} + s_d \vec{n} \quad (2.34)$$

By substituting Eq. (2.34) into Eq. (2.32) the flame stretch can be expressed as [16]:

$$\mathbb{K} = \nabla_t \cdot \vec{w} = \nabla_t \cdot (\vec{u} + s_d \vec{n}) = \underbrace{\nabla_t \cdot \vec{u}}_{\mathbb{K}_s} + \underbrace{s_d \kappa}_{\mathbb{K}_c} \quad (2.35)$$

\mathbb{K}_c is the stretch due to curvature κ and flame propagation s_d . \mathbb{K}_s is the aerodynamic strain rate due to fluid velocity gradients [49, 50]. Note that \mathbb{K}_s implicitly contains the flame curvature κ (compare Eq. (2.33) and 2.35). Eq. (2.35) demonstrates that stretch in terms of the change of surface area in Eq. (2.31) is caused by velocity gradients along the flame surface and the flame propagation itself. The aerodynamic strain rate \mathbb{K}_s is

connected to the strain rate tensor $\mathbf{S} = \text{symm}(\nabla\vec{u})$ by

$$\mathbb{K}_s = (\mathbf{I} - \vec{n}\vec{n}) : \mathbf{S} \quad (2.36)$$

where \mathbf{I} is the unit tensor [56]. The aerodynamic strain rate \mathbb{K}_s is often referred to in the literature as a_T [57]. Note that the flame speed in Eq. (2.34) and Eq. (2.33) is the displacement speed s_d measured at the same surface for which the stretch is computed. It is neither the density weighted displacement speed s_d^* nor the consumption speed s_c or unstretched laminar flame speed s_L^0 .

By its definition, the concept of flame stretch is only applicable to (two-dimensional) surfaces. However, flames have a non-zero flame thickness. The choice of iso-surface representing the flame can affect the stretch rates because velocity gradients, curvature and the absolute movement velocity $\vec{w} = \vec{u} \cdot \vec{n} + s_d$ of the iso-surface can vary throughout the flame front, especially for highly stretched flames [10, 56]. This has to be taken into account when discussing stretch rates.

2.4.1 Lewis Number

Flames react very differently to stretch depending on the fuel type and equivalence ratio. Increasing stretch may increase local flame speeds, decrease them or have no effect at all [57, 81]. An indicator of how a flame reacts to stretching is the Lewis number Le [57]:

$$Le \equiv \frac{a}{D} \quad (2.37)$$

a is the thermal diffusivity and D the diffusion coefficient of the deficient species, both usually evaluated for unstretched flames in the unburnt mixture. In the context of flame stretch it is useful to define the deficient species relative to the maximum of the unstretched laminar flame speed s_L^0 [51, 94] which is a function of the equivalence ratio ϕ (see Figure 2.11). For $\phi < \phi(s_{L,\max}^0)$, the deficient specie is the fuel and for $\phi > \phi(s_{L,\max}^0)$ it is oxygen O_2 . For most flames, the maximum of the unstretched flame speed is approximately at stoichiometric conditions so that the deficient species is fuel for $\phi < 1$ and oxygen for $\phi > 1$.

The Lewis number compares how fast heat is conducted away from the flame and chemical reactants diffuse toward it. The Lewis number effect is illustrated for a curved and stretched flame in Figure 2.12. On the left (case **a** for $Le > 1$), heat \vec{q} (big blue arrows) diffuses faster than reactants \vec{j} (small red arrows) because $a > D$. At the positively curved base of the flame ($\nabla \cdot \vec{n} > 0$, $\mathbb{K} > 0$), heat flux is defocused ($\nabla \cdot \vec{q}$) leading to an increased heat loss compared to a planar flame, and at the negatively curved tip ($\nabla \cdot \vec{n} < 0$, $\mathbb{K} < 0$) heat flux is focused ($\nabla \cdot \vec{q}$) so that less heat is conducted away than in a planar flame. Because the positively curved base loses more heat, local flame speeds are decreased ($s_L \downarrow$) whereas at the negatively curved top local flame speeds are increased ($s_L \uparrow$) [52, 75].

If $Le < 1$ (case **b** and **c**), the flame is instead controlled by mass diffusion. At the base, mass flux (big blue arrows) is focused ($\nabla \cdot \vec{j} < 0$) and at the tip defocused ($\nabla \cdot \vec{j} > 0$). The local flame speeds depend on preferential diffusion: if the diffusion coefficient of the deficient specie is greater than the diffusion coefficient of the abundant specie, more of the deficient specie reaches the base, shifting the equivalence ratio locally towards higher flame speeds. Otherwise, the abundant specie is further enriched at the base, leading to decreased flame speeds [57,94]. At the tip, the faster diffusing specie is spread over a larger area and thereby local equivalence ratios are shifted toward leaner conditions if $D_F > D_{O_2}$ and richer conditions if $D_F < D_{O_2}$. Depending on the equivalence ratio of the fresh gas mixture ϕ , this leads to an increase or decrease of local flame speeds. For $Le \approx 1$ the flame is insensitive to curvature and stretch.

The Lewis number effect also explains thermo-diffusive instabilities [57]. In case **a** of Figure 2.12, the local flame speeds at the tip are higher than at the base. Therefore, the tip moves faster downward than the base so that their relative distance becomes smaller over time. This flame front tends to form a smooth surface with less wrinkles so that this case is stable. In case **b** for $D_F > D_{O_2}$ and in case **c** for $D_F < D_{O_2}$, the base moves faster than the tip, thereby increasing the distance between them over time, leading to a more wrinkled flame (unstable).

2.4.2 Markstein Number

A simplified model that describes the dependency of flame speed on stretch is given by the linear Markstein model [23,62]. A first order Taylor expansion for the flame speed of a stretched flame $s_L(\mathbb{K})$ around the flame speed of an unstretched flame $s_L^0 \equiv s_L(\mathbb{K} = 0)$

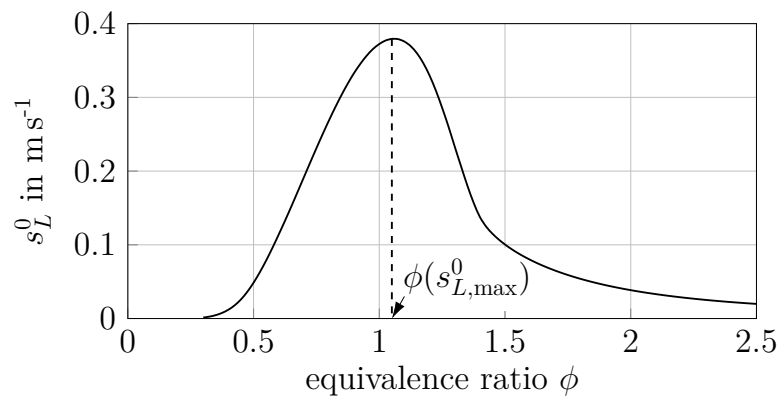


Figure 2.11: Unstretched laminar flame speed s_L^0 as a function of equivalence ratio ϕ computed for methane/air at atmospheric conditions.

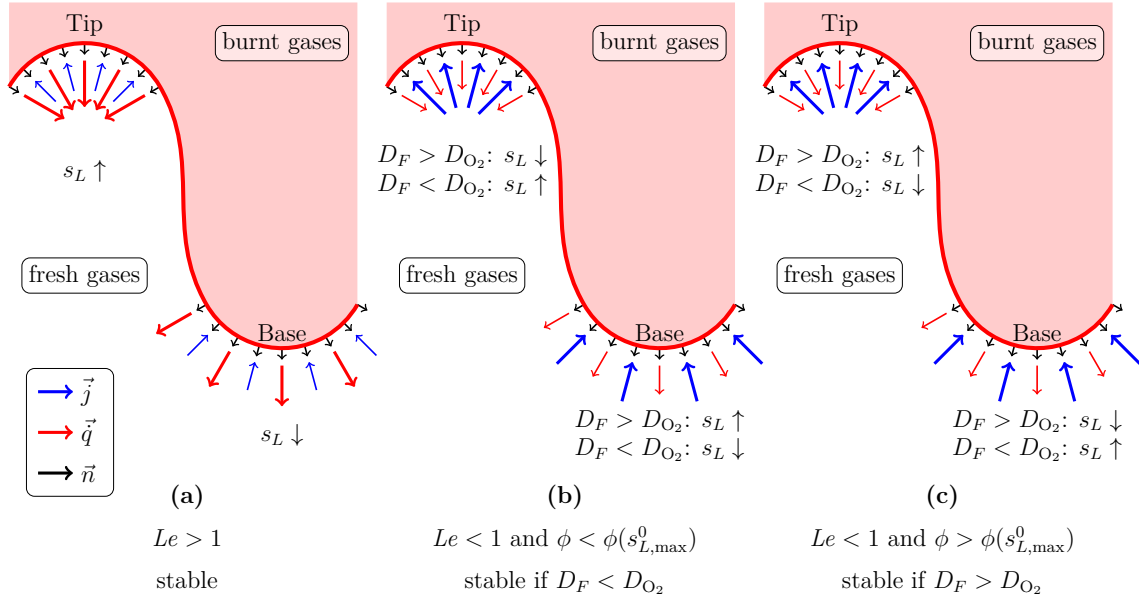


Figure 2.12: Effect of the Lewis number Le in terms of heat flux \vec{q} (\rightarrow) and mass flux \vec{j} (\rightarrow) leading to an increase ($s_L \uparrow$) or decrease ($s_L \downarrow$) of local flame speeds.

yields [56]:

$$s_L(\mathbb{K}) \approx s_L^0 + \left. \frac{\partial s_L}{\partial \mathbb{K}} \right|_{\mathbb{K}=0} (\mathbb{K} - 0) \quad (2.38)$$

The dependency (or sensitivity) of flame speed to stretch is summarized in the Markstein length \mathcal{L} :

$$\mathcal{L} \equiv -\frac{\partial s_L}{\partial \mathbb{K}} \quad (2.39)$$

Substituting the Markstein length in Eq. (2.38), one obtains:

$$s_L(\mathbb{K}) \approx s_L^0 - \mathcal{L}\mathbb{K} \quad (2.40)$$

Dividing by s_L^0 and expanding the product on the r.h.s. by a flame thickness δ^0 yields:

$$\frac{s_L(\mathbb{K})}{s_L^0} \approx 1 - \frac{\mathcal{L}}{\delta^0} \frac{\mathbb{K}\delta^0}{s_L^0} \quad (2.41)$$

Markstein length divided by flame thickness δ^0 is the non-dimensional Markstein number Ma :

$$Ma \equiv \frac{\mathcal{L}}{\delta^0} = -\frac{1}{\delta^0} \frac{\partial s_L}{\partial \mathbb{K}} \quad (2.42)$$

and the non-dimensional flame stretch is the Karlovitz number Ka :

$$Ka \equiv \frac{\mathbb{K}\delta^0}{s_L^0} \quad (2.43)$$

With these characteristic numbers, the linear Markstein correlation becomes [60]:

$$\frac{s_L(\mathbb{K})}{s_L^0} \approx 1 - Ma Ka \quad (2.44)$$

As shown in subsection 2.4.1, in unstable flames local flame speeds increase with stretch. The resulting Markstein number from Eq. (2.42) is therefore negative. For stable flames, Ma is positive [57].

Because a first order Taylor approximation is used in the derivation of the linear Markstein model, it is only valid for small stretch rates. This linear correlation can also be derived from asymptotic theory by assuming single-step chemistry, constant heat capacities, high activation energy and small stretch [75]. Additionally, flame speed is assumed to be only a function of the overall flame stretch \mathbb{K} . In reality, \mathbb{K}_c and \mathbb{K}_s from Eq. (2.35) have different effects on flame speed, especially for highly stretched flames [24, 56, 57, 75], so that the Markstein model can be extended for small stretch to [56]

$$\frac{s(\mathbb{K}_c, \mathbb{K}_s)}{s_L^0} \approx 1 - Ma_c Ka_c - Ma_s Ka_s = 1 - Ma_c \frac{\delta^0}{s_L^0} s_d \kappa - Ma_s \frac{\delta^0}{s_L^0} \nabla_t \cdot \vec{u} \quad (2.45)$$

It has also been shown that spatial gradients of stretch $\frac{\partial \mathbb{K}_{s/c}}{\partial s}$ along the flame coordinate s [56, 57, 99] and the temporal change of stretch $\frac{\partial \mathbb{K}_{s/c}}{\partial t}$ [31, 56, 57] influence the flame speeds too. However, using different Markstein numbers for Ka_s and Ka_c is impractical because they often cannot be measured separately.

There are also non-linear models to describe the effect of stretch on flame speeds derived from asymptotic theory or experimental fits. However, most of the non-linear Markstein models are only applicable to spherical flames [20, 37, 37, 87, 98], which are only positively curved and stretched and have no tangential velocity components u_t .

Different methods used to determine Markstein numbers yield different values. There are many definitions of flame thickness (i.e. global, thermal, diffusive) [75], which yield different thickness values. Markstein numbers depend on the choice of using flame speeds measured relative to the burnt s_L^b or unburnt gas s_L^u and the choice of iso-surface used to compute stretch and flame speeds as explained above. Different iso-surfaces used to evaluate stretch and flame speed can even lead to Markstein numbers with opposite sign in highly stretched flames [35, 57, 90]. Furthermore, Markstein numbers of consumption and displacement speeds can differ by a lot as explained in section 2.3. If not stated otherwise, Markstein and Karlovitz numbers in this thesis are calculated for consumption speeds s_c , non-dimensionalized with the thermal flame thickness δ_{th}^0 from Eq. (2.2) and computed at the iso-surface of fuel mass fraction corresponding to the maximum heat release $Y_{F,q_{\max}}^0$ in unstretched flames.

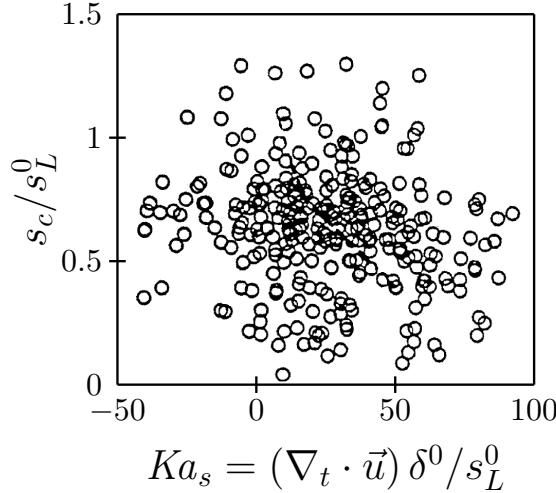


Figure 2.13: Normalized local consumption speeds s_c over normalized local aerodynamic strain rates obtained from DNS of turbulent hydrogen/air flames at $\phi = 0.5$ [4].

2.4.3 Flame Stretch in Turbulent Flows

As shown in section 2.2 in Figure 2.3, local flame speeds of turbulent flames depend on the unsteady flow conditions. Additionally, simulations have shown that points on a turbulent flame front experiencing the same instantaneous flame stretch \mathbb{K} can have different flame speeds. This results in a scattering of data when plotting local flame speeds against local stretch rates [18, 19, 30], as shown in Figure 2.13 [4].

It has been observed that flames react differently to unsteady stretching than to steady stretch [38, 51, 57]. There is also an effect of the time history (memory effect [57]). For example, in flows oscillating with high frequencies the motion of the flame is attenuated because the flame cannot adjust itself fast enough to the changing flow conditions [51]. Simulations and experiments [15, 21, 32, 48, 65, 85, 86] have shown that oscillating stretch rates, which temporarily exceed stretch rates that would lead to extinction in steady-state flames, do not extinguish the flame. The reason is that the flame has not enough time to relax to a state where the high stretch rates quench the flame [51]. In turbulent flames, this response time is difficult to study because the flame is subjected to a broad-band frequency spectrum.

The effect of the Lewis number (see subsection 2.4.1) is qualitatively found in turbulent flames too: turbulent flame speeds s_T of unstable flames with $Le < 1$ increase with increasing turbulent fluctuations u' more than stable flames with $Le > 1$ [57] (see Figure 2.14). The reason for this can be seen from the definition of turbulent flame speed in Eq. (2.6):

$$s_T = \bar{s}_L \frac{A_T}{A} \quad (2.46)$$

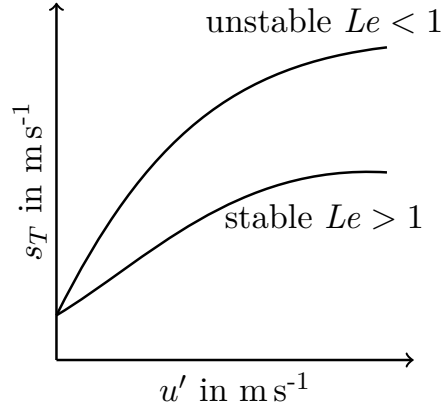


Figure 2.14: Qualitative behavior of turbulent flame speed s_T with turbulent velocity fluctuations u' [57]. In stable flames with $Le > 1$, s_T increases more slowly with u' than in unstable flames with $Le < 1$, although both flames have the same laminar flame speed s_L^0 .

Turbulent fluctuations lead to an increase in flame surface area A_T/\bar{A} and therewith an increase of s_T for both stable and unstable flames. Because the flame surface area is always increased in turbulent flows, the average stretch rate $\mathbb{K} \equiv 1/A \, dA/dt$ is positive too. For unstable flames, the local flame speed \bar{s}_L increases with positive stretch, increasing the turbulent flame speed s_T further. For stable flames ($Le > 1$) and positive stretch, the local flame speed \bar{s}_L is decreased so that s_T increases more slowly with u' and A_T/\bar{A} .

In order to include variable local flame speeds in simulations, the efficiency factor I_0 has been introduced [11]:

$$I_0 \equiv \frac{\bar{s}_L}{s_L^0} \quad (2.47)$$

If the flame is stable ($Le > 1$, $Ma > 0$), local flame speeds are decreased by positive stretch rates so that $I_0 < 1$. For unstable flames ($Le < 1$, $D_{\text{deficient}}/D_{\text{abundant}} > 1$ and $Ma < 0$), $I_0 > 1$ [59]. I_0 can be computed from [8, 75, 78]

$$I_0 = \frac{1}{s_L^0} \int_{-\infty}^{+\infty} s_L(\mathbb{K}) P(\mathbb{K}) \, d\mathbb{K} \quad (2.48)$$

where $P(\mathbb{K})$ is the probability density function of stretch on the turbulent flame surface. Analogously to Eq. (2.45), this can be extended to [12]:

$$I_0 = \frac{1}{s_L^0} \int_{-\infty}^{+\infty} \int_{-\infty}^{+\infty} s_L(\mathbb{K}_c + \mathbb{K}_s) P(\mathbb{K}_c) P(\mathbb{K}_s) \, d\mathbb{K}_c \, d\mathbb{K}_s \quad (2.49)$$

Simulations and experiments have shown that the average curvature and therewith \mathbb{K}_c of a turbulent flame front is close to zero. Because the overall stretch rate is positive in turbulent flows, the average straining \mathbb{K}_s is positive [10]. The probability density functions are not known in general, but fits to experimental data of methane/air flames with $Le > 1$

exist [1, 10, 75]:

$$I_0 \approx 0.117 \frac{\rho^b}{\rho^u} \left(0.157 \left(\frac{u'}{s_L^0} \right)^2 Re_T^{-\frac{1}{2}} \right)^{-0.784} \quad (2.50)$$

If a linear correlation is assumed similar to the liner Markstein model in subsection 2.4.2, the average local flame speed can be computed from [95]:

$$\frac{\bar{s}_L}{s_L^0} \approx 1 - \int_{-\infty}^{+\infty} Ma P(Ka) dKa \approx 1 - IMa_{lam} Ka_{mean} \quad (2.51)$$

where $P(Ka)$ is the probability density function of the Karlovitz number, Ka_{mean} is the mean turbulent Karlovitz number, Ma_{lam} the Markstein number obtained from the laminar flame and IMa_{lam} is the effective Markstein number of the turbulent flame.

Simulation of Turbulent Flames

In the field of Computational Fluid Dynamics (CFD) many methods have been developed to simulate turbulent flows and model the chemistry of combustion processes. The first section in this chapter gives a short overview of simulation methods and models currently used to simulate turbulent premixed flames. The second section describes the technique of Direct Numerical Simulation and includes a comprehensive description of the implementation of the DNS solver used in this work.

3.1 Modeling of Turbulent Premixed Combustion

The most widely used approaches for simulating turbulent flows are RANS (Reynolds-Averaged Navier-Stokes Equations) and LES (Large Eddy Simulation) [75]. Both techniques solve an averaged flow so that the turbulent fluctuations in the fluid field do not have to be resolved down to the smallest time and length scales in order to save computing time.

In RANS simulations the turbulent flow is averaged over time. Turbulent fluctuations increase the transport of mass, momentum and energy in the flow (see section 2.2). This is modeled by increasing the viscosity and other diffusive properties where high gradients in the averaged velocity, energy or species concentration fields are present.

LES does not average the flow field temporally but spatially. Thereby, larger vortices are fully resolved and a transient flow can be simulated. Smaller eddies are not resolved and their effect is modeled similarly to RANS simulations. Because the flow is resolved at the length scales of larger eddies containing most of the turbulent kinetic energy, LES is more accurate than RANS but also more computationally expensive.

In addition to turbulence modeling, combustion is simulated using simplifying models too when conducting RANS or LES. This is done because on one hand a lot of different chemical species are involved in the chemical process of combustion. For example, detailed reaction mechanisms of iso-octane [64] include over 850 chemical species and about 4000 different reactions. Because a conservation equation has to be solved for each species and thermodynamical and transport properties have to be computed for each species, this

would add very high computing times compared to the solution of the flow in RANS or LES. On the other hand systems of differential equations including reaction rates are very numerically stiff: species concentrations and chemical time scales can differ by over ten orders of magnitude [46] and the chemical reaction rates are highly non-linear because they depend exponentially on temperature. Therefore, special integration methods have to be utilized to solve them efficiently and stably. Also, the thin reaction zone of flames, where most of the reactions take place, has to be resolved spatially which is not possible using coarse computational grids.

Due to the high computational costs of including detailed chemistry, many combustion models have been developed to avoid the problems mentioned above. For an overview of the different combustion models, see for example Poinso et al. [75]. Some models reduce the whole chemical system to just a single reaction and thicken the flame artificially (Thickened Flame Models), others assume that as soon as fuel and oxygen are mixed they are burned instantly (infinitely fast chemistry) and that the chemistry is governed only by the time needed to mix fuel and oxidizer through turbulent fluctuations (Eddy Breakup Model). Diffusive fluxes are sometimes simplified by assuming that all chemical species and energy diffuse with the same speeds (unity Lewis number). Flamelet models like the Flamelet Generated Manifold (FGM) model precompute one-dimensional flames and embed them in turbulent flows allowing to compute the chemistry beforehand and store the results into look-up tables. The effect of turbulent fluctuations can then be captured, for example, with probability density functions which account for the averaging performed by RANS and LES. Another model, the G-Equation, assumes the flame to be infinitely thin and solves a kinematic equation for the flame surface. In flame surface density models, a transport equation for the increase in flame surface area is solved which provides the turbulent burning velocity in terms of flame surface area growth.

Because the interaction of the turbulent flow and the flame is still not fully understood, many combustion models do not include the effect of flame stretch on local burning velocities [75]. For example, in flamelet approaches like FGM the chemistry is often precomputed for laminar and unstretched flames and Turbulent Flame Speed Closure Models often assume the local burning velocities to be constant and not dependent on stretch or use empirical models (see Eq. (2.8) – Eq. (2.12)) so that effects like local extinction cannot be reproduced correctly [57]. More research is needed to understand the influence of turbulent stretching on local burning velocities to improve existing combustion models.

3.2 Direct Numerical Simulation

Turbulence and combustion models cannot be used to investigate the fundamental interactions of flames and turbulent flows. Instead, detailed chemistry and transport as well as a fully resolved flow field are necessary [57, 75]. Direct Numerical Simulation (DNS) is a simulation technique where the full range of time and length scales of the flow and flame is resolved and the fluid flow is computed directly without using statistical models like in RANS or LES approaches. Additionally, a transport equation for each species is solved and detailed reaction mechanisms are used to account for all reactions and intermediate species relevant for the combustion so that there is no need for simplified chemistry approaches. This allows to study of the interaction of turbulent flows and flames in great detail down to the smallest time and length scales.

Because the smallest time and length scales of the flow and chemistry are resolved and for each chemical species a transport equations is solved including non-linear source terms and detailed diffusion for multicomponent mixtures, DNS is very computationally expensive. As high performance computers have become more powerful over the last decades, DNS has been made possible. But still, the high computational demands are the limiting factor, usually restricting DNS to problems with small physical dimensions. It is therefore important to optimize the performance of DNS codes and ensure good parallel scale-up to utilize the resources provided by supercomputers efficiently.

3.3 Implementation Details

In this thesis, all simulations are performed using DNS. The DNS solver was developed in 2012 at the Engler-Bunte Institute at the Karlsruhe Institute of Technology [6, 101]. It is implemented in the open-source code OpenFOAM [69, 96] and actively being developed especially with regards to performance [102]. It uses the Finite Volume Method to solve the fully compressible Navier-Stokes equations for reacting flows in a single gaseous phase, including the conservation of species masses and energy. The solver uses routines of the open-source library Cantera [36] to compute transport properties derived from rigorous kinetic gas theory and chemical source terms using an operator splitting technique. The advantages of the solver are:

- Unstructured grids for complex geometries.
- Fully compressible formulation of the governing equations.
- Detailed reaction mechanisms and thermo-physical properties derived from rigorous kinetic gas theory.

- Highly optimized routines of Cantera and Sundials [83] for chemistry and transport properties.
- Sundials is the only external dependency.
- Chemical source terms are computed using an operator splitting technique, leading to higher accuracy and lower computing times.
- Built-in parser for Cantera's robust and flexible `xml` format for reaction mechanisms.
- Excellent parallel performance and scalability with well over 10,000 CPU cores on different architectures [101, 102].

A comprehensive list of the methods implemented to simulate the fluid flow and combustion is given in the following section.

3.3.1 Governing Equations

The governing equations (assuming ideal gases and perfect mixtures) are implemented as follows [75]:

- Conservation of total mass:

$$\frac{\partial \rho}{\partial t} + \nabla \cdot (\rho \vec{u}) = 0 \quad (3.1)$$

ρ is the density, t time and \vec{u} the fluid velocity.

- Conservation of momentum:

$$\frac{\partial (\rho \vec{u})}{\partial t} + \nabla \cdot (\rho \vec{u} \vec{u}) = -\nabla p + \nabla \cdot \boldsymbol{\tau} + \rho \vec{g} \quad (3.2)$$

p is the pressure, \vec{g} the gravitational acceleration. The viscous stress tensor $\boldsymbol{\tau}$ is computed for a Newtonian fluid using the Stokes assumption:

$$\boldsymbol{\tau} = \mu \left(\nabla \vec{u} + (\nabla \vec{u})^T - \frac{2}{3} \mathbf{I} \nabla \cdot \vec{u} \right) \quad (3.3)$$

where \mathbf{I} is the identity tensor and μ the dynamic viscosity.

- Conservation of species mass:

$$\frac{\partial (\rho Y_k)}{\partial t} + \nabla \cdot (\rho (\vec{u} + \vec{u}_c) Y_k) = \dot{\omega}_k - \nabla \cdot \vec{j}_k, \quad k = 1 \dots N - 1 \quad (3.4)$$

Y_k is the mass fraction of species k and $\dot{\omega}_k$ its reaction rate. N is the number of species. The correction velocity \vec{u}_c forces the sum of all diffusive fluxes \vec{j}_k to be zero:

$$\vec{u}_c = -\frac{1}{\rho} \sum_k \vec{j}_k \quad (3.5)$$

The diffusive mass flux is computed using a mixture-averaged model derived from the Stefan-Maxwell equations [46], neglecting pressure and temperature diffusion (Soret effect):

$$\vec{j}_k = -\rho D_{m,k} \nabla Y_k \quad (3.6)$$

$D_{m,k}$ is the diffusion coefficient of species k in the mixture.

- Conservation of energy: The transport of energy is formulated in terms of the total sensible enthalpy $h_s + \frac{1}{2} \vec{u} \cdot \vec{u}$:

$$\frac{\partial \left(\rho \left(h_s + \frac{1}{2} \vec{u} \cdot \vec{u} \right) \right)}{\partial t} + \nabla \cdot \left(\rho \vec{u} \left(h_s + \frac{1}{2} \vec{u} \cdot \vec{u} \right) \right) = -\nabla \cdot \vec{q} + \frac{\partial p}{\partial t} - \sum_k h_k^\circ \dot{\omega}_k \quad (3.7)$$

with

$$-\nabla \cdot \vec{q} = \underbrace{\nabla \cdot \left(\frac{\lambda}{c_p} \nabla h_s \right) - \sum_k \nabla \cdot \left(\frac{\lambda}{c_p} h_{s,k} \nabla Y_k \right)}_{=\nabla \cdot (\lambda \nabla T)} - \sum_k \nabla \cdot \left(h_{s,k} \hat{\vec{j}}_k \right) \quad (3.8)$$

λ is the heat conductivity of the mixture, c_p the isobaric heat capacity and T the temperature. Viscous work $\nabla \cdot (\boldsymbol{\tau} \cdot \vec{u})$, potential energy $\rho \vec{g} \cdot \vec{u}$, radiation and the Dufour effect are neglected. The sensible enthalpy $h_{s,k}$ of species k and the sensible enthalpy of the mixture h_s for ideal gases is

$$h_{s,k} = h_k - h_k^\circ, \quad h_s = \sum_k Y_k h_{s,k} \quad (3.9)$$

and $h_k^\circ \equiv h_k(298 \text{ K})$ is the enthalpy of formation of species k . The corrected diffusive mass flux $\hat{\vec{j}}_k$ is

$$\hat{\vec{j}}_k = \vec{j}_k - Y_k \sum_k \vec{j}_k \quad (3.10)$$

and Fourier's second law $\nabla \cdot (\lambda \nabla T)$ is rewritten (assuming ideal gases and that all species have the same temperature) in order to obtain the first term on the r.h.s. of Eq. (3.8), which can be discretized implicitly.

To close this system of partial differential equations, the relation of density, pressure and temperature is given by the equation of state for ideal gases:

$$\rho = \frac{p \bar{M}}{\mathcal{R} T} \quad (3.11)$$

where \bar{M} is the mean molar mass of the mixture and \mathcal{R} the universal gas constant.

Because the conservation of energy is formulated using sensible enthalpies, the temper-

ature has to be recovered from the enthalpy solution. After the energy equation is solved, the new enthalpies h_{CFD} are used to update the temperatures utilizing Newton's method:

$$T^{n+1} = T^n + \frac{h_{CFD} - h(T^n)}{c_p(T^n)} \quad (3.12)$$

3.3.2 Thermodynamic Properties

JANAF polynomials (also known as NASA polynomials) [63] are used to compute the specific molar enthalpy \tilde{h}_k , specific molar entropy \tilde{s}_k and specific molar isobaric heat capacity $\tilde{c}_{p,k}$ of each species k :

$$\frac{\tilde{c}_{p,k}}{\mathcal{R}} = a_{k,0} + a_{k,1}T + a_{k,2}T^2 + a_{k,3}T^3 + a_{k,4}T^4 \quad (3.13)$$

$$\frac{\tilde{h}_k}{\mathcal{R}T} = a_{k,0} + \frac{a_{k,1}}{2}T + \frac{a_{k,2}}{3}T^2 + \frac{a_{k,3}}{4}T^3 + \frac{a_{k,4}}{5}T^4 + \frac{a_{k,5}}{T} \quad (3.14)$$

$$\frac{\tilde{s}_k}{\mathcal{R}} = a_{k,0} \ln T + a_{k,1}T + \frac{a_{k,2}}{2}T^2 + \frac{a_{k,3}}{3}T^3 + \frac{a_{k,4}}{4}T^4 + a_{k,6} \quad (3.15)$$

Two sets of coefficients $a_{k,0} - a_{k,6}$ for a low and a high temperature range are read from the reaction mechanism file for each species. The mass specific values are computed from:

$$c_{p,k} = \frac{\tilde{c}_{p,k}}{M_k}, \quad h_k = \frac{\tilde{h}_k}{M_k}, \quad s_k = \frac{\tilde{s}_k}{M_k} \quad (3.16)$$

M_k is the molar mass of species k . The corresponding mixture properties are:

$$\bar{M} = \sum_k X_k M_k = \left(\sum_k \frac{Y_k}{M_k} \right)^{-1} \quad (3.17)$$

$$h = \sum_k Y_k h_k = \frac{1}{\bar{M}} \sum_k X_k \tilde{h}_k \quad (3.18)$$

$$c_p = \sum_k Y_k c_{p,k} = \frac{1}{\bar{M}} \sum_k X_k \tilde{c}_{p,k} \quad (3.19)$$

$X_k = Y_k \frac{\bar{M}}{M_k}$ is the mole fraction of species k .

3.3.3 Transport Properties

The transport properties (dynamic viscosity μ_k , heat conductivity λ_k and binary diffusion coefficients $\mathcal{D}_{k,i}$) for each species are calculated from the Chapman-Enskog solution of

kinetic gas theory [46, 76]:

$$\mu_k = \frac{5}{16} \frac{\sqrt{\pi M_k k_B T}}{\pi \sigma_k^2 \Omega_{kk}^{(2,2)*} \sqrt{N_A}} \quad (3.20)$$

$$\mathcal{D}_{k,i} = \frac{1}{p} \frac{3}{16 \pi \sigma_{i,k}^2 \Omega_{i,k}^{(1,1)*}} \sqrt{\frac{2 \pi k_B^3 T^3}{m_{i,k}}} \quad (3.21)$$

$$\lambda_k = \frac{\mu_k}{M_k} \left(f_{trans,k} \tilde{c}_{v,trans} + f_{rot,k} \tilde{c}_{v,rot,k} + f_{vib,k} \tilde{c}_{v,vib,k} \right) \quad (3.22)$$

k_B is the Boltzmann constant, N_A Avogadro's constant and σ_k is the Lennard-Jones collision diameter of species k . The reduced mass $m_{i,k}$, the reduced Lennard-Jones collision diameter $\sigma_{i,k}$ and the reduced Lennard-Jones well-depth $\epsilon_{i,k}$ of species i and k are computed from:

$$m_{i,k} = \frac{M_i M_k}{N_A (M_k + M_i)}, \quad \epsilon_{i,k} = \sqrt{\epsilon_i \epsilon_k} \xi^2, \quad \sigma_{i,j} = \frac{1}{2} (\sigma_i + \sigma_k) \xi^{-\frac{1}{6}} \quad (3.23)$$

where ϵ_k is the Lennard-Jones well-depth of the species k . The factor ξ is a correction for the interaction of polar and non-polar species. If both species i and k are polar (polarizability $\alpha_i > 0$ and $\alpha_k > 0$), or both species are non-polar ($\alpha_i = 0$ and $\alpha_k = 0$), ξ is unity. If one species is polar (species p) and the other is non-polar (species n), ξ [41, 54] is obtained with:

$$\xi = 1 + \frac{1}{4} \alpha_n^* \bar{\mu}_p^{*2} \sqrt{\frac{\epsilon_p}{\epsilon_n}}, \quad \alpha_n^* = \frac{\alpha_n}{\sigma_n^3}, \quad \bar{\mu}_p^* = \frac{\bar{\mu}_p}{\sqrt{\sigma_p^3 \epsilon_p}} \quad (3.24)$$

α_n is the polarizability of species n and $\bar{\mu}_p$ the dipole moment of species p . The collision integrals $\Omega_{i,k}^{(1,1)*}$ are calculated from the collision integrals $\Omega_{i,k}^{(2,2)*}$ as:

$$\Omega_{i,k}^{(1,1)*} = \frac{\Omega_{i,k}^{(2,2)*}}{A_{i,k}^*} \quad (3.25)$$

$A_{i,k}^*$ and $\Omega_{i,k}^{(2,2)*}$ are interpolated from tabulated values [51, 66] as a function of the reduced dipole moment $\delta_{i,k}^*$ and the reduced temperature $T_{i,j}^*$:

$$\delta_{i,k}^* = \frac{1}{2} \frac{\bar{\mu}_{i,k}^2}{\epsilon_{i,k} \sigma_{i,k}^3}, \quad \bar{\mu}_{i,k} = \sqrt{\bar{\mu}_i \bar{\mu}_k}, \quad T_{i,j}^* = \frac{k_B T}{\epsilon_{i,k}} \quad (3.26)$$

λ_i is computed using the parameters

$$f_{vib,k} = \frac{p \mathcal{D}_{k,k}}{\mu_k} \frac{M_k}{\mathcal{R}T}, \quad f_{trans,k} = \frac{5}{2} \left(1 - \frac{2}{\pi} \frac{\tilde{c}_{v,rot,k} A_k}{\tilde{c}_{v,trans} B_k} \right), \quad f_{rot,k} = f_{vib,k} \left(1 + \frac{2}{\pi} \frac{A_k}{B_k} \right) \quad (3.27)$$

$$A_k = \frac{5}{2} - f_{vib,k}, \quad B_k = Z_{rot,k} \frac{F_k(298\text{ K})}{F_k(T)} + \frac{2}{\pi} \left(\frac{5}{3} \frac{\tilde{c}_{v,rot,k}}{\mathcal{R}} + f_{vib,k} \right), \quad \tilde{c}_{v,trans} = \frac{3}{2} \mathcal{R} \quad (3.28)$$

$$F_k(T) = 1 + \frac{\pi^{\frac{3}{2}}}{\sqrt{T_k^*}} \left(\frac{1}{2} + \frac{1}{T_k^*} \right) + \left(\frac{\pi^2}{4} + 2 \right) \frac{1}{T_k^*}, \quad T_k^* = \frac{k_b T}{\epsilon_k} \quad (3.29)$$

$$\tilde{c}_{v,rot,k} = \begin{cases} 0, & \text{if mono-atomic} \\ \mathcal{R}, & \text{if linear} \\ \frac{3}{2} \mathcal{R}, & \text{otherwise} \end{cases}, \quad \tilde{c}_{v,vib,k} = -\tilde{c}_{v,rot,k} + \tilde{c}_{p,k} - \frac{5}{2} \mathcal{R} \quad (3.30)$$

where the last result is obtained from $\tilde{c}_v = \tilde{c}_{v,rot} + \tilde{c}_{v,vib} + \tilde{c}_{v,trans}$ and $\tilde{c}_v = \tilde{c}_p - \mathcal{R}$ (for ideal gases).

Because the calculation of the transport properties is computationally expensive, λ_k , $\mathcal{D}_{k,i}$ and $\sqrt{\mu_k}$ are calculated once at the start of the solver for 50 equidistant temperatures. The results are used to fit the coefficients of the following polynomials of the logarithmic temperature:

$$\lambda_k = \sqrt{T} \left(d_{k,0} + d_{k,1} \ln T + d_{k,2} \ln^2 T + d_{k,3} \ln^3 T + d_{k,4} \ln^4 T \right) \quad (3.31)$$

$$\mathcal{D}_{k,i} = \frac{1}{p} T^{\frac{3}{2}} \left(c_{ki,0} + c_{ki,1} \ln T + c_{ki,2} \ln^2 T + c_{ki,3} \ln^3 T + c_{ki,4} \ln^4 T \right) \quad (3.32)$$

$$\sqrt{\mu_k} = T^{\frac{1}{4}} \left(b_{k,0} + b_{k,1} \ln T + b_{k,2} \ln^2 T + b_{k,3} \ln^3 T + b_{k,4} \ln^4 T \right) \quad (3.33)$$

The species transport properties are computed using these functions at runtime. Because these polynomials are only a function of the temperature, the binary diffusion coefficients are actually fitted as $p\mathcal{D}_{k,i}$ to lose the pressure dependency (see Eq. (3.21)), so that the fitting polynomial in Eq. (3.32) has to be divided by the current pressure p .

The mixing rules for obtaining the properties of the gas mixture are [76]:

$$\mu = \sum_i \frac{\mu_i X_i}{\sum_k \Phi_{i,k} X_k}, \quad \Phi_{i,k} = \frac{\left(1 + \sqrt{\frac{\mu_i}{\mu_k} \sqrt{\frac{M_k}{M_i}}} \right)^2}{\sqrt{8 \left(1 + \frac{M_i}{M_k} \right)}} \quad (3.34)$$

$$\lambda = \frac{1}{2} \left(\sum_i X_i \lambda_i + \frac{1}{\sum_i \frac{X_i}{\lambda_i}} \right) \quad (3.35)$$

$$D_{m,k} = \left(\sum_{i \neq k} \frac{X_i}{\mathcal{D}_{k,i}} + \frac{X_k}{1 - Y_k} \sum_{i \neq k} \frac{Y_i}{\mathcal{D}_{k,i}} \right)^{-1} \quad (3.36)$$

In summary, the following molecular data have to be provided for each species k :

- Lennard-Jones well-depth as $\frac{\epsilon_k}{k_B}$

- Lennard-Jones collision diameter as $10^{10}\sigma_k$
- polarizability as $10^{30}\alpha_k$
- dipole moment as $\frac{10^{25}\bar{\mu}_k}{\sqrt{10}}$
- reference rotational relaxation collision number at $T = 298\text{ K}$ $Z_{rot,k}$
- molecule geometry (mono-atomic, linear, non-linear)

3.3.4 Chemical Source Terms

The forward molar reaction rate \dot{r}'_r of reaction r and reverse reaction rate \dot{r}''_r are computed by [46]

$$\dot{r}'_r = k'_r \prod_k C_k^{e'_{k,r}}, \quad \dot{r}''_r = k''_r \prod_k C_k^{\nu''_{k,r}} \quad (3.37)$$

where k'_r (k''_r) is the forward (reverse) rate constant of reaction r , $C_k = \frac{Y_k}{M_k}\rho$ is the molar concentration of species k and $e'_{k,r}$ the species reaction order, which for elementary reactions is the same as the stoichiometric coefficient $\nu'_{k,r}$ ($\nu''_{k,r}$) of the reactant (product) species k and reaction r . For three-body reactions, this is extended with an effective mixture concentration C_m :

$$\dot{r}'_r = k'_r C_m \prod_k C_k^{e'_{k,r}}, \quad \dot{r}''_r = k''_r C_m \prod_k C_k^{\nu''_{k,r}}, \quad C_m = \sum_k \varepsilon_k C_k \quad (3.38)$$

where the efficiencies ε_k are set to unity by default if no value is specified. The rate constants k_r for either the forward or reverse reaction can be computed as standard three-parameter Arrhenius reactions

$$k_r = A_r T^{\beta_r} \exp\left(-\frac{E_{a,r}}{\mathcal{R}T}\right) \quad (3.39)$$

or pressure dependent Lindemann falloff reactions

$$k_r = k_{r,\infty} \frac{p_r}{1 + p_r} F_r, \quad p_r = \frac{k_{r,0} C_m}{k_{r,\infty}}, \quad F_r = 1 \quad (3.40)$$

$$k_{r,0} = A_{r,0} T^{\beta_{r,0}} \exp\left(-\frac{E_{a,r,0}}{\mathcal{R}T}\right), \quad k_{r,\infty} = A_{r,\infty} T^{\beta_{r,\infty}} \exp\left(-\frac{E_{a,r,\infty}}{\mathcal{R}T}\right) \quad (3.41)$$

or Troe falloff reactions, which are the same as Lindemann reactions except that the blending function F_r is not unity and instead calculated with

$$\lg F_r = \left(1 + \left(\frac{\lg p_r + c}{n - d(\lg p_r + c)} \right)^2 \right)^{-1} \lg F_{r,cent} \quad (3.42)$$

$$c = -0.4 - 0.67 \lg F_{r,cent}, \quad n = 0.75 - 1.27 \lg F_{r,cent}, \quad d = 0.14 \quad (3.43)$$

$$F_{r,cent} = (1 - \alpha_r) \exp\left(-\frac{T}{T_r^{***}}\right) + \alpha_r \exp\left(-\frac{T}{T_r^*}\right) + \exp\left(-\frac{T_r^{**}}{T}\right) \quad (3.44)$$

where the last term including T_r^{**} is optional. A similar reaction type is SRI, which is computed like the Troe reactions, except that the blending function F_r is defined as by the following expression:

$$F_r = \left(a_r \exp\left(-\frac{b_r}{T}\right) + \exp\left(-\frac{T}{c_r}\right) \right)^{1/(1+\lg^2 p_r)} d_r T^{e_r} \quad (3.45)$$

Another supported reaction type are **plg** reactions, where the rate constants are interpolated logarithmically from pressure. The parameters A_r , β_r , $E_{a,r}$ for the rate constant expression k_r from Eq. (3.39) are specified at different pressure levels p_n , where P is the number of pressure levels. There may also be more than one set of parameters for the three parameter Arrhenius expression per pressure level, leading to the summation in Section 3.3.4 over all K rate constants at that pressure level. Given the current pressure p , the pressure p_n is looked up from all P pressure levels which is closest to p and $p_n \leq p$. This pressure will be denoted as p_{low} . The pressure $p_{n+1} > p$ is denoted as p_{high} . The rate constants at the two pressure levels p_{low} and p_{high} are computed from:

$$k_{r,low} = \sum_i^K k_{r,i}(p_{low}) \quad (3.46)$$

$$k_{r,high} = \sum_i^K k_{r,i}(p_{high}) \quad (3.47)$$

with the rate constants at the specific pressure levels $k_{r,i}(p_{low})$ and $k_{r,i}(p_{high})$ computed from Eq. (3.39). The final rate constant is then logarithmically interpolated from the pressure:

$$k_r = \exp\left(\log(k_{r,low}) + \left(\log(k_{r,high}) - \log(k_{r,low}) \right) \frac{\log(p) - \log(p_{low})}{\log(p_{high}) - \log(p_{low})} \right) \quad (3.48)$$

The parameters A_r , $A_r(p_n)$, $\beta_r, \beta_r(p_n)$, $E_{a,r}$, $E_{a,r}(p_n)$, $A_{r,0}$, $A_{r,\infty}$, $\beta_{r,0}$, $\beta_{r,\infty}$, $E_{a,r,0}$, $E_{a,r,\infty}$, α_r , T_r^* , T_r^{**} , T_r^{***} , a_r , b_r , c_r , d_r and e_r are read from the reaction mechanism file.

If the parameters for the reverse rate constant are not explicitly included in the reaction mechanism file, it is computed via the equilibrium constant K_r assuming ideal gases and perfect mixtures:

$$k_r'' = \frac{k_r'}{K_r}, \quad K_r = \exp\left(-\frac{\Delta G_r^\circ}{\mathcal{R}T}\right) \left(\frac{p^\circ}{\mathcal{R}T}\right)^{\Delta\nu_r} \quad (3.49)$$

p° is a reference pressure (usually 1 atm) and $\Delta\nu_r = \sum_k (\nu_{k,r}'' - \nu_{k,r}')$. The standard Gibbs free energy of formation ΔG_r° is

$$\Delta G_r^\circ = \sum_k (\nu_{k,r}'' - \nu_{k,r}') G_k^\circ, \quad G_k^\circ = \tilde{h}_k - T\tilde{s}_k \quad (3.50)$$

Additionally, reactions can be marked as `duplicate` to allow rate constants of the form $k_r = \sum_i k_{r,i}$. Finally, the reaction rate of species k is obtained with:

$$\dot{\omega}_k = \dot{r}_k M_k = M_k \sum_r (\nu_{k,r}'' - \nu_{k,r}') (\dot{r}_r' - \dot{r}_r'') \quad (3.51)$$

3.3.4.1 Operator Splitting

The time steps needed to integrate the system of chemical source terms are usually much smaller than the time steps required to solve the governing equations for non-reactive flows. Therefore, in order to integrate the governing equations for a reactive flow, the time step used by OpenFOAM Δt_{OF} has to be chosen small enough to resolve the chemical source terms adequately. This is very computationally expensive. To avoid this, an operator splitting technique is used: each finite volume (or cell) in the computational domain is considered to be an isochoric closed zero-dimensional batch reactor. At the beginning of each time step, the highly optimized library Sundials CVODE [83] is used to integrate the state of the batch reactor over the CFD time step Δt_{OF} for each cell and uses methods designed for stiff systems of differential equations. Thereby, much smaller time steps $\Delta t_{\text{Sundials}}$, that are adaptively chosen by Sundials, can be used to integrate the system of chemical reactions within Δt_{OF} . The system of $N + 1$ ordinary differential equations (ODE) integrated by Sundials is:

$$\int_{T(t_0)}^{T(t_0+\Delta t_{\text{OF}})} dT = \int_{t_0}^{t_0+\Delta t_{\text{OF}}} -\frac{\sum_k \dot{\omega}_k e_k}{\rho c_v} dt \quad (3.52)$$

$$\int_{Y_k(t_0)}^{Y_k(t_0+\Delta t_{\text{OF}})} dY_k = \int_{t_0}^{t_0+\Delta t_{\text{OF}}} \frac{\dot{\omega}_k}{\rho} dt, \quad k = 1 \dots N \quad (3.53)$$

with $c_v = c_p - \mathcal{R}/\bar{M}$. The partial specific internal energy e_k is computed from the fundamental equation for ideal gases as the specific internal energy of the pure species:

$$e_k = \frac{\tilde{e}_k}{M_k} = \frac{1}{M_k} (\tilde{h}_k - \mathcal{R}T) \quad (3.54)$$

The equation of state for ideal gases is used to compute the pressure. With this approach, the chemical source terms are computed decoupled from the governing equations. With the mass fractions $Y_k(t_0)$ and $Y_k(t_0 + \Delta t_{OF})$, a time step averaged reaction rate is obtained, which is used in the governing equations:

$$\dot{\omega}_k = M_k \frac{\partial C_k}{\partial t} \approx M_k \frac{C_k(t_0 + \Delta t_{OF}) - C_k(t_0)}{\Delta t_{OF}} \quad (3.55)$$

where $C_k(t_0 + \Delta t_{OF}) = \frac{Y_k(t_0 + \Delta t_{OF})\rho}{M_k}$ is the value obtained from the integration performed by Sundials.

Steady-State Flames

Two dimensional planar jet-flames have been simulated using DNS. This chapter describes the numerical setup and explains why this particular flame type was chosen. Markstein numbers are computed and the effect of total stretch \mathbb{K} , aerodynamic strain \mathbb{K}_s and stretch due to the propagation of a curved flame \mathbb{K}_c on local flame speeds is highlighted.

4.1 Numerical Setup

The DNS solver utilizes the open-source library OpenFOAM to solve the transport equations and the open-source code Cantera [36] to compute thermo-physical and transport properties as well as chemical reaction rates (see section 3.3). The Finite Volume Method is used to solve the fully compressible Navier-Stokes equations. Convective terms are discretized by a fourth order interpolation scheme and diffusive terms are discretized using fourth order unbounded schemes. The time discretization is fully implicit with a second order scheme. The system of linearized equations is solved iteratively using (bi-)conjugate gradient methods. Diagonal incomplete-Cholesky and Lower-Upper decompositions are used as preconditioners. The PIMPLE algorithm, which combines the SIMPLE (semi-implicit method for pressure-linked equations) and PISO (pressure implicit with splitting the operators) algorithms, is used for pressure correction. Gravitation is neglected. Hydrogen flames are simulated using the reaction mechanism by Li et al. [55] (see Appendix B.1), containing 9 species and 38 elementary reactions. For methane flames, the reaction mechanism by Kee et al. [47] (see Appendix B.2) including 17 species and 58 elementary reactions, is used.

4.1.1 Computational Domain and Boundary Conditions

In Figure 4.1 the computational domain is depicted. It is two-dimensional and has a rectangular shape with 2 cm in the stream-wise (y) direction and 1 cm in the span-wise (x) direction. It is equidistantly discretized with 20 μm (500,000 cells in total) so that the flame fronts are resolved by 17 to 60 cells based on the thermal thickness δ_{th}^0 (see Eq. (2.2))

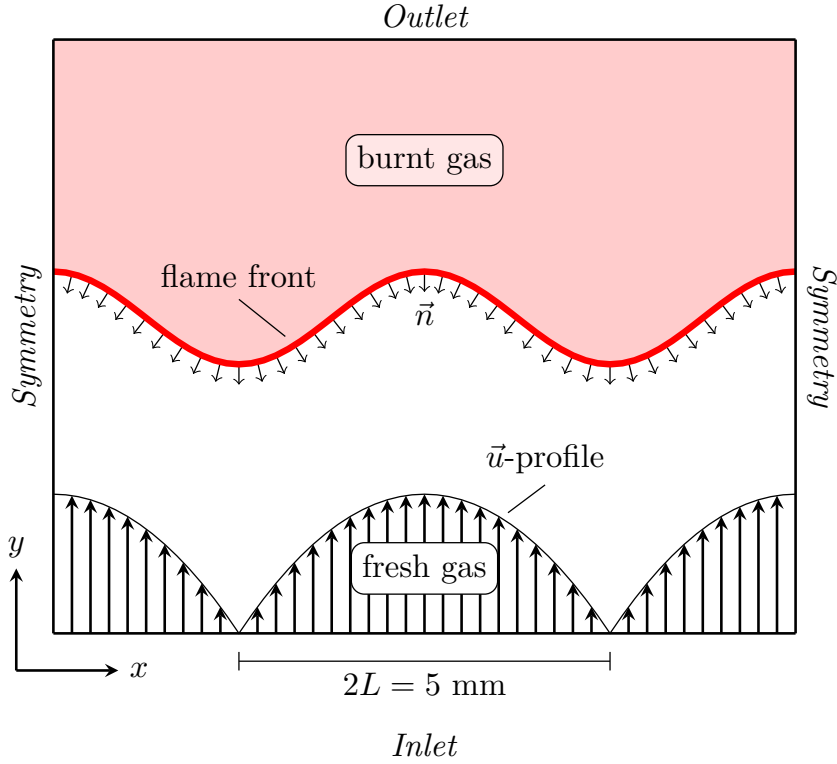


Figure 4.1: Computational domain, boundary conditions and inlet velocity profile.

and Table 4.2). The time step is set to $0.25 \mu\text{s}$.

As illustrated in Figure 4.1, the fresh gas enters the inlet with $T = 300 \text{ K}$ and $p = 1 \text{ bar}$ in the positive y -direction and the burnt gases leave the domain at the outlet. The setup corresponds to an array of slot burners with infinitely thin walls, where the velocity profile at the inlet of each slot burner is set to be the parabolic velocity profile given by the Poiseuille solution:

$$u_y(x) = u_{y,\max} \left(1 - \left(\frac{(x+L) \bmod (2L)}{L} - 1 \right)^2 \right) \quad (4.1)$$

with $L = 2.5 \text{ mm}$. The velocity is zero in-between the slot burners and has its maximum $u_{y,\max}$ at the center. Using this setup, a plane-jet flame in the middle and two half plane-jet flames at the sides are created, leading to a continuous corrugated flame.

The boundary conditions are summarized in Table 4.1: the velocity profile \vec{u} from Eq. (4.1) is prescribed at the inlet and zero gradient at the outlet. Temperature T and the mass fractions Y of fuel, nitrogen and air are fixed at the inlet and have a zero gradient at the outlet too. The lateral sides are set as symmetry planes to avoid a loss of mass and to ensure perfect symmetry inside the domain. At the inlet and outlet, a partially non-reflecting boundary condition (PNRBC) for the pressure p is used [74] to bypass pressure waves.

Table 4.1: *Boundary conditions used in the simulation.*

	\vec{u}	T	$Y_{\text{fuel}}, Y_{\text{O}_2}, Y_{\text{N}_2}$	p
Inlet	profile from Eq. (4.1)	fixed	fixed	PNRBC
Outlet	zero gradient	zero gradient	zero gradient	PNRBC
Sides	symmetry	symmetry	symmetry	symmetry

The domain is initialized with a planar flame obtained from one-dimensional computations. Reynolds numbers for the different cases are summarized in Table 4.2.

$$Re = u_{\text{bulk}} \frac{2L}{\nu} = \frac{4}{3} u_{y,\text{max}} \frac{L}{\nu} \quad (4.2)$$

based on the bulk inlet velocity u_{bulk} :

$$u_{\text{bulk}} = \frac{1}{L} \int_0^L u_{y,\text{max}} \left(1 - \frac{x^2}{L^2}\right)^2 dx \frac{2L}{\nu} = \frac{2}{3} u_{y,\text{max}} \quad (4.3)$$

ν is the kinematic viscosity of the unburnt mixture. Laminar unstretched flame speed s_L^0 , the thermal thickness δ_{th}^0 from Eq. (2.2), the chemical time scale from Eq. (2.3) and the

Table 4.2: *Parameters for the methane and hydrogen flames at atmospheric conditions.*

	H ₂ /air						
ϕ	0.4	0.5	0.8	1.0	2.5	4.0	6.5
$u_{y,\text{max}}$ in m s ⁻¹	3.0	6.0	10.2	13.8	13.5	5.1	0.9
Re	540	1050	1640	2100	1540	481	70
s_L^0 in m s ⁻¹	0.23	0.55	1.69	2.29	2.69	1.69	0.63
δ_{th}^0 in mm	0.61	0.42	0.35	0.36	0.35	0.44	0.8
τ_c^0 in ms	2.6	0.75	0.21	0.16	0.13	0.26	1.3
Le	0.43	0.46	0.54	0.59	1.95	1.98	1.97
$Y_{\text{H}_2,q_{\text{max}}}^0$	0.0014	0.0032	0.0129	0.0194	0.0582	0.0918	0.1406
	CH ₄ /air						
ϕ	0.6	0.7	0.9	1.0	1.2	1.3	
$u_{y,\text{max}}$ in m s ⁻¹	0.15	0.45	0.98	1.04	0.80	0.45	
Re	31	93	201	213	134	92	
s_L^0 in m s ⁻¹	0.12	0.19	0.33	0.37	0.35	0.26	
δ_{th}^0 in mm	0.93	0.66	0.49	0.46	0.46	0.58	
τ_c^0 in ms	8.0	3.4	1.5	1.3	1.3	2.2	
Le	1.004	1.005	1.006	1.007	1.074	1.074	
$Y_{\text{CH}_4,q_{\text{max}}}^0$	0.0018	0.0024	0.0031	0.0033	0.0040	0.0047	

Lewis number Le from Eq. (2.37) are summarized in Table 4.2 for the different equivalence ratios ϕ too. The flame is assumed to be represented by the iso-surface of the fuel mass fraction corresponding to the maximum heat release in an unstretched one-dimensional flame $Y_{F,q_{\max}}^0$.

Different equivalence ratios of methane and hydrogen are investigated. Additionally, for each steady-state simulation transient simulations of oscillating flames with different frequencies were conducted (see chapter 5). Due to the high computational costs of DNS, all simulations for this work have been performed on high performance clusters including the CRAY XC40 HAZEL-HEN cluster [39] (180,000 physical CPU cores with 7.4 PFlops) at the High Performance Computing Center in Stuttgart and the ForHLR 2 Cluster [82] (23,000 physical CPU cores with 0.8 TFlops) at the Karlsruhe Institute of Technology.

4.2 Choice of Setup

This setup of plane-jet flames forming a corrugated flame front was chosen for several reasons: On one hand, the flame is embedded into a laminar flow. In contrast to turbulent flows, stretching can be investigated without turbulent fluctuations. In the case of the oscillating flames in chapter 5, isolated fluctuation frequencies can be investigated without the broad-band frequency spectrum of turbulent flows.

On the other hand, the two-dimensional corrugated flame front experiences flame stretch through curvature \mathbb{K}_c , aerodynamic straining \mathbb{K}_s and tangential velocity gradients \mathbb{K}_t (see Eq. (2.33) and Eq. (2.35)). Like realistic turbulent flames, it experiences negative stretch (at the tip) and positive stretch (at the base) [80]. Additionally, spatial stretch gradients can be varied by increasing the mass flow rate at the inlet. Most of the simulations [5, 9, 28, 31, 32, 40, 42, 51, 53, 57, 58, 75, 84, 85, 86, 93, 100] done to study the effect of flame stretch on laminar steady as well as oscillating flames used simplified chemistry and combustion modeling or used setups where the flame is not subjected to all stretch contributions: spherical expanding flames are only positively curved and stretched and there are no tangential velocity gradients \mathbb{K}_t and no spatial stretch gradients along the flame surface. Stagnation-point flames like counter-flow flames have no curvature, are only positively stretched and experience stretch only through tangential straining \mathbb{K}_t .

4.3 Results

In Figure 4.2 on the left, the shape of the middle plane-jet flame is depicted for five different equivalence ratios of the hydrogen flames. The lines shown are the iso-surface of $Y_{F,q_{\max}}^0$ representing the flame front (see Table 4.2). They are slightly lifted from the inlet at $y = 0$ mm because of heat losses to the inlet. On the right of Figure 4.2, the normalized

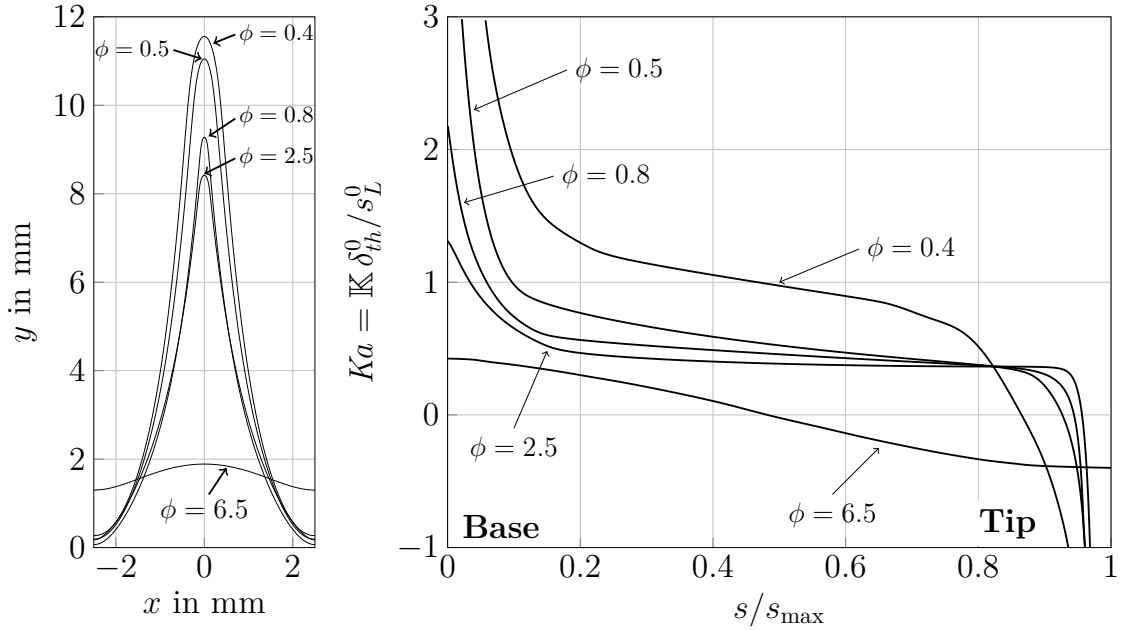


Figure 4.2: Shape of the hydrogen flames (left) and profile of normalized flame stretch along the flame coordinate s (right).

stretch or Karlovitz number Ka is plotted over the flame tangential coordinate s along the flame front, where $s = 0$ at the base of the flame and $s = s_{max}$ at the tip. The highest positive stretch rates are at the base caused by the high positive curvature. Similarly, the highest negative stretch rate is at the negatively curved tip. In Figure 4.3 the shapes of a subset of the methane flames are depicted. Similar results are found for the other equivalence ratios. The distribution of flame stretch over flame coordinate is qualitatively similar to the hydrogen flames in Figure 4.2 and can be seen in Figure 4.4 for methane

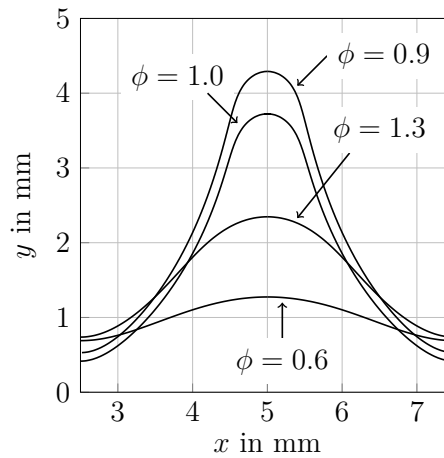


Figure 4.3: Shapes of the steady-state methane flames.

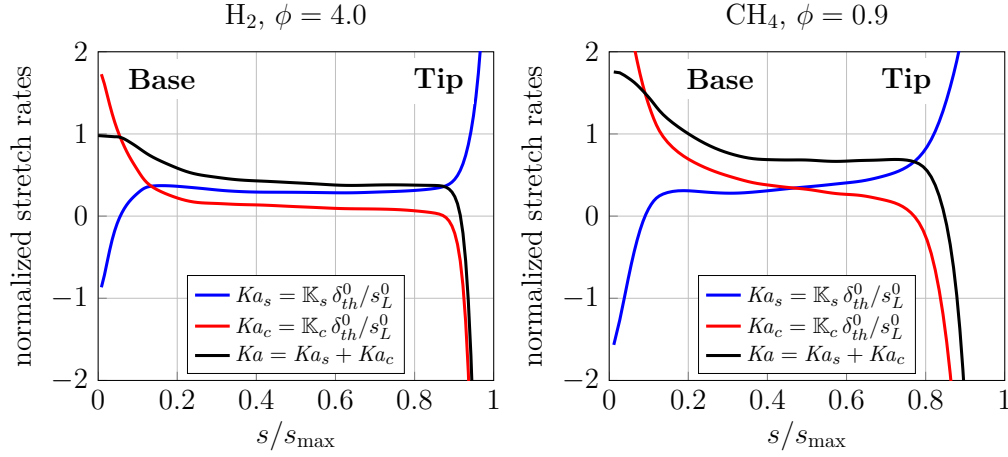


Figure 4.4: Normalized flame stretch Ka (—), aerodynamic strain Ka_s (—) and stretch due to flame propagation and curvature Ka_c (—) along the flame front for a hydrogen and a methane flame.

with $\phi = 0.9$.

As explained in Eq. (2.35), flame stretch \mathbb{K} can be divided into aerodynamic strain \mathbb{K}_s and a curvature term \mathbb{K}_c . These are plotted against the normalized flame coordinate in Figure 4.4 as an example for a rich hydrogen flame with $\phi = 4$ (left) and a lean methane flame with $\phi = 0.9$ (right). Because \mathbb{K}_c is proportional to the curvature, its highest value is at the positively curved base at $s = 0$ and is lowest at the negatively curved tip at $s = s_{\max}$. The aerodynamic strain \mathbb{K}_s is negative at the base and positive at the tip, counteracting the effect of the curvature term. At $Ka = 0$ the normalized flame speed s_c/s_L^0 is not exactly unity because on one hand the computed flame stretch depends on the choice of iso-surface. On the other hand, flame stretch of zero is not a result of strain \mathbb{K}_s and curvature K_c being zero. Instead, strain and curvature have the same magnitude but opposite sign as shown in Figure 4.4. Therefore, flames with $Ka = 0$ are still curved and strained.

The effect of the Lewis number described in subsection 2.4.1 is shown in Figure 4.5 for the hydrogen flames: Rich hydrogen flames ($\phi > 1$) have a Lewis number greater than unity (see Table 4.2) so that flame speeds at the tip are higher than at the base due to focused diffusion. This can be seen from the reaction rates of hydrogen in Figure 4.5. The highest reaction rates appear at the tip. Lean hydrogen flames have Lewis number below unity. Because the diffusion coefficient of hydrogen is two to four times larger than the diffusion coefficient of oxygen (depending on the equivalence ratio), lean hydrogen flames are unstable. Therefore, the flame speed is higher at the positively curved and stretched base of the flame than at the tip of the flame. They even extinguish at the tip due to the high negative stretching. At $\phi = 0.8$ and $\phi = 1.0$ the behavior transitions from unstable to stable so that these flames are not sensitive to stretch and curvature and the reaction rates

do not vary considerably along the flame front.

Both lean and rich methane flames have Lewis numbers greater than unity and are thermo-diffusively stable. Figure 4.6 shows that the highest reaction rates occur at the tip as explained in subsection 2.4.1. Very lean methane flames ($\phi = 0.6$ and $\phi = 0.7$) have a Lewis number close to unity. They are also insensitive to stretch and curvature, as demonstrated by the constant reaction rate profile along the flame front.

The correlation of the consumption speed s_c with flame stretch is depicted for hydrogen flames in Figure 4.7 on the top left. As indicated by the reaction rates in Figure 4.5, consumption speeds increase with stretch for lean hydrogen flames, leading to negative Markstein numbers. For rich hydrogen flames consumption speeds decrease with stretch, yielding positive Markstein numbers. For the flames with $\phi = 0.8$ (●) and $\phi = 1$ (○), consumption speeds are only weakly affected by stretch, leading to Markstein numbers close to zero. The hook shaped distribution at positive stretch values observable for $\phi = 2.5$ (○) and $\phi = 4$ (●) is caused by heat losses from the base of the flame to the inlet flow [75]. The depicted range of $-1 < Ka < 3$ also shows, that the assumption of a linear correlation of flame speed with flame stretch is only valid for small stretching rates around zero. The flames with $\phi = 2.5$ (○) and $\phi = 6.5$ (○) cover a lower range of Karlovitz numbers than the other flames because their respective flame speeds are lower so that the inlet velocity is set lower, leading to a shorter and less curved flame.

In Figure 4.7 on the top right normalized consumption speeds are plotted against the stretching due to flame propagation and curvature Ka_c from Eq. (2.35). The behavior of consumption speed depending on Ka_c is qualitatively similar to the total stretch Ka , that is consumption speeds increase with Ka_c for lean hydrogen flames and decrease for rich hydrogen flames. The steeper rise of s_c with Ka_c suggests that curvature influences local flame speeds more strongly than aerodynamic straining (see also Figure 4.10). The correlation of consumption speed and aerodynamic straining is shown on the bottom left. On the bottom right, consumption speeds are plotted against the local equivalence ratio ϕ_{local} at the iso-surface of $Y_{F,q_{\text{max}}}^0$ divided by equivalence ratio of the unburnt mixture ϕ . The local equivalence ratio changes along the flame front due to preferential diffusion. It is computed from the ratio of the present molar fraction of oxygen atoms to the mole fraction of oxygen atoms required for stoichiometric combustion:

$$\phi_{\text{local}} = \frac{X_{\text{O,present}}}{X_{\text{O,required}}} \quad (4.4)$$

For the lean flames, consumption speeds increase as the local equivalence ratio is shifted toward stoichiometric conditions. For rich hydrogen flames, consumption speeds decrease with increasing local equivalence ratios. For the flame with $\phi = 1$, a maximum of consumption speed is found at $\phi_{\text{local}} \approx 0.9$. Note, that the absolute value of local

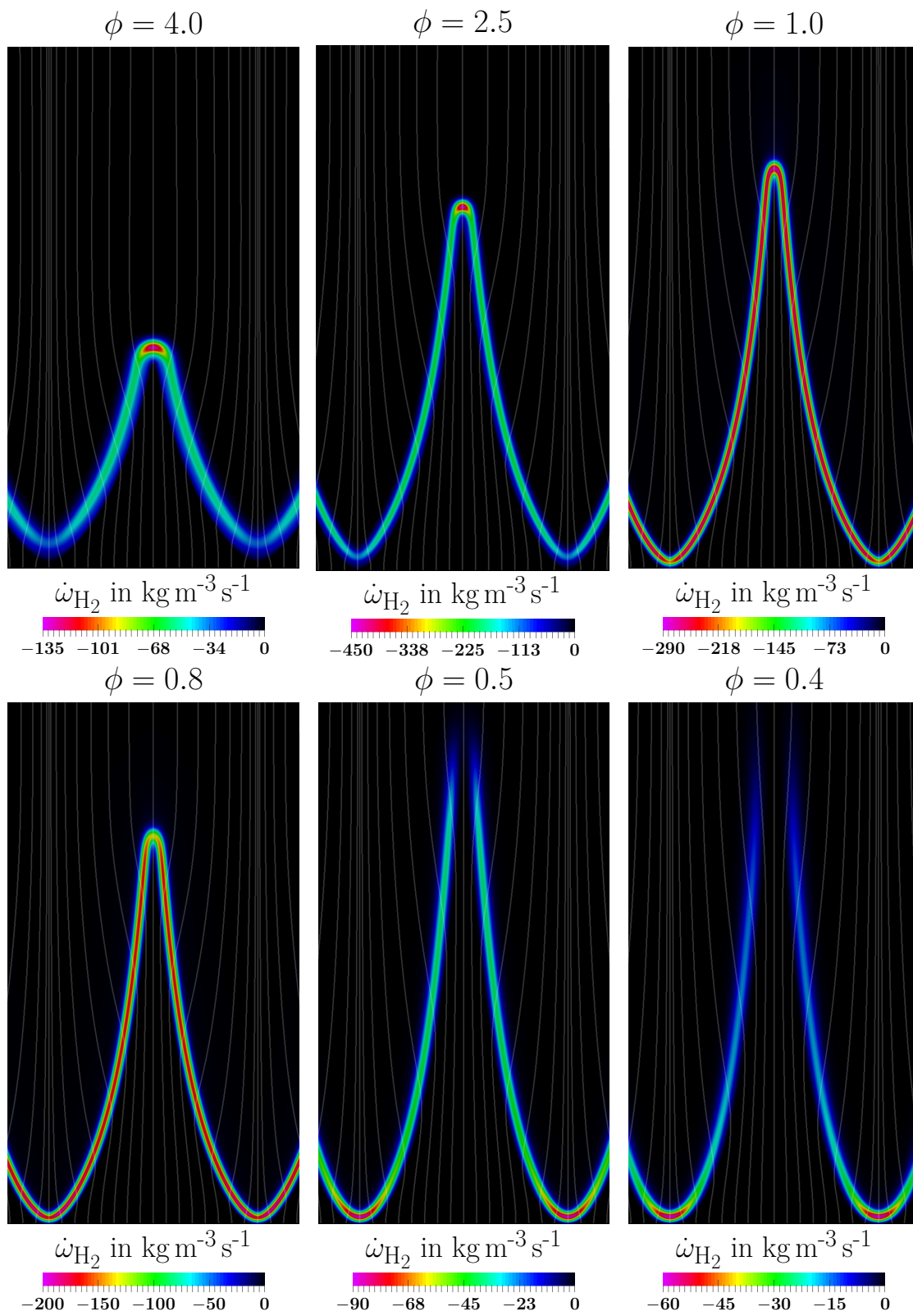


Figure 4.5: Hydrogen reaction rates for different equivalence ratios. Gray lines show the fluid velocity streamlines. Dimensions are $1.25 \text{ mm} < x < 8.75 \text{ mm}$ and $0 \text{ mm} < y < 12 \text{ mm}$.

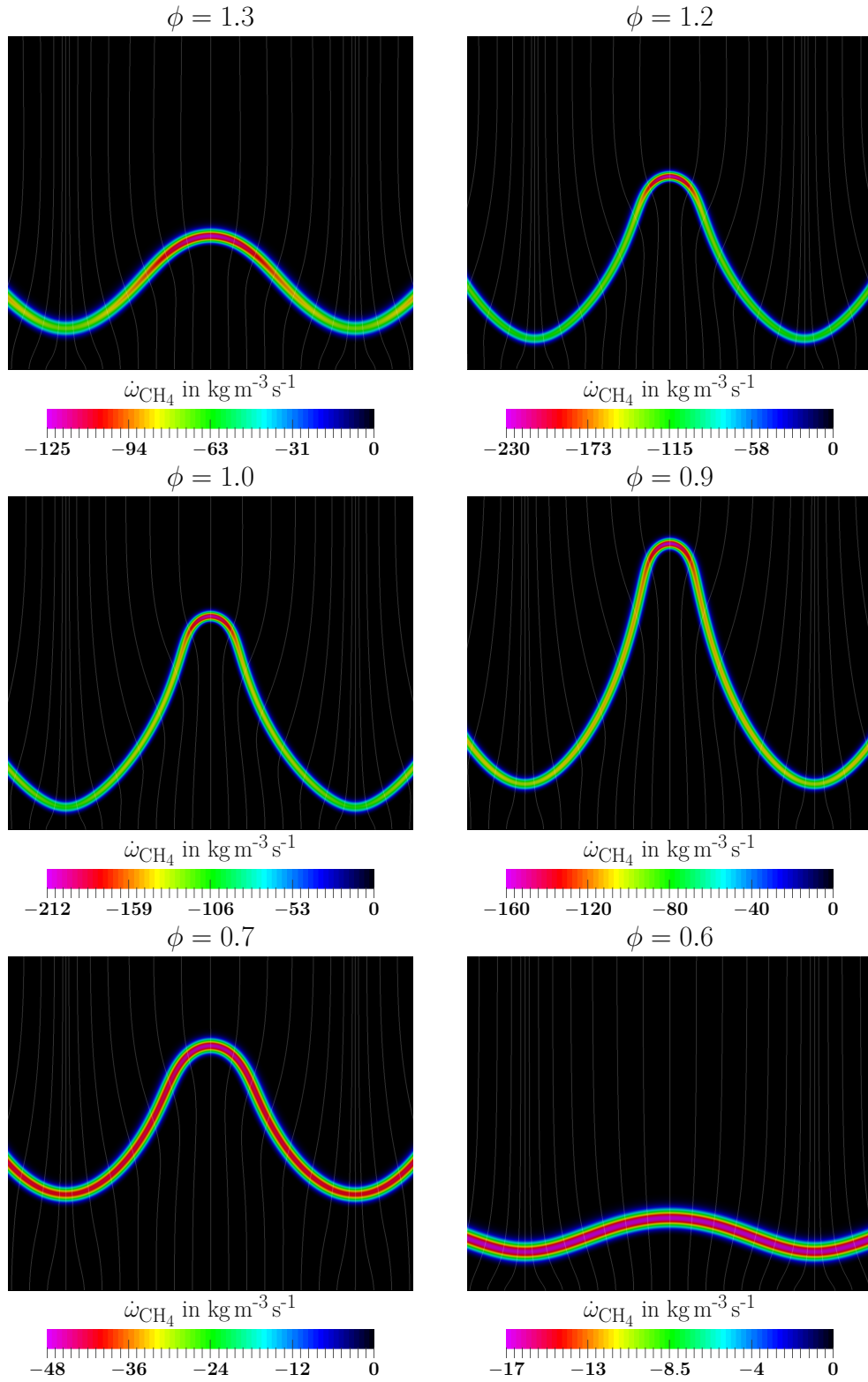


Figure 4.6: Methane reaction rates for different equivalence ratios. Gray lines show the fluid velocity streamlines. Dimensions are $1.25 \text{ mm} < x < 8.75 \text{ mm}$ and $0 \text{ mm} < y < 4.5 \text{ mm}$

equivalence ratio can change within the flame front. The depicted trends however have been found to not be affected qualitatively by choosing different iso-surfaces.

Figure 4.8 shows the correlations of consumption speed for the methane flames. On the top left, normalized consumption speeds are plotted against the Karlovitz number. Because all methane flames have Lewis number of $Le \geq 1$, consumption speeds for both lean and rich methane flames decrease with flame stretch. For $\phi = 0.6$ (●) the Lewis number is approximately unity so that the consumption speeds are insensitive to stretch, resulting in a Markstein number of about zero. The sensitivity to stretch shown by the slope of s_c over stretch and therewith Markstein number rises with increasing equivalence ratio or Lewis number, respectively. In Figure 4.8 on the top right consumption speeds are plotted against Ka_c , yielding similar trends as the total stretch Ka .

Plotting consumption speeds over local equivalence ratios on the bottom right shows

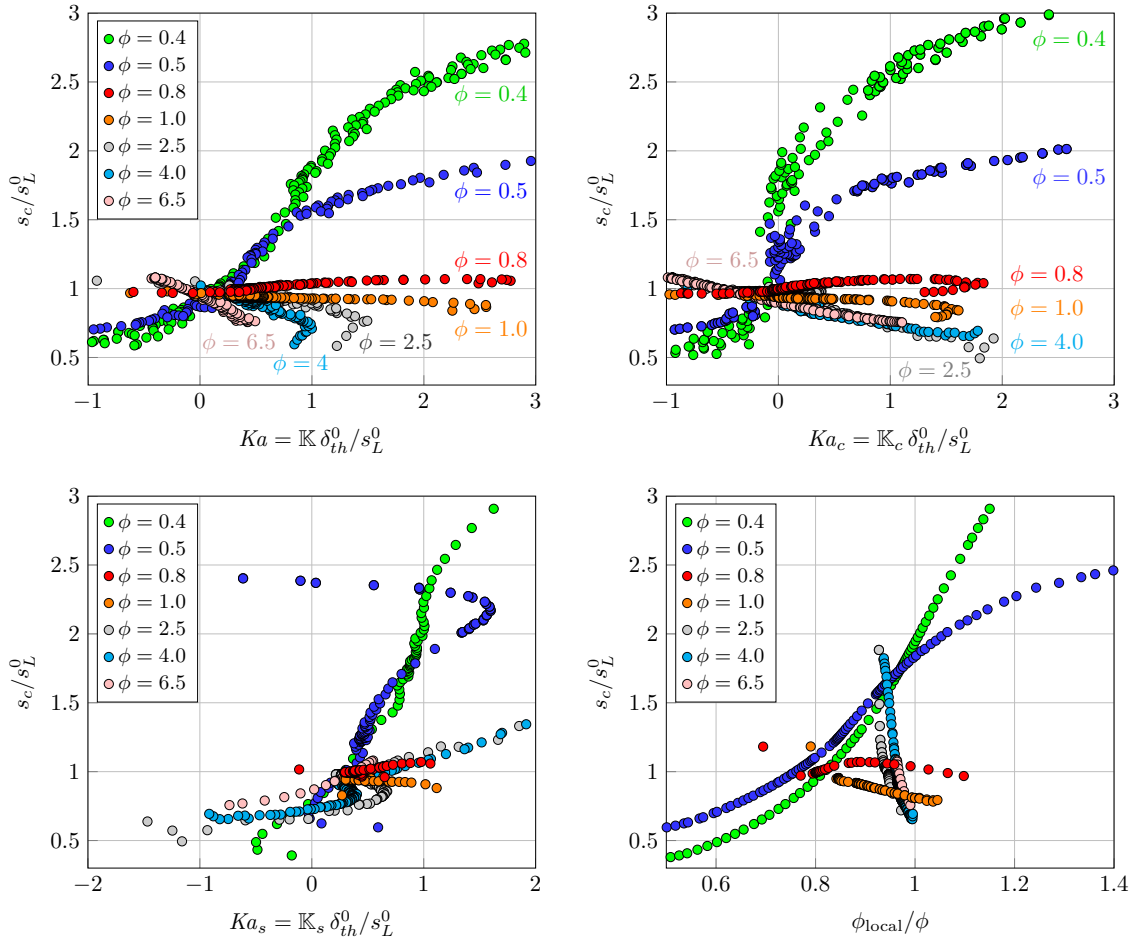


Figure 4.7: Normalized consumption speed of the hydrogen flames over normalized flame stretch Ka (top left), over normalized curvature Ka_c (top right), over normalized aerodynamic strain Ka_s (bottom left) and over local equivalence ratio ϕ_{local} (bottom right).

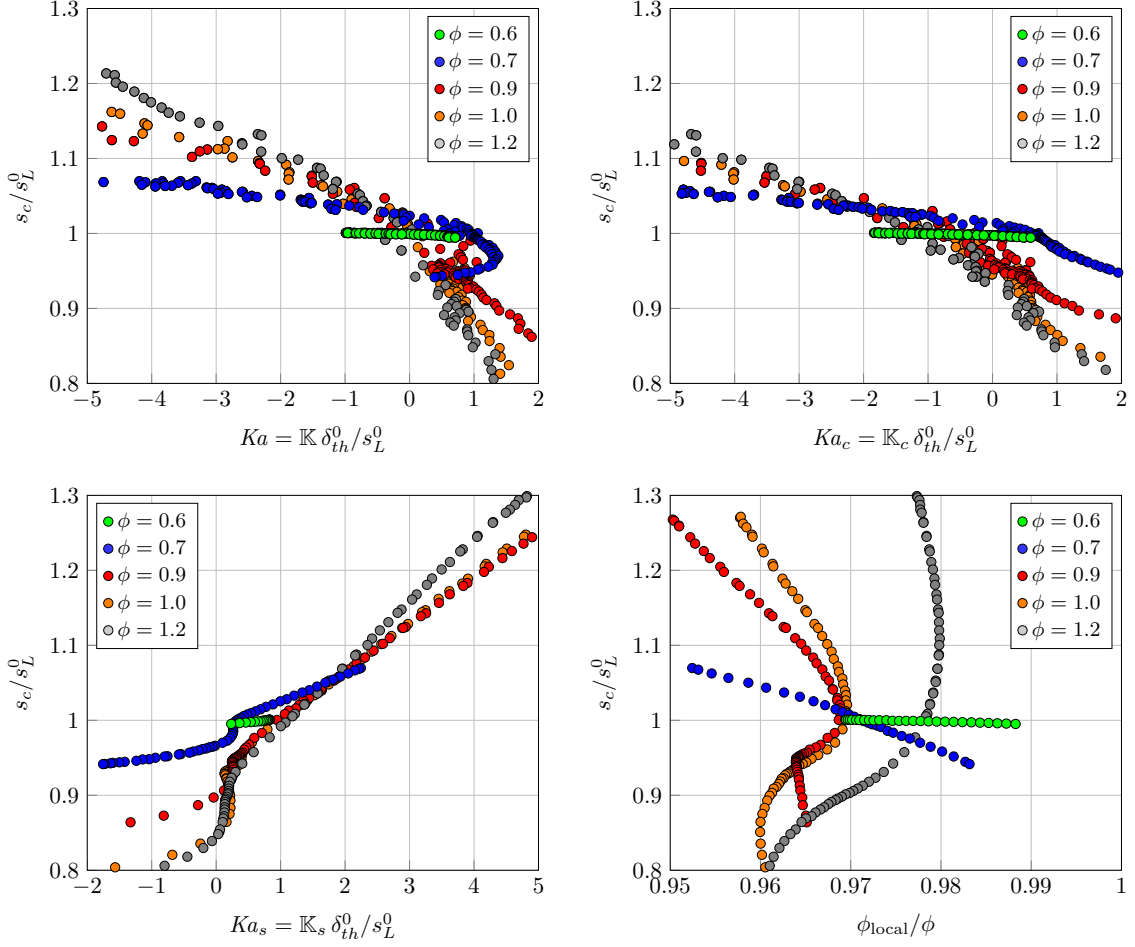


Figure 4.8: Normalized consumption speed of methane flames over normalized flame stretch Ka (top left), over normalized curvature Ka_c (top right), over normalized aerodynamic strain Ka_s (bottom left) and over local equivalence ratio ϕ_{local} (bottom right).

that the range of local equivalence ratios is substantially smaller than in the hydrogen flames in Figure 4.7. The reason is that the diffusion coefficient of methane is only about 10 % higher than the diffusion coefficient of oxygen so that the effect of preferential diffusion is much smaller than in hydrogen flames. The methane flame with $\phi = 0.7$ (\bullet) decreases its consumption speed monotonically with local equivalence ratio, although the local equivalence ratio is shifted toward more stoichiometric conditions for this lean flame. In Figure 4.9 on the left, local equivalence ratio is plotted over the flame coordinate for $\phi = 0.7$. Because methane diffuses slightly faster than oxygen, local equivalence ratios are higher at the base where diffusive mass fluxes are focused. But because the flame is controlled by heat conduction because of $Le > 1$, the base loses more heat than the tip, lowering the consumption speeds at the base counteracting the effect of equivalence ratios shifting toward more stoichiometric conditions. For all hydrogen flames the same

monotonic increase of local equivalence ratio from the tip to the base is observed.

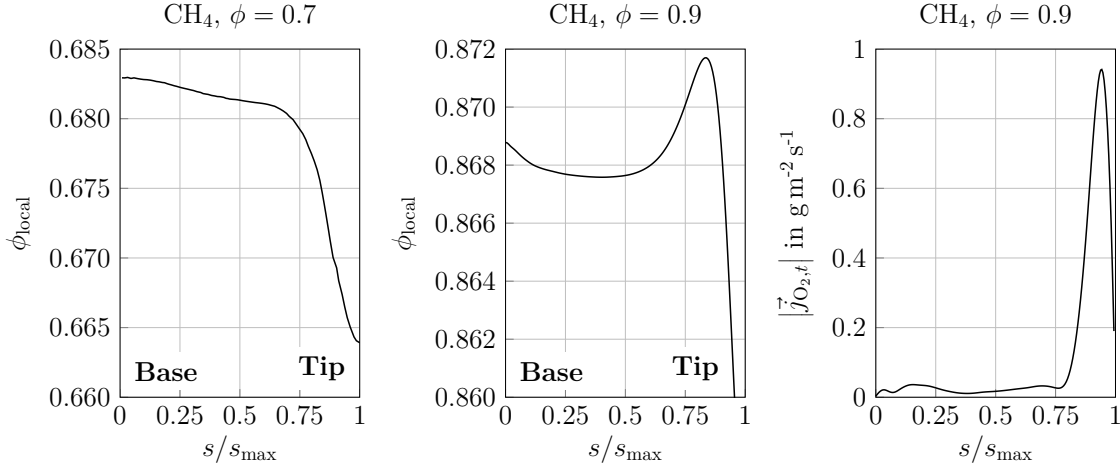


Figure 4.9: Local equivalence ratios ϕ_{local} along the flame front from base to tip for methane with $\phi = 0.7$ (left) and $\phi = 0.9$ (middle) and diffusive flux of oxygen parallel to the flame front (right).

Methane flames with $\phi > 0.7$ depend not uniquely on the local equivalence ratio. The reason for this is shown in Figure 4.9 in the middle for $\phi = 0.9$. Local equivalence ratios decrease from the base of the flame toward the tip as expected from $D_{\text{CH}_4} > D_{\text{O}_2}$. But at $\phi_{\text{local}} \approx 0.8$ there is a maximum of local equivalence ratio. This has been observed not only for iso-surfaces of methane but also oxygen, temperature and heat release rate as long as the iso-surface is located within the reaction zone. On the right, the magnitude of the diffusive flux of oxygen parallel to the flame surface $\vec{j}_{\text{O}_2,t}$ is shown for $\phi = 0.9$:

$$|\vec{j}_{\text{O}_2,t}| = \left| \vec{j}_{\text{O}_2} - (\vec{j}_{\text{O}_2} \cdot \vec{n}) \vec{n} \right| \quad (4.5)$$

Near the tip, oxygen diffuses faster due to the strong curvature. This might lead to an additional increase of the local oxygen concentration which is not compensated by the methane mass flux.

The Markstein numbers obtained from the correlation of normalized consumption speed with normalized flame stretch Ka in Figure 4.7 and Figure 4.8 is shown in Figure 4.10 for hydrogen (left) and methane (right). They are computed using the linear Markstein correlation from Eq. (2.44). The linear regression is performed over a range of $-0.5 < Ka < 1$ which covers most of the flame surface ($0.1 < s/s_{\text{max}} < 0.9$) and includes regions near the positively curved base and negatively curved tip while staying within the range of small stretch where the linear assumption is applicable. Figure 4.10 shows the Markstein numbers Ma (\bullet) based on total stretch Ka and Markstein numbers Ma_c (\circ) based on the curvature term Ka_c . Both Markstein numbers (Ma and Ma_c) have the same sign. However, Ma_c is greater in magnitude than Ma for lean hydrogen flames and similar to Ma for the

stable methane and rich hydrogen flames.

There is also an influence of the global stretch rate on the Markstein numbers. By increasing $u_{y,\max}$ and therewith the mass flow rate, the flames become longer but remain in steady state. This is shown in Figure 4.11 for a hydrogen flame with $\phi = 0.8$ with $u_{y,\max} = 8 \text{ m s}^{-1}$, 10 m s^{-1} and 15 m s^{-1} used in Eq. (4.1).

In Figure 4.12, the correlation of normalized consumption speed with the Karlovitz

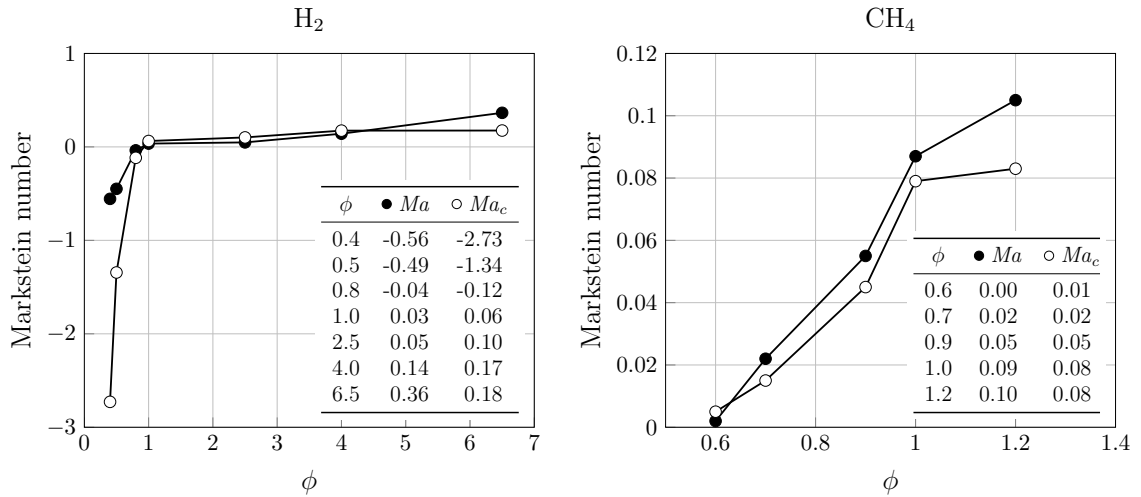


Figure 4.10: Markstein numbers Ma based on Ka (\bullet) and Markstein numbers Ma_c based on Ka_c (\circ) for hydrogen (left) and methane (right).

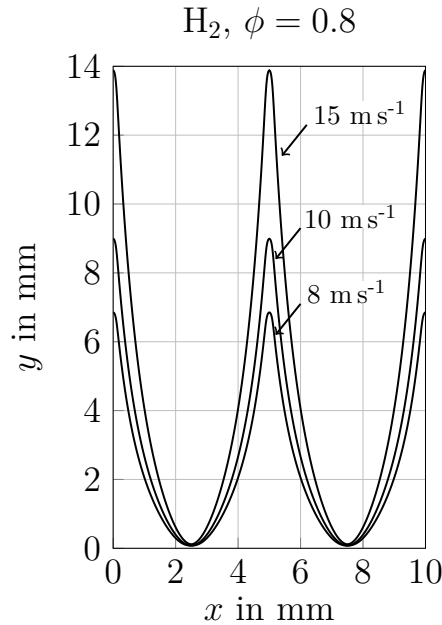


Figure 4.11: Shapes of the steady-state hydrogen flames with $\phi = 0.8$ for three different mass flow rates with $u_{y,\max} = 8 \text{ m s}^{-1}$, 10 m s^{-1} and 15 m s^{-1} . Lines are iso-surfaces of $Y_{F,qmax}^0$.

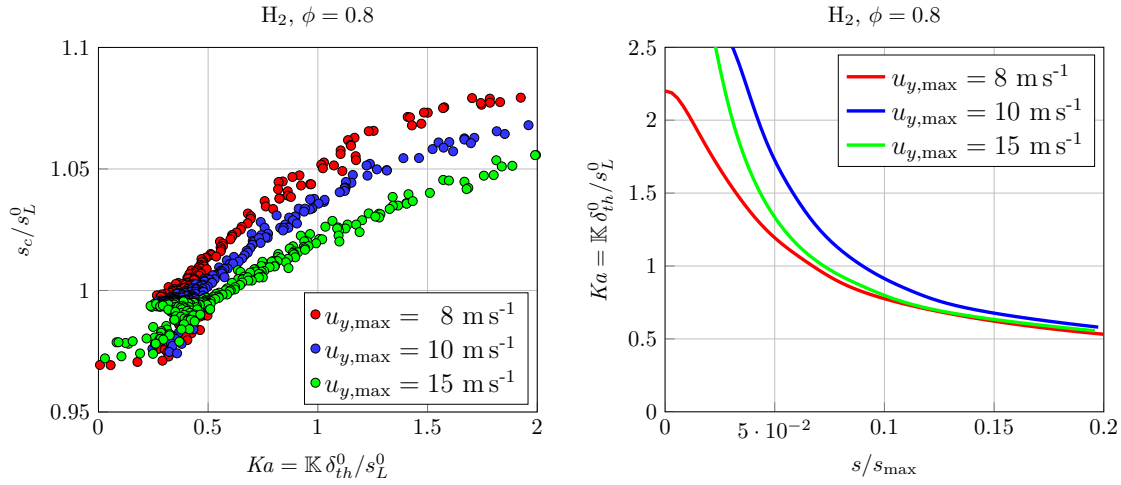


Figure 4.12: Effects of different mass flow rates on the correlation of consumption speeds and flame stretch (left) and flame stretch gradients along the flame front (right) for a hydrogen flame.

number is shown. The slope of consumption speed over stretch rate is different for each mass flow rate of Figure 4.12 so that slightly different Markstein numbers are obtained. On the right of Figure 4.12, stretch rates are plotted over the flame coordinate s . It can be seen that the Markstein numbers differ the most in regions where the gradient of flame stretch along the flame surface $\partial\mathbb{K}/\partial s$ is different between the setups. For $\phi = 0.8$ this is near the base between $0 < Ka < 2$. Similar results have been obtained for the oscillating flames in chapter 5 where the shape of the flames is affected by the unsteady movement of the flame front.

Oscillating Flames

To study the influence of unsteady stretching the previously computed steady-state flames are placed in an harmonically excited flow field. The response of the flame in terms of movement of the flame tip and relaxation time is evaluated. The correlation of flame speed and flame stretch at different phase angles within one oscillation period is investigated. Additionally, time averaged Markstein numbers for individual frequencies are calculated.

5.1 Numerical Setup

The numerical setup is the same as for the steady-state flames described in section 4.1. The only difference is that the inlet velocity in the stream-wise y -direction is forced to oscillate with:

$$\hat{u}_x(x, t) = u_y(x) (1 + a \sin(2\pi ft)) \quad (5.1)$$

where $u_y(x)$ is the steady-state velocity profile from Eq. (4.1). The transient flow is characterized by the amplitude a and the frequency f . The flow is still laminar.

5.2 Flame Relaxation Times

The flame relaxation times τ are computed from the phase shift of the movement of the flame front and the fluid velocity at the flame front. The movement of the flame is tracked in terms of the flame height h , which is the position of the flame tip y_{tip} . As an example, Figure 5.1 on the left shows this for the middle plane-jet flame of hydrogen with $\phi = 0.5$ which oscillates in a flow field excited by a frequency of $f = 100$ Hz and an amplitude of $a = 0.3$. On the right, the position of the flame tip h is recorded over time.

The movement of the flame tip is illustrated in Figure 5.2 for different methane and hydrogen flames and fixed amplitudes over two oscillation periods (time t normalized by frequency f). The dashed lines show the oscillation of the fluid velocity at the tip of the flame which is not the oscillation at the inlet. The oscillation at the inlet flow and at the flame differ due to compressibility effects when the disturbances are convected from

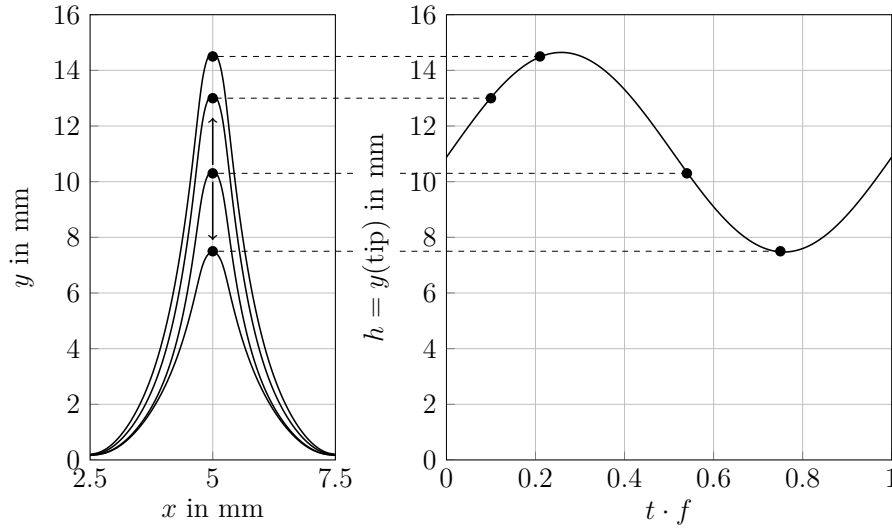


Figure 5.1: Shapes of the hydrogen flame with $\phi = 0.5$ in a periodically oscillating flow with $f = 100$ Hz and $a = 0.3$ (left) and position of the flame tip h over one oscillation period (right).

the inlet to the flame. The phase shift $\Delta\alpha$ between the flow field at the tip and the movement of the tip is demonstrated for hydrogen $\phi = 6.5$ with $f = 50$ Hz (top left) and methane $\phi = 0.6$ with $f = 20$ Hz (middle left). The following conclusions can be drawn from Figure 5.2:

- The flames oscillate with the same frequency as the flow.
- The movement of the flame front is attenuated with increasing frequency.
- The phase shift $\Delta\alpha$ increases with increasing frequency.
- The movement of flames with high chemical time scales τ_c^0 is attenuated more than the movement of flames with low chemical time scales. For example, the hydrogen flame with $\phi = 6.5$ at the top left barely moves at $f = 1000$ Hz. For the hydrogen flame with $\phi = 0.8$ the displacement of the flame tip is affected only marginally even at $f = 1000$ Hz. This corresponds to the time scales $\tau_c^0(\phi = 0.8) < \tau_c^0(\phi = 6.5)$ (see Table 4.2). For the methane flames, this effect can be seen for $\phi = 1$ and $\phi = 0.7$: at $f = 500$ Hz, the flame with $\phi = 0.7$ moves only very weakly while the stoichiometric flame has a visible displacement from its steady-state position because $\tau_c^0(\phi = 1) < \tau_c^0(\phi = 0.7)$ for the methane flames.

In Figure 5.3, the oscillation of the flames is shown for a fixed frequency of $f = 100$ Hz and a fixed amplitude of $a = 0.6$ for the hydrogen flames and $a = 0.5$ for the methane flames. The direct comparison of the flames shows the influence of the chemical time scale on the flame response. For hydrogen, $\tau_c^0(\phi = 0.8) < \tau_c^0(\phi = 4) < \tau_c^0(\phi = 6.5)$ and for methane, $\tau_c^0(\phi = 1) \approx \tau_c^0(\phi = 0.9) < \tau_c^0(\phi = 0.7) < \tau_c^0(\phi = 0.6)$ (see Table 4.2).

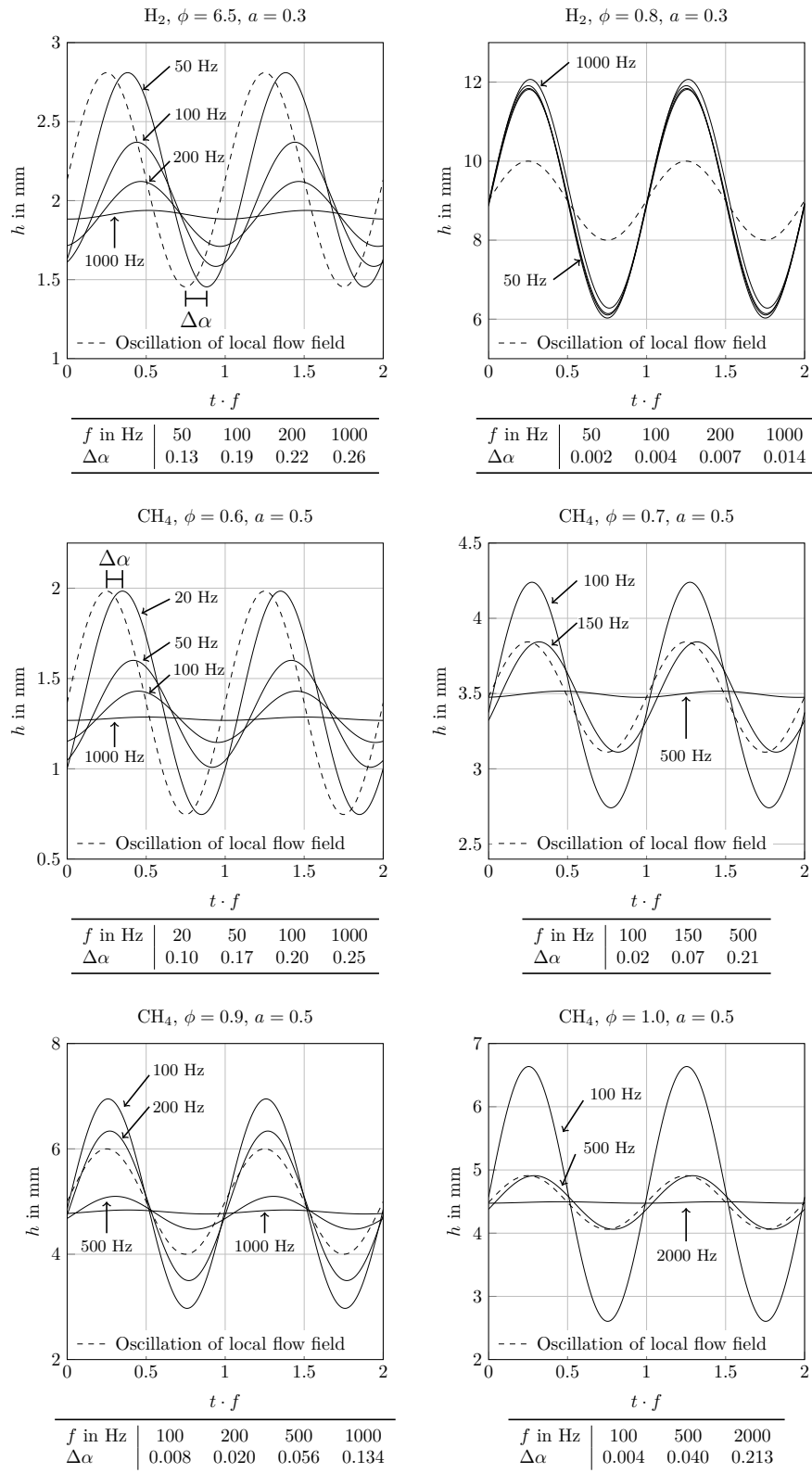


Figure 5.2: Temporal evolution of the flame tip position for different hydrogen and methane flames for fixed amplitudes. Dashed lines show the oscillation of the fluid flow field at the tip.

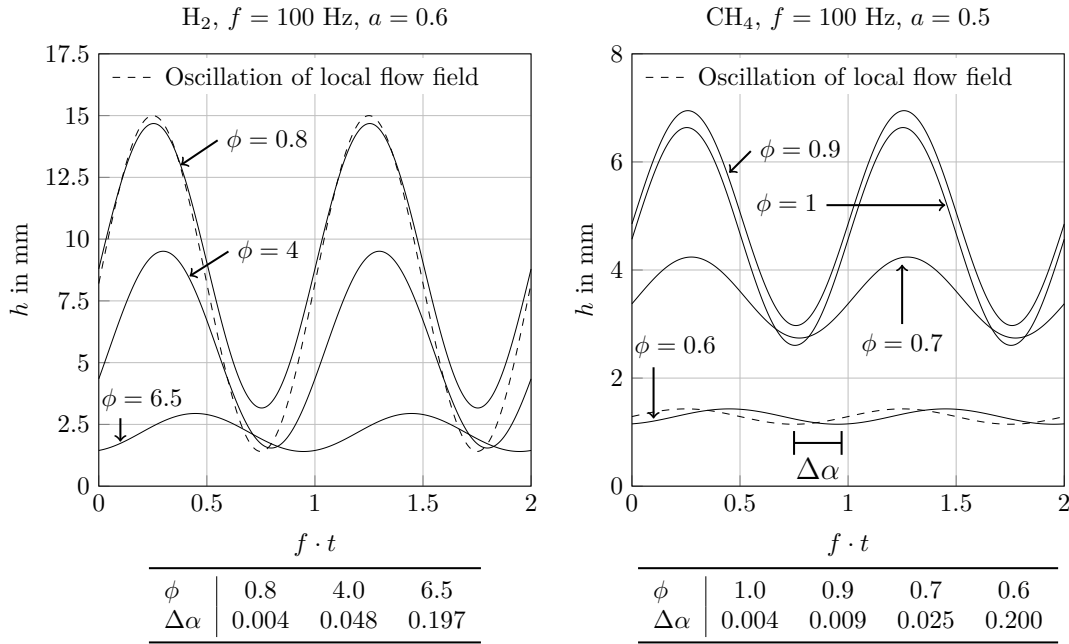


Figure 5.3: Temporal evolution of the flame tip position for hydrogen flames (left) and methane flames (right) for fixed amplitudes and frequency. Dashed lines show the oscillation of the fluid flow field at the tip.

- As the chemical time scale increases, the phase shift $\Delta\alpha$ increases as well.
- The movement of flames with higher chemical time scales is attenuated more strongly.
- Comparing the movement of the hydrogen flames on the left for $a = 0.6$ with the results in Figure 5.2 for $a = 0.3$ shows that a decrease in amplitude leads to lower displacements of the flame tip. The flame relaxation times however are the same for both amplitudes at $f = 100$ Hz.

Based on the phase shift $\Delta\alpha$ the flame relaxation time τ is defined as:

$$\tau \equiv \frac{\Delta\alpha}{f} \quad (5.2)$$

The flow is characterized by the Damköhler number Da_f :

$$Da_f \equiv \frac{\tau_{flow}}{\tau_{flame}} = \frac{1}{\tau_c^0 f} \quad (5.3)$$

For high Damköhler numbers $Da_f \gg 1$ (low frequencies) the flame reacts promptly to changing flow conditions because it has enough time to relax to a quasi-steady state, leading to flame relaxation times close to zero. For very low Damköhler numbers (high frequencies) the time scale of the flow is much smaller than the chemical time scale so that

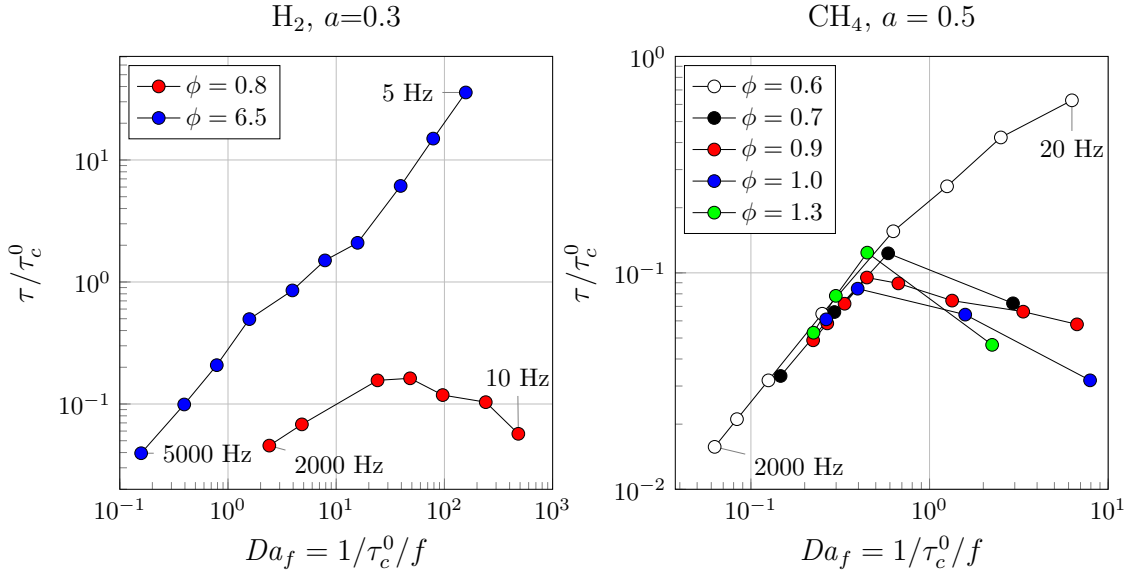


Figure 5.4: Normalized flame relaxation times over the Damköhler number of the flow for hydrogen flames (left) and methane flame (right).

the flame cannot react to flow disturbances, leading again to flame relaxation times close to zero. Additionally, if the flow is excited with very high frequencies, flow disturbances are not convected with the flow but propagate in the form of pressure waves which travel at the speed of sound. In Figure 5.4 the flame relaxation times normalized by the chemical time scale are plotted over the Damköhler numbers of the flow. For moderate Damköhler numbers, a maximum of the flame relaxation time can be found for the lean hydrogen flame at $Da_f \approx 50$ and for most of the methane flames at $Da_f \approx 0.6$. The rich hydrogen flame and the lean methane flame with $\phi = 0.6$, which have the highest chemical time scales, show no decrease in the range of high Damköhler numbers depicted here. Because very low frequencies are not relevant for turbulent flows and the simulations have to be run for a very long time, the bending points of those two flames are not computed.

The flame relaxation times discussed so far were computed for the movement of the flame tip position relative to the fluid flow. It is to be expected that flame relaxation times computed at other points along the flame front lead to different relaxation times, because the local chemical time scales depend on the local straining and curvature of the flame. For the lean hydrogen flames frequencies were limited to frequencies up to 2000 Hz. At higher frequencies the lean flames do not follow the fluid flow harmonically. In Figure 5.5, reaction rates of hydrogen are depicted for $\phi = 0.5$ at $a = 0.3$. On the top left at 100 Hz, the flame oscillates harmonically with the flow as shown in Figure 5.1. At 1000 Hz the flame becomes unstable and wrinkled. At 10000 Hz the flame does not react to the flow disturbances and does not move.

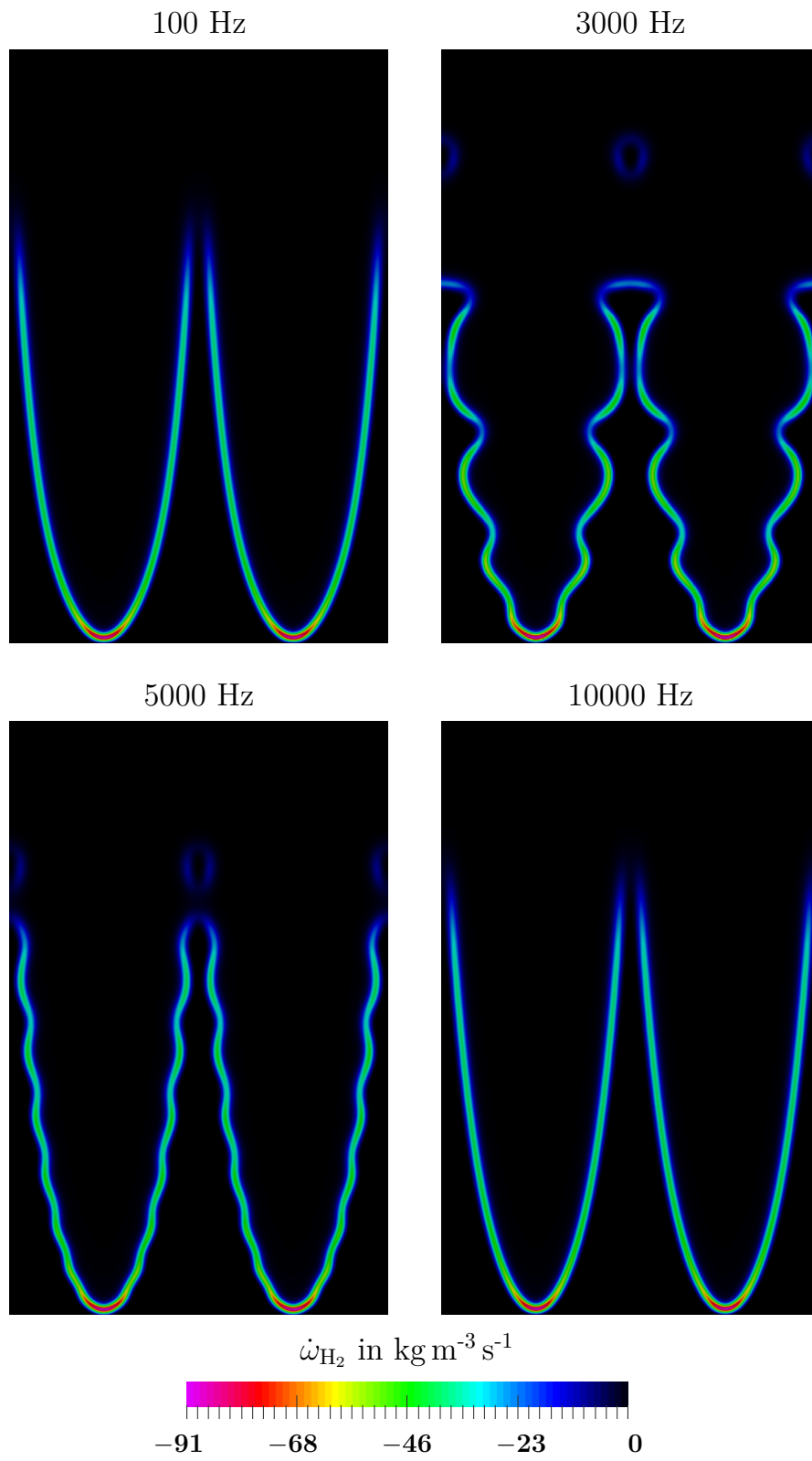


Figure 5.5: Reaction rates of hydrogen for $\phi = 0.5$ for different frequencies at $a = 0.3$.

5.3 Unsteady Markstein Numbers

Before time averaged Markstein numbers are computed, the correlation of flame speed and flame stretch is investigated for the oscillating flames at different phase angles within one oscillation period. In Figure 5.6 on the top left the correlation of flame speed with flame stretch is plotted for three phase angles as shown in the subplot in the top left figure: The moment when the flame reaches its steady state position at the upward motion $0.25f^{-1}$ (\bullet), the moment when the flame reaches its highest point at $0.5f^{-1}$ (\blacktriangle) and the steady-state position at the downward movement at $0.75f^{-1}$ (\blacksquare). The linear Markstein correlation can be applied for each of the three phase angles, yielding three different Markstein numbers. Comparing the top left and top right shows that an increase in amplitude a increases

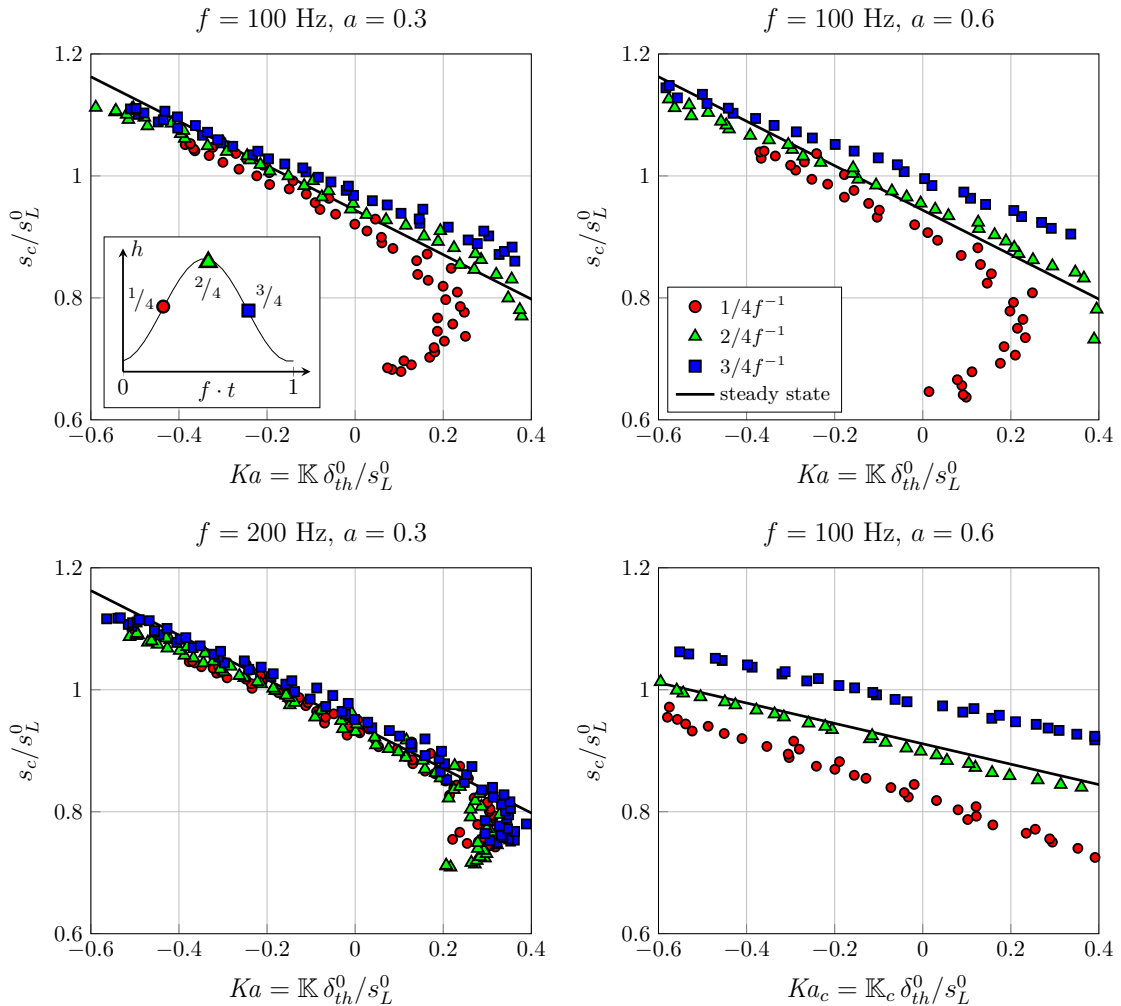


Figure 5.6: Correlation of flame speed and flame stretch for hydrogen with $\phi = 6.5$ evaluated at three phase angles within one oscillation for different frequencies and amplitudes.

the discrepancy of the Markstein numbers between the phase angles. Comparing the top left with the top right shows that an increase in frequency narrows the range of Markstein numbers because the movement of the flame is attenuated. On the bottom right, consumption speeds are plotted against the curvature term Ka_c showing qualitatively the same trends as the correlation of flame speed with total flame stretch Ka .

Figure 5.6 also demonstrates the effect of the flame relaxation time. For $f = 100$ Hz and $f = 200$ Hz the phase shift between the flame and the flow is about 0.2 (see Figure 5.2 on the top left). The same slope of flame speed with stretch as in the steady state (solid line) is obtained for the phase angle of $0.5f^{-1}$ (\blacktriangle). This is the phase angle corresponding to the highest displacement of the flame, not the steady-state position. But because $\Delta\alpha \approx 0.2$, the flame reacts to the flow conditions of a time $0.2 f^{-1}$ earlier where the flame was near the steady-state position. Similarly, the correlation at the phase angle $0.25f^{-1}$ (\bullet) shows the hook shaped distribution caused by non-adiabatic combustion due to heat losses to the inlet flow. It is the position half way between the lowest and highest point of the flame tip. Because of $\Delta\alpha \approx 0.2$, the flame still relaxes to a state, where the flame was near the inlet, explaining the hook shaped distribution at a time when the flame is already further away from the inlet.

In Figure 5.7 the correlation of flame speed with stretch is shown for hydrogen/air with $\phi = 0.8$ for three different phase angles. The correlations obtained at $f = 100$ Hz and $f = 200$ Hz are very similar due to the small flame relaxation time: At both frequencies, the flame reacts promptly to changing flow conditions. The correlations of the three instantaneous flame surfaces look similar to the steady-state flame with different mass flow rates in Figure 4.12 on the left. In the steady-state flame, the highest slope

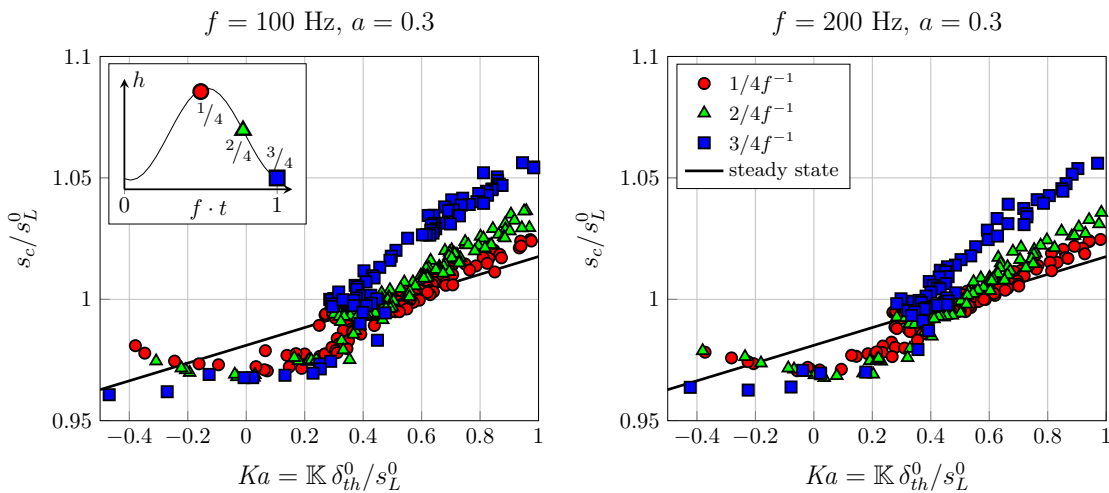


Figure 5.7: Correlation of flame speed and flame stretch for hydrogen with $\phi = 0.8$ evaluated at three phase angles within one oscillation period for different frequencies.

of s_c over Ka was obtained for the lowest mass flow rate and therefore shortest flame. The same is true for the oscillating flame, where the highest slope appears for the phase angle $0.75f^{-1}$ (■), where the flame is closest to the inlet and therefore is at its shortest length. The different Markstein numbers obtained for the three phase angles could be caused by different gradients of stretch along the flame surfaces as demonstrated for the steady-state flame. This would also explain why the discrepancy is highest in the positive Karlovitz range, where spatial stretch gradients differ the most in the steady-state flame (see section 4.3).

The time averaged Markstein numbers \overline{Ma} are obtained by linear regression over 10 phase angles within one oscillation period. This is illustrated as an example in Figure 5.8 for hydrogen with $\phi = 0.8$ and $f = 100$ Hz.

The averaged Markstein numbers for two hydrogen and two methane flames are shown in Figure 5.9. All Markstein numbers become smaller with increasing frequency. This means for the stable flames (both methane flames and the rich hydrogen flame) that the flame becomes less sensitive to stretch in an unsteady flow. The unstable hydrogen flame on the other hand becomes more sensitive to stretch, explaining that the turbulent flame speed of unstable flames increases faster with turbulent fluctuations than turbulent flame speeds of stable flames (see Figure 2.14). The averaged Markstein number \overline{Ma} is analogous to the effective Markstein number I_0Ma introduced in subsection 2.4.3. It has also been observed that higher amplitudes lead to a stronger decrease of \overline{Ma} . The decrease of the Markstein number can be reproduced by a power function of the Damköhler number. The

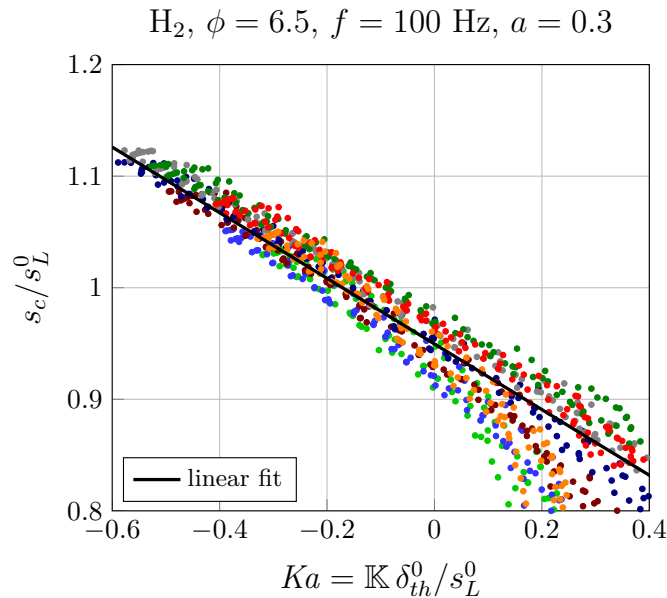


Figure 5.8: Example of the computation of time averaged Markstein numbers \overline{Ma} . Different colors indicate different phase angles.

solid lines shown in Figure 5.9 are fits of the form $\overline{Ma} = Ma_{steady} + c_1 Da_f^{c_2}$. This can be used to simulate the effect of unsteady stretching on local flame speeds in numerical simulations.

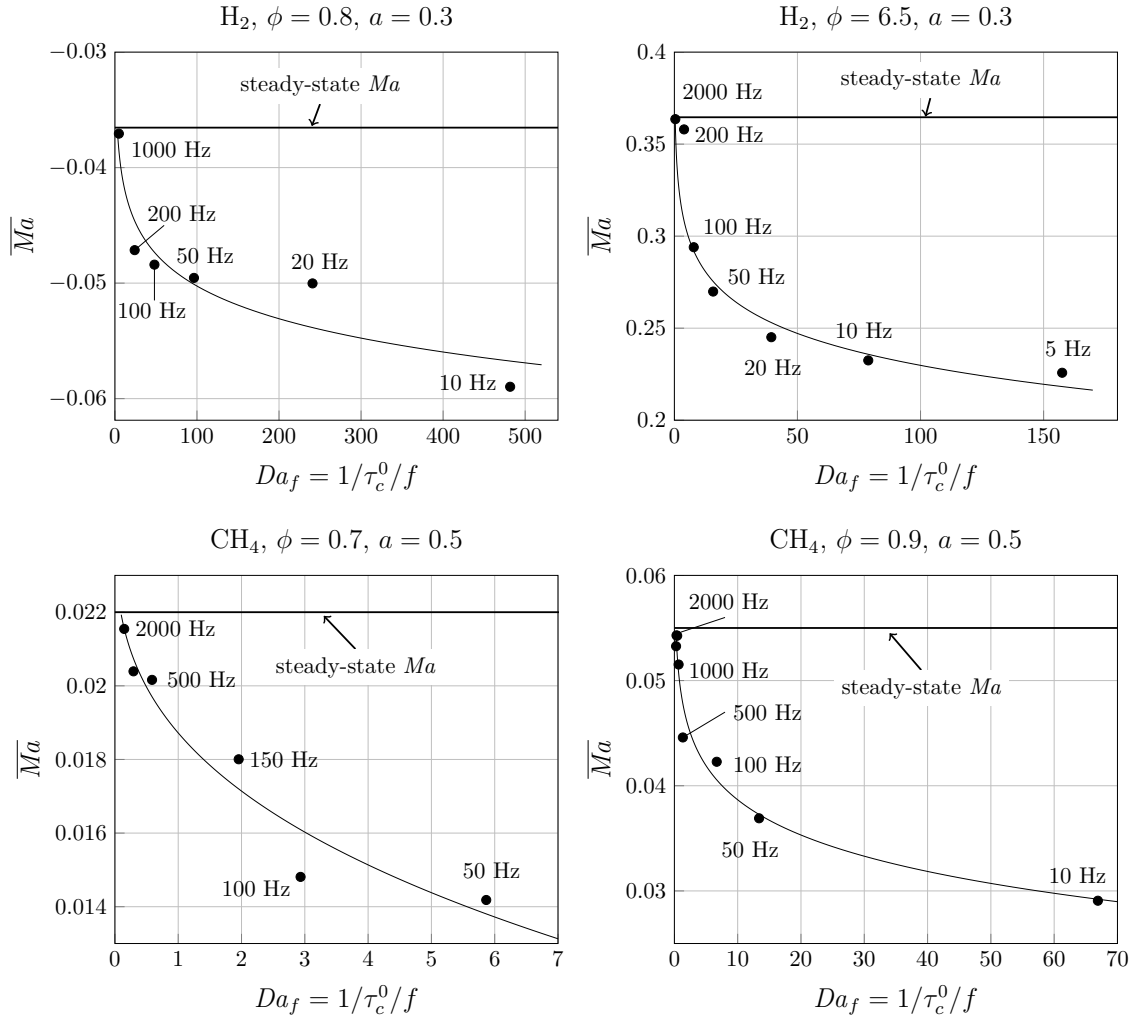


Figure 5.9: Time averaged Markstein numbers as a function of the Damköhler number of the flow. Solid lines are fitted power functions.

Summary and Outlook

6.1 Summary

Steady-state stretched flames have been simulated in order to investigate the effect of non-uniform stretching on local flame speeds. The linear Markstein correlation from the literature is applicable for small stretch rates and the dependence of consumption speeds on stretch, strain and curvature has been studied separately. In the steady state flames, the shape of the flame in terms of flame length can affect the Markstein numbers especially in regions where spatial flame stretch gradients along the flame front are changing.

Oscillating flames were simulated to investigate the flame response to unsteady stretching. For different phase angles within the oscillation period different Markstein numbers are obtained. The movement of the flame is attenuated for increasing frequencies and chemical time scales. The phase shift between the oscillation of the flame and the local flow field is found to be increased by high frequencies and chemical time scales. Based on the phase shift, flame relaxation times have been computed which are the time the flame needs to adapt to the changing flow conditions. For high Damköhler numbers the flame reacts faster to the changing conditions. For low Damköhler numbers or high frequencies, the flame cannot react to the flow because the time provided by the flow is too small. The large scattering of flame speeds and stretch values in turbulent flames can be explained by the flame relaxation time: Although two points on the flame surface may have the same instantaneous flame stretch, their flame speeds can be different because the flame may still adapt to stretch rates of previous times due to the relaxation time. Additionally, points with the same instantaneous flame stretch can experience different flame stretch gradients along the flame front which may change the local flame speeds as well.

Time averaged Markstein numbers have been computed which are generally lower than steady-state Markstein numbers and decrease with decreasing frequency. This behavior can be reproduced by a power function of the Damköhler number.

6.2 Outlook

The effect of unsteady stretching was investigated primarily in terms of frequencies in this thesis. More work is needed to compute the time averaged Markstein numbers in dependence on amplitude. The next step is to average these Markstein numbers over a frequency spectrum to emulate the influence of fully turbulent flows. The effect of flame stretch gradients along the flame needs to be quantified and flame relaxation times along the flame front—not only at the tip—need to be evaluated. Additionally, the pressure dependence was not part of this thesis but is very important as most technical combustion processes take place at elevated pressures.

Derivation of Stretch

Three derivations of general surface stretch are presented in this chapter.

A.1 Geometric Derivation of Stretch

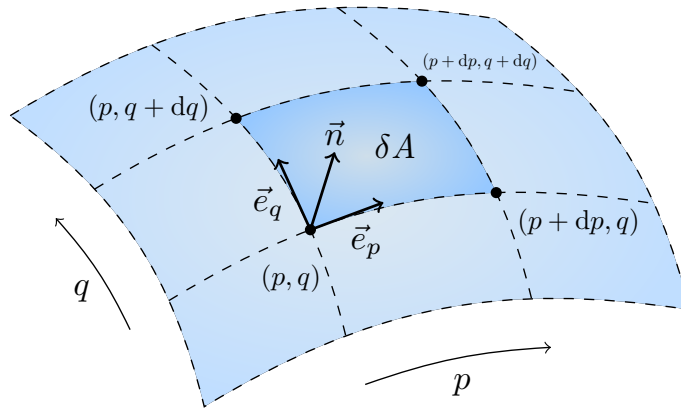


Figure A.1: The curvilinear coordinate system of a surface is spanned by the two unit vectors \vec{e}_p and \vec{e}_q . Each point is identified by its coordinates p and q .

The first derivation tracks the temporal evolution of surface elements [22]. Let p and q be the coordinates of the curvilinear coordinate system tangent to a surface (Fig. A.1). The location of any point on the surface can be identified by $\vec{r}(p, q, t)$ at a point in time t . The unit vectors of this surface coordinate system are:

$$\vec{e}_p = \frac{\frac{\partial \vec{r}}{\partial p}}{\left| \frac{\partial \vec{r}}{\partial p} \right|}, \quad \vec{e}_q = \frac{\frac{\partial \vec{r}}{\partial q}}{\left| \frac{\partial \vec{r}}{\partial q} \right|} \quad (\text{A.1})$$

The unit normal vector \vec{n} of the surface can be expressed as

$$\vec{n} = \vec{e}_p \times \vec{e}_q = \frac{\frac{\partial \vec{r}}{\partial p}}{\left| \frac{\partial \vec{r}}{\partial p} \right|} \times \frac{\frac{\partial \vec{r}}{\partial q}}{\left| \frac{\partial \vec{r}}{\partial q} \right|} \quad (\text{A.2})$$

To follow the convention of this thesis, \vec{e}_p and \vec{e}_q must be chosen in a way, that the unit normal vector \vec{n} points towards the fresh gas. Moving along the surface can be described by taking the total differential of the vector $\vec{r}(p, q, t)$, which points to the location of a point on the surface:

$$d\vec{r} = \frac{\partial \vec{r}}{\partial p} dp + \frac{\partial \vec{r}}{\partial q} dq + \frac{\partial \vec{r}}{\partial t} dt \quad (\text{A.3})$$

The path traveled in the p direction at a constant time ($dq = 0, dt = 0$) is the arc $(d\vec{s})_p$:

$$(d\vec{s})_p \equiv d\vec{r} = \frac{\partial \vec{r}}{\partial p} dp + \frac{\partial \vec{r}}{\partial q} \underbrace{dq}_{=0} + \frac{\partial \vec{r}}{\partial t} \underbrace{dt}_{=0} = \frac{\partial \vec{r}(p, q, t)}{\partial p} dp \quad (\text{A.4})$$

Analogously, moving only in the q direction at constant time t is described by:

$$(d\vec{s})_q = \frac{\partial \vec{r}(p, q, t)}{\partial q} dq \quad (\text{A.5})$$

The area of the parallelogram spanned by the two arc vectors is

$$\delta A(p, q, t) = \left| (d\vec{s})_p \times (d\vec{s})_q \right| = \left| \frac{\partial \vec{r}}{\partial p} dp \times \frac{\partial \vec{r}}{\partial q} dq \right| \quad (\text{A.6})$$

Using the identity

$$(f\vec{a}) \times \vec{b} = \vec{a} \times (f\vec{b}) = f(\vec{a} \times \vec{b}) \quad (\text{A.7})$$

with \vec{a} and \vec{b} arbitrary vectors and f a scalar, dp and dq can be moved outside the cross product:

$$\delta A(p, q, t) = \left| \frac{\partial \vec{r}}{\partial p} dp \times \frac{\partial \vec{r}}{\partial q} dq \right| = \left| dpdq \left(\frac{\partial \vec{r}}{\partial p} \times \frac{\partial \vec{r}}{\partial q} \right) \right| \quad (\text{A.8})$$

The vector norm for any scalar f times a vector \vec{a} can be written in Einstein notation as

$$|f\vec{a}| = \sqrt{f^2 a_i a_i} = \sqrt{f^2} \sqrt{a_i a_i} = f |\vec{a}|, \quad f \geq 0 \quad (\text{A.9})$$

Using this, Eq. (A.8) becomes:

$$\delta A(p, q, t) = \left| dpdq \left(\frac{\partial \vec{r}}{\partial p} \times \frac{\partial \vec{r}}{\partial q} \right) \right| = dpdq \left| \frac{\partial \vec{r}}{\partial p} \times \frac{\partial \vec{r}}{\partial q} \right| \quad (\text{A.10})$$

Eq. (A.10) can further be multiplied by

$$\left| \frac{\partial \vec{r}}{\partial p} \times \frac{\partial \vec{r}}{\partial q} \right| \frac{1}{\left| \frac{\partial \vec{r}}{\partial p} \right| \left| \frac{\partial \vec{r}}{\partial q} \right|} = 1 \quad (\text{A.11})$$

To show that Eq. (A.11) is true, the identity

$$\vec{a} \times \vec{b} = |\vec{a}| |\vec{b}| \sin(\Theta) \vec{n} \quad (\text{A.12})$$

is used. Noting that $\frac{\partial \vec{r}}{\partial p}$ and $\frac{\partial \vec{r}}{\partial q}$ are orthogonal and therefore $\sin \Theta = 1$, Eq. (A.11) becomes:

$$\left| \frac{\partial \vec{r}}{\partial p} \times \frac{\partial \vec{r}}{\partial q} \right| \frac{1}{\left| \frac{\partial \vec{r}}{\partial p} \right| \left| \frac{\partial \vec{r}}{\partial q} \right|} = \left| \frac{\partial \vec{r}}{\partial p} \right| \left| \frac{\partial \vec{r}}{\partial q} \right| \vec{n} \frac{1}{\left| \frac{\partial \vec{r}}{\partial p} \right| \left| \frac{\partial \vec{r}}{\partial q} \right|} \quad (\text{A.13})$$

Applying Eq. (A.9) yields:

$$\left| \frac{\partial \vec{r}}{\partial p} \right| \left| \frac{\partial \vec{r}}{\partial q} \right| \vec{n} \frac{1}{\left| \frac{\partial \vec{r}}{\partial p} \right| \left| \frac{\partial \vec{r}}{\partial q} \right|} = \left| \frac{\partial \vec{r}}{\partial p} \right| \left| \frac{\partial \vec{r}}{\partial q} \right| \underbrace{|\vec{n}|}_{=1} \frac{1}{\left| \frac{\partial \vec{r}}{\partial p} \right| \left| \frac{\partial \vec{r}}{\partial q} \right|} = 1 \quad (\text{A.14})$$

Multiplying Eq. (A.10) by Eq. (A.11) leads to

$$\delta A(p, q, t) = dpdq \left| \frac{\partial \vec{r}}{\partial p} \times \frac{\partial \vec{r}}{\partial q} \right|^2 \frac{1}{\left| \frac{\partial \vec{r}}{\partial p} \right| \left| \frac{\partial \vec{r}}{\partial q} \right|} \quad (\text{A.15})$$

The squared vector norm can be expressed as:

$$|\vec{a}|^2 = a_i a_i = \vec{a} \cdot \vec{a} \quad (\text{A.16})$$

Therefore, Eq. (A.15) becomes:

$$\delta A(p, q, t) = dpdq \left(\frac{\partial \vec{r}}{\partial p} \times \frac{\partial \vec{r}}{\partial q} \right) \cdot \left(\frac{\partial \vec{r}}{\partial p} \times \frac{\partial \vec{r}}{\partial q} \right) \frac{1}{\left| \frac{\partial \vec{r}}{\partial p} \right| \left| \frac{\partial \vec{r}}{\partial q} \right|} \quad (\text{A.17})$$

Using Eq. (A.7) to include the vector norms into the second cross product, the final expression for the surface element area can be written as:

$$\delta A(p, q, t) = dpdq \left(\frac{\partial \vec{r}}{\partial p} \times \frac{\partial \vec{r}}{\partial q} \right) \cdot \underbrace{\left(\frac{\frac{\partial \vec{r}}{\partial p}}{\left| \frac{\partial \vec{r}}{\partial p} \right|} \times \frac{\frac{\partial \vec{r}}{\partial q}}{\left| \frac{\partial \vec{r}}{\partial q} \right|} \right)}_{\equiv \vec{n}} = dpdq \left(\frac{\partial \vec{r}}{\partial p} \times \frac{\partial \vec{r}}{\partial q} \right) \cdot \vec{n} \quad (\text{A.18})$$

The location of the point (p, q) on the surface at $t' = t + \Delta t$ can be expressed by a first order Taylor expansion:

$$\vec{r}'(p, q, t + \Delta t) = \vec{r}(p, q, t) + \left. \frac{\partial \vec{r}}{\partial t} \right|_{p, q, t} \Delta t \quad (\text{A.19})$$

The absolute velocity of a point on the surface is \vec{w} . Since the coordinates of the point on the surface local curvilinear coordinate system stay the same [29], \vec{w} is

$$\vec{w} \equiv \frac{d\vec{r}}{dt} = \frac{\partial \vec{r}}{\partial t} \frac{dt}{dt} + \frac{\partial \vec{r}}{\partial p} \overbrace{\frac{dp}{dt}}^{=0} + \frac{\partial \vec{r}}{\partial q} \overbrace{\frac{dq}{dt}}^{=0} = \frac{\partial \vec{r}}{\partial t} \quad (\text{A.20})$$

Eq. (A.19) can therefore be recast into:

$$\vec{r}'(p, q, t + \Delta t) = \vec{r}(p, q, t) + \vec{w}(p, q, t)\Delta t \quad (\text{A.21})$$

Substituting Eq. (A.21) in Eq. (A.18) gives an expression for the surface element area at $t' = t + \Delta t$:

$$\begin{aligned} \delta A(p, q, t + \Delta t) &= dpdq \left(\frac{\partial \vec{r}'}{\partial p} \times \frac{\partial \vec{r}'}{\partial q} \right) \cdot \vec{n} \\ &= dpdq \left(\frac{\partial (\vec{r} + \vec{w}\Delta t)}{\partial p} \times \frac{\partial (\vec{r} + \vec{w}\Delta t)}{\partial q} \right) \cdot \vec{n} \end{aligned} \quad (\text{A.22})$$

The cross product in Eq. (A.22) can be expanded further. Using the product rule

$$\frac{\partial (\vec{a} + \vec{b})}{\partial x} = \frac{\partial \vec{a}}{\partial x} + \frac{\partial \vec{b}}{\partial x} \quad (\text{A.23})$$

yields

$$\frac{\partial (\vec{r} + \vec{w}\Delta t)}{\partial p} \times \frac{\partial (\vec{r} + \vec{w}\Delta t)}{\partial q} = \left(\frac{\partial \vec{r}}{\partial p} + \frac{\partial (\vec{w}\Delta t)}{\partial p} \right) \times \left(\frac{\partial \vec{r}}{\partial q} + \frac{\partial (\vec{w}\Delta t)}{\partial q} \right) \quad (\text{A.24})$$

Applying the vector identities

$$(\vec{a} + \vec{b}) \times \vec{c} = \vec{a} \times \vec{c} + \vec{b} \times \vec{c} \quad (\text{A.25})$$

$$\vec{a} \times \vec{b} = -\vec{b} \times \vec{a} \quad (\text{A.26})$$

and therefore

$$(\vec{a} + \vec{b}) \times (\vec{c} + \vec{d}) = \vec{a} \times \vec{c} + \vec{a} \times \vec{d} + \vec{b} \times \vec{c} + \vec{b} \times \vec{d} \quad (\text{A.27})$$

Eq. (A.24) becomes:

$$\frac{\partial \vec{r}}{\partial p} \times \frac{\partial \vec{r}}{\partial q} + \frac{\partial \vec{r}}{\partial p} \times \frac{\partial (\vec{w}\Delta t)}{\partial q} + \frac{\partial (\vec{w}\Delta t)}{\partial p} \times \frac{\partial \vec{r}}{\partial q} + \frac{\partial (\vec{w}\Delta t)}{\partial p} \times \frac{\partial (\vec{w}\Delta t)}{\partial q} \quad (\text{A.28})$$

Because Δt is not a function of p or q , it can be written outside the partial differential and

factored out of the cross product with Eq. (A.7) and substituted back into Eq. (A.22):

$$\begin{aligned} \delta A(p, q, t + \Delta t) = \\ \text{d}p\text{d}q \left(\frac{\partial \vec{r}}{\partial p} \times \frac{\partial \vec{r}}{\partial q} + \Delta t \frac{\partial \vec{r}}{\partial p} \times \frac{\partial \vec{w}}{\partial q} + \Delta t \frac{\partial \vec{w}}{\partial p} \times \frac{\partial \vec{r}}{\partial q} + \Delta t^2 \frac{\partial \vec{w}}{\partial p} \times \frac{\partial \vec{w}}{\partial q} \right) \cdot \vec{n} \end{aligned} \quad (\text{A.29})$$

The time derivative in the definition of stretch can be written in terms of the difference quotient:

$$\begin{aligned} \mathbb{K}(p, q, t) &= \frac{1}{\delta A(p, q, t)} \lim_{\Delta t \rightarrow 0} \frac{1}{\Delta t} (\delta A(p, q, t + \Delta t) - \delta A(p, q, t)) \\ &= \lim_{\Delta t \rightarrow 0} \frac{\frac{1}{\Delta t} (\delta A(p, q, t + \Delta t) - \delta A(p, q, t))}{\delta A(p, q, t)} \end{aligned} \quad (\text{A.30})$$

$\delta A(p, q, t)$ can be put inside the limit because it is not a function of Δt . Inserting the expressions for the infinitesimal areas from Eq. (A.18) and Eq. (A.29), the stretch becomes:

$$\lim_{\Delta t \rightarrow 0} \frac{\frac{1}{\Delta t} \left(\text{d}p\text{d}q \left(\frac{\partial \vec{r}}{\partial p} \times \frac{\partial \vec{r}}{\partial q} + \Delta t \frac{\partial \vec{r}}{\partial p} \times \frac{\partial \vec{w}}{\partial q} + \Delta t \frac{\partial \vec{w}}{\partial p} \times \frac{\partial \vec{r}}{\partial q} + \Delta t^2 \frac{\partial \vec{w}}{\partial p} \times \frac{\partial \vec{w}}{\partial q} \right) \cdot \vec{n} - \text{d}p\text{d}q \left(\frac{\partial \vec{r}}{\partial p} \times \frac{\partial \vec{r}}{\partial q} \right) \cdot \vec{n} \right)}{\text{d}p\text{d}q \left(\frac{\partial \vec{r}}{\partial p} \times \frac{\partial \vec{r}}{\partial q} \right) \cdot \vec{n}} \quad (\text{A.31})$$

Canceling $\text{d}p$, $\text{d}q$ and Δt and using the vector identity

$$\vec{a} \cdot \vec{c} \pm \vec{b} \cdot \vec{c} = (\vec{a} \pm \vec{b}) \cdot \vec{c} \quad (\text{A.32})$$

the stretch expression becomes:

$$\lim_{\Delta t \rightarrow 0} \frac{\left(\frac{1}{\Delta t} \frac{\partial \vec{r}}{\partial p} \times \frac{\partial \vec{r}}{\partial q} + \frac{\partial \vec{r}}{\partial p} \times \frac{\partial \vec{w}}{\partial q} + \frac{\partial \vec{w}}{\partial p} \times \frac{\partial \vec{r}}{\partial q} + \Delta t \frac{\partial \vec{w}}{\partial p} \times \frac{\partial \vec{w}}{\partial q} - \frac{1}{\Delta t} \frac{\partial \vec{r}}{\partial p} \times \frac{\partial \vec{r}}{\partial q} \right) \cdot \vec{n}}{\left(\frac{\partial \vec{r}}{\partial p} \times \frac{\partial \vec{r}}{\partial q} \right) \cdot \vec{n}} \quad (\text{A.33})$$

The first and last term in the numerator cancel each other. The fourth term vanishes, as Δt approaches zero. After evaluating the limit, the stretch can be simplified to:

$$\mathbb{K}(p, q, t) = \frac{\left(\frac{\partial \vec{r}}{\partial p} \times \frac{\partial \vec{w}}{\partial q} + \frac{\partial \vec{w}}{\partial p} \times \frac{\partial \vec{r}}{\partial q} \right) \cdot \vec{n}}{\left(\frac{\partial \vec{r}}{\partial p} \times \frac{\partial \vec{r}}{\partial q} \right) \cdot \vec{n}} \quad (\text{A.34})$$

Choosing the scale factors

$$\left| \frac{\partial \vec{r}}{\partial p} \right| = \left| \frac{\partial \vec{r}}{\partial q} \right| = 1 \quad (\text{A.35})$$

for this particular curvilinear coordinate system, the unit vectors (see Eq. (A.1) and

Eq. (A.2)) simplify to:

$$\vec{e}_p = \frac{\partial \vec{r}}{\partial p}, \quad \vec{e}_q = \frac{\partial \vec{r}}{\partial q} \quad (\text{A.36})$$

$$\vec{n} = \vec{e}_p \times \vec{e}_q = \frac{\partial \vec{r}}{\partial p} \times \frac{\partial \vec{r}}{\partial q} \quad (\text{A.37})$$

Substituting the new unit vectors into Eq. (A.34), the denominator becomes $\vec{n} \cdot \vec{n} = |\vec{n}|^2 = 1$ and the stretch reads:

$$\mathbb{K}(p, q, t) = \left(\vec{e}_p \times \frac{\partial \vec{w}}{\partial q} + \frac{\partial \vec{w}}{\partial p} \times \vec{e}_q \right) \cdot \vec{n} \quad (\text{A.38})$$

This can further be rearranged with Eq. (A.32) to:

$$\mathbb{K}(p, q, t) = \left(\vec{e}_p \times \frac{\partial \vec{w}}{\partial q} \right) \cdot \vec{n} + \left(\frac{\partial \vec{w}}{\partial p} \times \vec{e}_q \right) \cdot \vec{n} \quad (\text{A.39})$$

Using the vector identity

$$\left(\vec{b} \times \vec{c} \right) \cdot \vec{a} = \left(\vec{c} \times \vec{a} \right) \cdot \vec{b} = \left(\vec{a} \times \vec{b} \right) \cdot \vec{c} \quad (\text{A.40})$$

the stretch becomes:

$$\mathbb{K}(p, q, t) = \left(\vec{n} \times \vec{e}_p \right) \cdot \frac{\partial \vec{w}}{\partial q} + \left(\vec{e}_q \times \vec{n} \right) \cdot \frac{\partial \vec{w}}{\partial p} \quad (\text{A.41})$$

$\vec{n} \times \vec{e}_p$ and $\vec{e}_q \times \vec{n}$ can be simplified to \vec{e}_q and \vec{e}_p , respectively. To demonstrate this, take the cross product of Eq. (A.2) and \vec{e}_p :

$$\vec{n} \times \vec{e}_p = \left(\vec{e}_p \times \vec{e}_q \right) \times \vec{e}_p \quad (\text{A.42})$$

The relation for the triple cross product

$$\left(\vec{a} \times \vec{b} \right) \times \vec{c} = \left(\vec{c} \cdot \vec{a} \right) \vec{b} - \left(\vec{c} \cdot \vec{b} \right) \vec{a} \quad (\text{A.43})$$

can be used to rewrite the r.h.s. of Eq. (A.42) to:

$$\vec{n} \times \vec{e}_p = \underbrace{\left(\vec{e}_p \cdot \vec{e}_p \right)}_{=|\vec{e}_p|^2} \vec{e}_q - \underbrace{\left(\vec{e}_p \cdot \vec{e}_q \right)}_{=0} \vec{e}_p \quad (\text{A.44})$$

Since \vec{e}_p and \vec{e}_q are orthogonal, $\vec{e}_p \cdot \vec{e}_q = 0$. And because \vec{e}_p and \vec{e}_q are unit vectors, $|\vec{e}_p| = 1$. Therefore

$$\vec{n} \times \vec{e}_p = \vec{e}_q \quad (\text{A.45})$$

Analogously, by taking the cross product of \vec{e}_q and Eq. (A.2)

$$\vec{e}_q \times \vec{n} = \vec{e}_q \times (\vec{e}_p \times \vec{e}_q) \quad (\text{A.46})$$

and using Eq. (A.26) to rewrite the vector identity to

$$\vec{a} \times (\vec{b} \times \vec{c}) = \vec{b}(\vec{a} \cdot \vec{c}) - \vec{c}(\vec{a} \cdot \vec{b}) \quad (\text{A.47})$$

one obtains

$$\vec{e}_q \times \vec{n} = \vec{e}_p \underbrace{(\vec{e}_q \cdot \vec{e}_q)}_{=|\vec{e}_q|^2=1} - \vec{e}_q \underbrace{(\vec{e}_q \cdot \vec{e}_p)}_{=0} = \vec{e}_p \quad (\text{A.48})$$

Therefore, the stretch reads:

$$\mathbb{K}(p, q, t) = \vec{e}_p \cdot \frac{\partial \vec{w}}{\partial p} + \vec{e}_q \cdot \frac{\partial \vec{w}}{\partial q} \quad (\text{A.49})$$

With the definition of the surface gradient operator ∇_t

$$\nabla_t \equiv \vec{e}_p \frac{\partial}{\partial p} + \vec{e}_q \frac{\partial}{\partial q} \quad (\text{A.50})$$

Eq. (A.49) finally becomes:

$$\mathbb{K}(p, q, t) = \nabla_t \cdot \vec{w} \quad (\text{A.51})$$

A.2 Reynolds Transport Theorem

An alternative derivation uses the Reynolds transport theorem for material surfaces

$$\frac{d}{dt} \int \vec{a} \cdot d\vec{A} = \frac{d}{dt} \int \vec{a} \cdot \vec{n} dA \quad (\text{A.52})$$

where \vec{a} is an arbitrary vector field. Note, that this form differs from the Reynolds transport theorem for material volumes, since the area integral cannot be converted into a volume integral using the divergence theorem because the area in Eq. (A.52) is not necessarily closed (and cannot be closed in the case presented below to derive the stretch term). This theorem represents a generalization of the two-dimensional Leibniz integral rule.

A simplified but descriptive derivation of the Reynolds transport theorem for material surfaces starts by expressing the total time derivative in Eq. (A.52) with a difference

quotient:

$$\frac{d}{dt} \int \vec{a} \cdot \vec{n} dA = \lim_{\Delta t \rightarrow 0} \frac{1}{\Delta t} \left(\int_{A(t+\Delta t)} \vec{a}(t+\Delta t) \cdot \vec{n} dA - \int_{A(t)} \vec{a}(t) \cdot \vec{n} dA \right) \quad (\text{A.53})$$

The r.h.s. is expanded by

$$0 = - \int_{A(t+\Delta t)} \vec{a}(t) \cdot \vec{n} dA + \int_{A(t+\Delta t)} \vec{a}(t) \cdot \vec{n} dA \quad (\text{A.54})$$

to yield:

$$\frac{d}{dt} \int \vec{a} \cdot \vec{n} dA = \lim_{\Delta t \rightarrow 0} \frac{1}{\Delta t} \left(\int_{A(t+\Delta t)} \vec{a}(t+\Delta t) \cdot \vec{n} dA - \int_{A(t+\Delta t)} \vec{a}(t) \cdot \vec{n} dA + \int_{A(t+\Delta t)} \vec{a}(t) \cdot \vec{n} dA - \int_{A(t)} \vec{a}(t) \cdot \vec{n} dA \right) \quad (\text{A.55})$$

The first two terms on the r.h.s. have the same integration boundaries and can therefore be combined to:

$$\lim_{\Delta t \rightarrow 0} \frac{1}{\Delta t} \int_{A(t+\Delta t)} (\vec{a}(t+\Delta t) - \vec{a}(t)) \cdot \vec{n} dA = \lim_{\Delta t \rightarrow 0} \int_{A(t+\Delta t)} \frac{\vec{a}(t+\Delta t) - \vec{a}(t)}{\Delta t} \cdot \vec{n} dA \quad (\text{A.56})$$

Because Δt is a constant, it can be moved into the integral. As the limit approaches zero, the last term becomes:

$$\lim_{\Delta t \rightarrow 0} \int_{A(t+\Delta t)} \frac{\vec{a}(t+\Delta t) - \vec{a}(t)}{\Delta t} \cdot \vec{n} dA = \int_{A(t)} \frac{\partial \vec{a}}{\partial t} \cdot \vec{n} dA \quad (\text{A.57})$$

The last two terms in Eq. (A.55) describe the integration of $\vec{a}(t)$ over two different areas. Instead of evaluating the integrals separately, a new area is introduced. As the area $A(t)$ moves towards $A(t+\Delta t)$, its edge $C(t)$ sweeps over an area $A_{Connect}$. The surface $A_{Connect}$ connects the edges of $A(t)$ and $A(t+\Delta t)$, forming a closed surface. This is illustrated in Figure A.2

Because the new area $A_{Connect}$ is not part of the two original surfaces $A(t)$ and $A(t+\Delta t)$, it has to be subtracted (see Figure A.2):

$$\int_{A(t+\Delta t)} \vec{a}(t) \cdot \vec{n} dA - \int_{A(t)} \vec{a}(t) \cdot \vec{n} dA = \oint \vec{a}(t) \cdot \vec{n} dA - \int_{A_{Connect}} \vec{a}(t) \cdot \vec{n} dA \quad (\text{A.58})$$

Note, that the surfaces $A(t)$ and $A(t+\Delta t)$ have the same orientation, that is, \vec{n} pointing

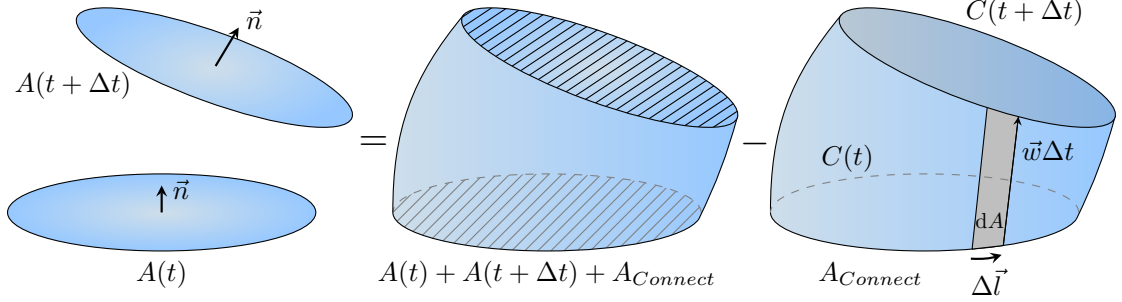


Figure A.2: As the surface $A(t)$ moves towards $A(t+\Delta t)$, its edge $C(t)$ sweeps over an area $A_{Connect}$ that connects the edges $C(t)$ and $C(t+\Delta t)$. Together with $A_{Connect}$, $A(t)$ and $A(t+\Delta t)$ form a closed surface. Subtracting the new area $A_{Connect}$ from the closed surface yields the original two surfaces.

upwards in this example. The unit normal vectors of the closed surface, however, point outwards. Therefore, the normal vector of the closed surface at the bottom points downwards, leading to the minus sign before the second term on the l.h.s. of Eq. (A.58). Now that the first integral on the r.h.s. covers a closed surface, the divergence theorem can be used to express it as a volume integral:

$$\oint \vec{a}(t) \cdot \vec{n} dA = \int \nabla \cdot \vec{a}(t) dV \quad (\text{A.59})$$

The volume enclosed by the closed surface (middle of Figure A.2) is the volume swept over by $A(t)$ as it moves towards $A(t+\Delta t)$ with the velocity \vec{w} . It can therefore be approximated by the area $A(t)$ moving with the velocity \vec{w} for a time of Δt

$$dV = \vec{w} dt dA \quad (\text{A.60})$$

with $dt \approx \Delta t$, so that the volume integral becomes:

$$\oint \vec{a}(t) \cdot \vec{n} dA = \int_{A(t)} \nabla \cdot \vec{a}(t) dV = \int_{A(t)} \nabla \cdot \vec{a}(t) \vec{w} \cdot \vec{n} dA \Delta t \quad (\text{A.61})$$

Using a similar argument, the integral over the area $A_{Connect}$ can be expressed by the area swept over by the edge $C(t)$ moving with the velocity \vec{w} for a time of Δt . The tangent line vector of $C(t)$ is \vec{l} . The area between the two vectors $\vec{w}\Delta t$ and $\Delta\vec{l}$ (gray area dA in Figure A.2) can be expressed by the cross product

$$\vec{n} dA = d\vec{A} = d\vec{l} \times \vec{w} dt \quad (\text{A.62})$$

The surface integral can be rewritten to:

$$-\int_{A_{Connect}} \vec{a}(t) \cdot d\vec{A} = -\int_{A_{Connect}} \vec{a}(t) \cdot d\vec{l} \times \vec{w} dt \quad (\text{A.63})$$

With $dt \approx \Delta t$ and $d\vec{l} \approx \Delta\vec{l}$, the integrand becomes

$$\vec{a}(t) \cdot d\vec{l} \times \vec{w} dt = \vec{a}(t) \cdot \Delta\vec{l} \times \vec{w} \Delta t \quad (\text{A.64})$$

Using the vector identity

$$\vec{a} \cdot (\vec{b} \times \vec{c}) = \vec{b} \cdot (\vec{c} \times \vec{a}) \quad (\text{A.65})$$

the integrand becomes:

$$\vec{a}(t) \cdot \Delta\vec{l} \times \vec{w} \Delta t = (\vec{w} \times \vec{a}(t)) \cdot \Delta\vec{l} \Delta t \quad (\text{A.66})$$

With $\Delta\vec{l} \approx d\vec{l}$ and noting that Δt is constant, the integral becomes:

$$-\int_{A_{Connect}} \vec{a}(t) \cdot d\vec{l} \times \vec{w} dt = -\Delta t \oint_{C(t)} (\vec{w} \times \vec{a}(t)) \cdot d\vec{l} \quad (\text{A.67})$$

Using Stokes' theorem, this closed line integral can be rewritten to a surface integral:

$$-\Delta t \oint_{C(t)} (\vec{w} \times \vec{a}(t)) \cdot d\vec{l} = -\Delta t \int_{A(t)} \nabla \times (\vec{w} \times \vec{a}(t)) \cdot \vec{n} dA \quad (\text{A.68})$$

Now, Eq. (A.58) can be expressed by substituting the first term on the r.h.s. with Eq. (A.61) and the second term with Eq. (A.68):

$$\begin{aligned} & \int_{A(t+\Delta t)} \vec{a}(t) \cdot \vec{n} dA - \int_{A(t)} \vec{a}(t) \cdot \vec{n} dA \\ &= \int_{A(t)} \nabla \cdot \vec{a}(t) \vec{w} \cdot \vec{n} dA \Delta t - \Delta t \int_{A(t)} \nabla \times (\vec{w} \times \vec{a}(t)) \cdot \vec{n} dA \\ &= \Delta t \left(\int_{A(t)} \nabla \cdot \vec{a}(t) \vec{w} \cdot \vec{n} dA - \int_{A(t)} \nabla \times (\vec{w} \times \vec{a}(t)) \cdot \vec{n} dA \right) \end{aligned} \quad (\text{A.69})$$

Finally, by substituting Eq. (A.57) for the first two terms in Eq. (A.55) and Eq. (A.69) for

the last two terms in Eq. (A.55), the Reynolds transport theorem simplifies to:

$$\begin{aligned} & \frac{d}{dt} \int \vec{a} \cdot \vec{n} \, dA \\ &= \int \frac{\partial \vec{a}}{\partial t} \cdot \vec{n} \, dA + \lim_{\Delta t \rightarrow 0} \frac{\Delta t}{\Delta t} \left(\int \nabla \cdot \vec{a} (\vec{w} \cdot \vec{n}) \, dA - \int \nabla \times (\vec{w} \times \vec{a}) \cdot \vec{n} \, dA \right) \end{aligned} \quad (\text{A.70})$$

where t as an argument has been omitted since all quantities are evaluated at t . Both Δt cancel out and because the remaining three integrals have the same boundaries, they can be combined to:

$$\boxed{\frac{d}{dt} \int \vec{a} \cdot \vec{n} \, dA = \int \left(\frac{\partial \vec{a}}{\partial t} + \vec{w} \nabla \cdot \vec{a} - \nabla \times (\vec{w} \times \vec{a}) \right) \cdot \vec{n} \, dA} \quad (\text{A.71})$$

This is the Reynold Transport Theorem for material surfaces [33, 34, 68]. The last term can alternatively be expressed as a line integral using Stoke's theorem:

$$\boxed{\frac{d}{dt} \int_A \vec{a} \cdot \vec{n} \, dA = \int_A \left(\frac{\partial \vec{a}}{\partial t} + \vec{w} \nabla \cdot \vec{a} \right) \cdot \vec{n} \, dA - \oint_C (\vec{w} \times \vec{a}) \cdot d\vec{l}} \quad (\text{A.72})$$

where C is the edge of A .

To derive an expression for stretch from this equation, the vector \vec{a} is replaced by the unit normal vector \vec{n} . With this substitution, Eq. (A.71) becomes:

$$\frac{d}{dt} \int \underbrace{\vec{n} \cdot \vec{n}}_{=1} \, dA = \int \left(\frac{\partial \vec{n}}{\partial t} + \vec{w} \nabla \cdot \vec{n} - \nabla \times (\vec{w} \times \vec{n}) \right) \cdot \vec{n} \, dA \quad (\text{A.73})$$

$$\frac{d}{dt} \int dA = \int \underbrace{\frac{\partial \vec{n}}{\partial t} \cdot \vec{n}}_{=0} \, dA + \int (\vec{w} \nabla \cdot \vec{n} - \nabla \times (\vec{w} \times \vec{n})) \cdot \vec{n} \, dA \quad (\text{A.74})$$

The first term on the r.h.s. is zero because

$$\frac{\partial \vec{n}}{\partial t} \cdot \vec{n} = \frac{\partial \frac{1}{2} \overbrace{(\vec{n} \cdot \vec{n})}^{=1}}{\partial t} = 0 \quad (\text{A.75})$$

Integrating Eq. (A.74) over the area of an infinitesimal area element δA , which is never a closed surface, yields:

$$\frac{d}{dt} \underbrace{\int_{\delta A} dA}_{=\delta A} = \int_{\delta A} (\vec{w} \nabla \cdot \vec{n} - \nabla \times (\vec{w} \times \vec{n})) \cdot \vec{n} \, dA \quad (\text{A.76})$$

Because δA is an infinitesimal area element, the integral on the right hand side can be simplified to

$$\frac{d\delta A}{dt} = (\vec{w}\nabla \cdot \vec{n} - \nabla \times (\vec{w} \times \vec{n})) \cdot \vec{n} \delta A \quad (\text{A.77})$$

Dividing by δA yields the familiar expression for stretch [16, 49, 50, 56, 61]

$$\mathbb{K} \equiv \frac{1}{\delta A} \frac{d(\delta A)}{dt} = (\vec{w}\nabla \cdot \vec{n} - \nabla \times (\vec{w} \times \vec{n})) \cdot \vec{n} \quad (\text{A.78})$$

$$= (\vec{w} \cdot \vec{n}) \nabla \cdot \vec{n} - \vec{n} \cdot \nabla \times (\vec{w} \times \vec{n}) \quad (\text{A.79})$$

Another expression can be recovered by using the vector calculus identity

$$\vec{a}\nabla \cdot \vec{b} - \nabla \times (\vec{a} \times \vec{b}) = \vec{b}\nabla \cdot \vec{a} - \vec{b} \cdot \nabla \vec{a} + \vec{a} \cdot \nabla \vec{b} \quad (\text{A.80})$$

with $\vec{a} \equiv \vec{w}$ and $\vec{b} \equiv \vec{n}$ for the r.h.s. of Eq. (A.78):

$$\begin{aligned} \mathbb{K} &= (\vec{w}\nabla \cdot \vec{n} - \nabla \times (\vec{w} \times \vec{n})) \cdot \vec{n} = (\vec{n}\nabla \cdot \vec{w} - \vec{n} \cdot \nabla \vec{w} + \vec{w} \cdot \nabla \vec{n}) \cdot \vec{n} \\ &= \underbrace{\vec{n} \cdot \vec{n}}_{=1} \nabla \cdot \vec{w} - \vec{n} \cdot \vec{n} \cdot \nabla \vec{w} + \underbrace{\vec{n} \cdot \vec{w}}_{=0} \cdot \nabla \vec{n} \end{aligned} \quad (\text{A.81})$$

where the last term is zero because

$$\vec{n} \cdot \vec{w} \cdot \nabla \vec{n} = \vec{w} \cdot \nabla \left(\overbrace{\frac{1}{2} \vec{n} \cdot \vec{n}}^{=1} \right) = 0 \quad (\text{A.82})$$

and the first two terms of the last line in Eq. (A.81) are [13, 17, 22, 75, 77, 78]

$$\mathbb{K} = \nabla \cdot \vec{w} - \vec{n} \cdot \vec{n} \cdot \nabla \vec{w} = (\mathbf{I} - \vec{n}\vec{n}) : \nabla \vec{w} \equiv \nabla_t \cdot \vec{w} \quad (\text{A.83})$$

A.3 Volume Element Analogy

An even more simplified derivation starts with the temporal change of a volume element. Its volume changes because of the movement of its boundaries [3]:

$$\frac{dV}{dt} = \oint \vec{w} \cdot d\vec{A} = \oint \vec{w} \cdot \vec{n} dA \quad (\text{A.84})$$

The velocity at which the boundaries are moving is \vec{w} . Since this volume element is closed, the divergence theorem can be used to obtain

$$\frac{dV}{dt} = \oint \vec{w} \cdot \vec{n} dA = \int \nabla \cdot \vec{w} dV \quad (\text{A.85})$$

and thereby connecting the movement of the volume elements boundaries with the divergence boundary velocity field. More generally, divergence of an arbitrary vector field \vec{a} is defined in terms of the surface integral over the volume element V :

$$\lim_{V \rightarrow 0} \frac{1}{V} \oint \vec{a} \cdot \vec{n} dA \equiv \nabla \cdot \vec{a} \quad (\text{A.86})$$

The infinitesimal volume element will be denoted as $\lim_{V \rightarrow 0} V \equiv \delta V$. Dividing Eq. (A.85) by δV , substituting \vec{a} by \vec{w} and comparing with Eq. (A.86), the fractal volume dilatation is simply written as:

$$\frac{1}{\delta V} \frac{d(\delta V)}{dt} = \frac{1}{\delta V} \oint \vec{w} \cdot \vec{n} dA \equiv \nabla \cdot \vec{w} \quad (\text{A.87})$$

The volume of the infinitesimal volume element can be expressed by a surface area δA multiplied by its thickness in the normal direction h or δh . Imagine for example a volume element in the shape of a cylinder, with the area of its base δA and height δh . The volume is therefore:

$$dV = dA dh \quad \text{or} \quad \delta V \approx \delta A \delta h \quad (\text{A.88})$$

Substituting the second expression into the total derivative of Eq. (A.87) and applying the product rule yields:

$$\frac{1}{\delta V} \frac{d(\delta V)}{dt} = \frac{1}{\delta A \delta h} \frac{d(\delta A \delta h)}{dt} = \frac{1}{\delta A} \frac{d(\delta A)}{dt} + \frac{1}{\delta h} \frac{d(\delta h)}{dt} = \nabla \cdot \vec{w} \quad (\text{A.89})$$

The change in thickness can be expressed by the movement of the two boundaries [24]:

$$\frac{d}{dt} \delta h \approx \vec{n} \cdot (\vec{w}(\vec{p} + \vec{n} \delta h) - \vec{w}(\vec{p})) \quad (\text{A.90})$$

where \vec{p} is the position vector of one of the boundaries. The velocity at $\vec{p} + \vec{n} \delta h$ can be expressed with a first order Taylor approximation:

$$\vec{w}(\vec{p} + \vec{n} \delta h) \approx \vec{w}(\vec{p}) + \frac{\partial \vec{w}}{\partial n} \delta h \quad (\text{A.91})$$

Substituting this back into Eq. (A.90) yields:

$$\frac{d}{dt} \delta h \approx \vec{n} \cdot \frac{\partial \vec{w}}{\partial n} \delta h \quad (\text{A.92})$$

Dividing this by δh and noting that the directional derivative is $\frac{\partial}{\partial n} \equiv \vec{n} \cdot \nabla$, Eq. (A.89) becomes [3, 24]:

$$\nabla \cdot \vec{w} = \frac{1}{\delta A} \frac{d(\delta A)}{dt} + \frac{1}{\delta h} \frac{d(\delta h)}{dt} = \frac{1}{\delta A} \frac{d(\delta A)}{dt} + \vec{n} \cdot \vec{n} \cdot \nabla \vec{w} \quad (\text{A.93})$$

or

$$\mathbb{K} \equiv \frac{1}{\delta A} \frac{d(\delta A)}{dt} = \nabla \cdot \vec{w} - \vec{n} \cdot \vec{n} \cdot \nabla \vec{w} \quad (\text{A.94})$$

Therefore, the stretch of the volume element's surface reduces to the tangential divergence of its velocity $\mathbb{K} = \nabla_t \cdot \vec{w} \equiv \nabla \cdot \vec{w} - \vec{n} \cdot \vec{n} \cdot \nabla \vec{w}$.

Reaction Mechanisms

In this appendix, the reaction mechanisms used in the thesis are listed in the CHEMKIN input file format.

B.1 Hydrogen Mechanism by Li et al.

The mechanism by Li. et al. [55] is used for the hydrogen combustion cases:

```

ELEMENTS H O N END
SPECIES
H2 H H2O2 H2O HO2 OH O2 O N2
END
REACTIONS
H+O2=O+OH          3.547E+15      -0.406      1.6599E+04
O+H2=H+OH          0.508E+05       2.670       0.6290E+04
H2+OH=H2O+H       0.216E+09       1.510       0.3430E+04
O+H2O=OH+OH       2.970E+06       2.020       1.3400E+04
H2+M=H+H+M
  H2/2.5/ H2O/12/
O+O+M=O2+M
  H2/2.5/ H2O/12/
O+H+M=OH+M
  H2/2.5/ H2O/12/
H+OH+M=H2O+M
  H2/2.5/ H2O/12/
H+O2(+M)=HO2(+M)  1.475E+12       0.600       0.0000E+00
  LOW/6.366E+20 -1.72 524.8/
  TROE/0.8 1E-30 1E+30 1E+100/
  H2/2.0/ H2O/11./ O2/0.78/
HO2+H=H2+O2       1.660E+13       0.000       0.8230E+03
HO2+H=OH+OH       7.079E+13       0.000       2.9500E+02
HO2+O=O2+OH       0.325E+14       0.000       0.0000E+00
HO2+OH=H2O+O2     2.890E+13       0.000      -4.9700E+02
HO2+HO2=H2O2+O2   4.200E+14       0.000       1.1982E+04
  DUPLICATE
HO2+HO2=H2O2+O2   1.300E+11       0.000      -1.6293E+03
  
```

```

DUPLICATE
H2O2(+M)=OH+OH(+M)          2.951E+14      0.000      4.8430E+04
  LOW/1.202E+17 0.0 4.55E+04/
  TROE/0.5 1E-30 1E+30 1E+100/
  H2/2.5/ H2O/12/
H2O2+H=H2O+OH              0.241E+14      0.000      0.3970E+04
H2O2+H=HO2+H2              0.482E+14      0.000      0.7950E+04
H2O2+O=OH+HO2              9.550E+06      2.000      3.9700E+03
H2O2+OH=HO2+H2O           1.000E+12      0.000      0.0000E+00
  DUPLICATE
H2O2+OH=HO2+H2O           5.800E+14      0.000      9.5570E+03
  DUPLICATE
END

```

B.2 Methane Mechanism by Kee et al.

The mechanism by Kee, et al. [47] is used for the methane combustion cases:

```

ELEMENTS H O C N END
SPECIES
H2 O2 H2O H O OH HO2 CO CO2 H2O2 CH4 CH3 CH2 CH CH2O HCO N2
END
REACTIONS          CAL/MOL
CH3+H+M=CH4+M     8.0000E26      -3.000      0.0000E+00
CH4+O2=CH3+HO2    7.9000E13      0.000      5.6000E+04
CH4+H=CH3+H2      2.2000E04      3.000      8.7500E+03
CH4+O=CH3+OH      1.6000E06      2.360      7.4000E+03
CH4+OH=CH3+H2O    1.6000E06      2.100      2.4600E+03
CH3+O=CH2O+H      6.8000E13      0.000      0.0000E+00
CH3+OH=CH2O+H2    1.0000E12      0.000      0.0000E+00
CH3+OH=CH2+H2O    1.5000E13      0.000      5.0000E+03
CH3+H=CH2+H2      9.0000E13      0.000      1.5100E+04
CH2+H=CH+H2       1.4000E19     -2.000      0.0000E+00
CH2+OH=CH2O+H     2.5000E13      0.000      0.0000E+00
CH2+OH=CH+H2O     4.5000E13      0.000      3.0000E+03
CH+O2=HCO+O       3.3000E13      0.000      0.0000E+00
CH+O=CO+H         5.7000E13      0.000      0.0000E+00
CH+OH=HCO+H       3.0000E13      0.000      0.0000E+00
CH+CO2=HCO+CO     3.4000E12      0.000      6.9000E+02
CH2+CO2=CH2O+CO   1.1000E11      0.000      1.0000E+03
CH2+O=CO+H+H      3.0000E13      0.000      0.0000E+00
CH2+O=CO+H2       5.0000E13      0.000      0.0000E+00
CH2+O2=CO2+H+H    1.6000E12      0.000      1.0000E+03
CH2+O2=CH2O+O     5.0000E13      0.000      9.0000E+03
CH2+O2=CO2+H2     6.9000E11      0.000      5.0000E+02
CH2+O2=CO+H2O     1.9000E10      0.000     -1.0000E+03

```

CH2+O2=C0+OH+H	8.6000E10	0.000	-5.0000E+02
CH2+O2=HCO+OH	4.3000E10	0.000	-5.0000E+02
CH2O+OH=HCO+H2O	3.4300E09	1.180	-4.4700E+02
CH2O+H=HCO+H2	2.1900E08	1.770	3.0000E+03
CH2O+M=HCO+H+M	3.3100E16	0.000	8.1000E+04
CH2O+O=HCO+OH	1.8100E13	0.000	3.0820E+03
HCO+OH=C0+H2O	5.0000E12	0.000	0.0000E+00
HCO+M=H+C0+M	1.6000E14	0.000	1.4700E+04
HCO+H=C0+H2	4.0000E13	0.000	0.0000E+00
HCO+O=C02+H	1.0000E13	0.000	0.0000E+00
HCO+O2=H02+C0	3.3000E13	-0.400	0.0000E+00
C0+O+M=C02+M	3.2000E13	0.000	-4.2000E+03
C0+OH=C02+H	1.5100E07	1.300	-7.5800E+02
C0+O2=C02+O	1.6000E13	0.000	4.1000E+04
H02+C0=C02+OH	5.8000E13	0.000	2.2934E+04
H2+O2=2OH	1.7000E13	0.000	4.7780E+04
OH+H2=H2O+H	1.1700E09	1.300	3.6260E+03
H+O2=OH+O	5.1300E16	-0.816	1.6507E+04
O+H2=OH+H	1.8000E10	1.000	8.8260E+03
H+O2+M=H02+M	3.6100E17	-0.720	0.0000E+00
H2O/18.6/ C02/4.2/ H2/2.86/ C0/2.11/ N2/1.26/			
OH+H02=H2O+O2	7.5000E12	0.000	0.0000E+00
H+H02=2OH	1.4000E14	0.000	1.0730E+03
O+H02=O2+OH	1.4000E13	0.000	1.0730E+0
2OH=O+H2O	6.0000E08	1.300	0.0000E+00
H+H+M=H2+M	1.000E18	-1.000	0.0000E+00
H+H+H2=H2+H2	9.2000E16	-0.600	0.0000E+00
H+H+H2O=H2+H2O	6.0000E19	-1.250	0.0000E+00
H+H+C02=H2+C02	5.4900E20	-2.000	0.0000E+00
H+OH+M=H2O+M	1.6000E22	-2.000	0.0000E+00
H2O/5.0/			
H+O+M=OH+M	6.2000E16	-0.600	0.0000E+00
H2O/5.0/			
H+H02=H2+O2	1.2500E13	0.000	0.0000E+00
H02+H02=H2O2+O2	2.0000E12	0.000	0.0000E+00
H2O2+M=OH+OH+M	1.3000E17	0.000	4.5500E+04
H2O2+H=H02+H2	1.6000E12	0.000	3.8000E+03
H2O2+OH=H2O+H02	1.0000E13	0.000	1.8000E+03
END			

Bibliography

- [1] R.G. Abdel-Gayed, D. Bradley, and A.K.C. Lau. The straining of premixed turbulent flames. In *Symposium (International) on Combustion*, volume 22, pages 731–738. Elsevier, 1989.
- [2] G.E. Andrews, D. Bradley, and S.B. Lwakabamba. Turbulence and turbulent flame propagation—a critical appraisal. *Combustion and Flame*, 24:285–304, 1975.
- [3] G.K. Batchelor. *An Introduction to Fluid Dynamics*. Cambridge University Press, 1967.
- [4] M. Baum, T.J. Poinso, D.C. Haworth, and N. Darabiha. Direct numerical simulation of $\text{H}_2/\text{O}_2/\text{N}_2$ flames with complex chemistry in two-dimensional turbulent flows. *Journal of Fluid Mechanics*, 281(1):1–32, 1994.
- [5] R.S. Blumenthal, P. Subramanian, R.I. Sujith, and W. Polifke. Novel perspectives on the dynamics of premixed flames. *Combustion and Flame*, 160(7):1215–1224, 2013.
- [6] H. Bonart. Implementation and validation of a solver for direct numerical simulations of turbulent reacting flows in OpenFOAM. Bachelor’s thesis, Karlsruhe Institute of Technology, Germany, 2012. URN: [urn:nbn:de:swb:90-374468](https://nbn-resolving.org/urn:nbn:de:swb:90-374468).
- [7] R. Borghi. On the structure and morphology of turbulent premixed flames. In *Recent advances in the Aerospace Sciences*, pages 117–138. Springer, 1985.
- [8] D. Bradley. How fast can we burn? In *Symposium (International) on Combustion*, volume 24, pages 247–262. Elsevier, 1992.
- [9] D. Bradley, P.H. Gaskell, and X.J. Gu. Burning velocities, markstein lengths, and flame quenching for spherical methane-air flames: a computational study. *Combustion and Flame*, 104(1):176–198, 1996.
- [10] D. Bradley, P.H. Gaskell, A. Sedaghat, and X.J. Gu. Generation of pdfs for flame curvature and for flame stretch rate in premixed turbulent combustion. *Combustion and flame*, 135(4):503–523, 2003.
- [11] K.N.C. Bray. Studies of the turbulent burning velocity. In *Proceedings of the Royal Society of London A: Mathematical, Physical and Engineering Sciences*, volume 431, pages 315–335. The Royal Society, 1990.

- [12] K.N.C. Bray and R.S. Cant. Some applications of kolmogorov's turbulence research in the field of combustion. In *Proceedings of the Royal Society of London A: Mathematical, Physical and Engineering Sciences*, volume 434, pages 217–240. The Royal Society, 1991.
- [13] H. Brenner. *Interfacial Transport Processes and Rheology*. Butterworth-Heinemann series in chemical engineering. Elsevier Science, 2013.
- [14] BP energy outlook 2016. Technical report, British Petroleum, 2016.
- [15] T.M. Brown, R.W. Pitz, and C.J. Sung. Oscillatory stretch effects on the structure and extinction of counterflow diffusion flames. In *Symposium (International) on Combustion*, volume 27, pages 703–710. Elsevier, 1998.
- [16] S.M. Candel and T.J Poinso. Flame stretch and the balance equation for the flame area. *Combustion Science and Technology*, 70(1–3):1–15, 1990.
- [17] P. Cermelli, E. Fried, and M.E. Gurtin. Transport relations for surface integrals arising in the formulation of balance laws for evolving fluid interfaces. *Journal of Fluid Mechanics*, 544:339–351, 2005.
- [18] J.B. Chen and H.G. Im. Correlation of flame speed with stretch in turbulent premixed methane/air flames. *Twenty-Seventh Symposium (International) on Combustion*, 27(1):819–826, 1997.
- [19] J.B. Chen and H.G. Im. Stretch effects on the burning velocity of turbulent premixed hydrogen/air flames. *Proceedings of the Combustion Institute*, 28(1):1249–1264, 2000.
- [20] Z. Chen. On the extraction of laminar flame speed and markstein length from outwardly propagating spherical flames. *Combustion and Flame*, 158(2):291–300, 2011.
- [21] E.W. Christiansen, C.K. Law, and C.J. Sung. The role of pulsating instability and global lewis number on the flammability limit of lean heptane/air flames. *Proceedings of the Combustion Institute*, 28(1):807–814, 2000.
- [22] S.H. Chung and C.K. Law. An invariant derivation of flame stretch. *Combustion and Flame*, 55(1):123–125, 1984.
- [23] P. Clavin. Dynamic behavior of premixed flame fronts in laminar and turbulent flows. *Progress in energy and combustion science*, 11(1):1–59, 1985.
- [24] P. Clavin and J.C. Graña-Otero. Curved and stretched flames: the two markstein numbers. *Journal of Fluid Mechanics*, 686:187–217, 2011.

- [25] 2030 climate and energy policy framework. Technical report, Council of the European Union, 2014.
- [26] G. Damköhler. Der Einfluß der Turbulenz auf die Flammengeschwindigkeit in Gasgemischen. *Zeitschrift für Elektrochemie und angewandte physikalische Chemie*, 46(11):601–626, 1940.
- [27] M.S. Day, I.G. Shepherd, Joseph F. Bell, J.G., and M.J. Lijewski. Displacement speeds in turbulent premixed flame simulations. *Lawrence Berkeley National Laboratory*, 2008.
- [28] L.P.H. de Goey, J.A. van Oijen, V.N. Kornilov, and J.H.M. ten Thijsse Boonkamp. Propagation, dynamics and control of laminar premixed flames. *Proceedings of the Combustion Institute*, 33(1):863–886, 2011.
- [29] A. Dziubek. Equations for two-phase flows: a primer. Cornell University Library, 2011.
- [30] T. Echekki and J.H. Chen. Unsteady strain rate and curvature effects in turbulent premixed methane-air flames. *Combustion and Flame*, 106, 1996.
- [31] F.N. Egolfopoulos. Dynamics and structure of unsteady, strained, laminar premixed flames. In *Symposium (International) on Combustion*, volume 25, pages 1365–1373. Elsevier, 1994.
- [32] F.N. Egolfopoulos and C.S. Campbell. Unsteady counterflowing strained diffusion flames: diffusion-limited frequency response. *Journal of Fluid Mechanics*, 318:1–29, 1996.
- [33] A. Fecko. Modern geometry in not-so-high echelons of physics: Case studies. Cornell University Library, 2014.
- [34] R. Gatignol and R. Prud’homme. *Mechanical and Thermodynamical Modeling of Fluid Interfaces*. Series on advances in mathematics for applied sciences. World Scientific, 2001.
- [35] G.K. Giannakopoulos, A. Gatzoulis, C.E. Frouzakis, M. Matalon, and A.G. Tomboulides. Consistent definitions of “flame displacement speed” and “markstein length” for premixed flame propagation. *Combustion and Flame*, 162(4):1249–1264, 2015.
- [36] D.G. Goodwin, H.K. Moffat, and R.L. Speth. Cantera: An object-oriented software toolkit for chemical kinetics, thermodynamics, and transport processes. <http://www.cantera.org>, 2016. Version 2.2.1.

- [37] F. Halter, T. Tahtouh, and C. Mounaïm-Rousselle. Nonlinear effects of stretch on the flame front propagation. *Combustion and Flame*, 157(10):1825–1832, 2010.
- [38] D.C. Haworth, M.C. Drake, S.B. Pope, and R.J. Blint. The importance of time-dependent flame structures in stretched laminar flamelet models for turbulent jet diffusion flames. In *Symposium (International) on Combustion*, volume 22, pages 589–597. Elsevier, 1989.
- [39] High-performance computing center stuttgart CRAY XC40 HAZEL-HEN. www.hlrs.de/en/systems/cray-xc40-hazel-hen, 2016.
- [40] T. Hirasawa, T. Ueda, A. Matsuo, and M. Mizomoto. Response of flame displacement speeds to oscillatory stretch in wall-stagnating flow. *Combustion and flame*, 121(1):312–322, 2000.
- [41] J.O. Hirschfelder, C.F. Curtiss, R.B. Bird, and M.G. Mayer. *Molecular theory of gases and liquids*, volume 26. Wiley New York, 1954.
- [42] H.G. Im and J.H. Chen. Effects of flow transients on the burning velocity of laminar hydrogen/air premixed flames. *Proceedings of the Combustion Institute*, 28(2):1833–1840, 2000.
- [43] Key world energy statistics. Technical report, International Energy Agency, 2015.
- [44] B. Karlovitz, D.W. Denniston, D.H. Knapschaefer, and F.E. Wells. Studies on turbulent flames: A. flame propagation across velocity gradients b. turbulence measurement in flames. In *Symposium (International) on Combustion*, volume 4, pages 613–620. Elsevier, 1953.
- [45] V.P. Karpov and E.S. Severin. Effects of molecular-transport coefficients on the rate of turbulent combustion. *Combustion, Explosion, and Shock Waves*, 16(1):41–46, 1980.
- [46] R.J. Kee, M.E. Coltrin, and P. Glarborg. *Chemically Reacting Flow: Theory and Practice*. Wiley, 2005.
- [47] R.J. Kee, J.F. Grcar, M.D. Smooke, J.A. Miller, and E. Meeks. Sandia report 85-8240. *Sandia National Laboratories*, 1985.
- [48] J.S. Kistler, C.J. Sung, T.G. Kreut, C.K. Law, and M. Nishioka. Extinction of counterflow diffusion flames under velocity oscillations. In *Symposium (International) on Combustion*, volume 26, pages 113–120. Elsevier, 1996.
- [49] K.K. Kuo. *Principles of Combustion*. John Wiley & Sons Inc, 2nd edition, 2005.

- [50] K.K. Kuo and R. Acharya. *Fundamentals of Turbulent and Multiphase Combustion*. John Wiley & Sons Inc, 2012.
- [51] C.K. Law. *Combustion Physics*. Cambridge University Press, 2010.
- [52] C.K. Law, P. Cho, M. Mizomoto, and H. Yoshida. Flame curvature and preferential diffusion in the burning intensity of bunsen flames. In *Symposium (International) on Combustion*, volume 21, pages 1803–1809. Elsevier, 1988.
- [53] C.K. Law and C.J. Sung. Structure, aerodynamics, and geometry of premixed flamelets. *Progress in Energy and Combustion Science*, 26(4–6):459–505, 2000.
- [54] G. Lewis-Dixon. Flame structure and flame reaction kinetics. ii. transport phenomena in multicomponent systems. *Proc. Roy. Soc. A*, 307(1488):111–135, 1968.
- [55] J. Li, Z. Zhao, A. Kazakov, and F.L. Dryer. An updated comprehensive kinetic model of hydrogen combustion. *International Journal of Chemical Kinetics*, 36(10):566–575, 2004. doi:10.1002/kin.20026.
- [56] T.C. Lieuwen. *Unsteady Combustor Physics*. Cambridge University Press, 2012.
- [57] A. Lipatnikov. *Fundamentals of Premixed Turbulent Combustion*. Taylor & Francis, 2012.
- [58] A. Lipatnikov and J. Chomiak. Global stretch effects in premixed turbulent combustion. *Proceedings of the Combustion Institute*, 31(1):1361–1368, 2007.
- [59] A.N. Lipatnikov and J. Chomiak. Molecular transport effects on turbulent flame propagation and structure. *Progress in Energy and Combustion ScienceA*, 31(1):1–73, 2005.
- [60] G.H. Markstein. *Non-steady flame Propagation*. 1964.
- [61] M. Matalon. On flame stretch. *Combustion Science and Technology*, 31(3–4):169–181, 1983.
- [62] M. Matalon and B.J. Matkowsky. Flames as gasdynamic discontinuities. *Journal of Fluid Mechanics*, 124:239–259, 1982.
- [63] B.J. McBride, S. Gordon, and M.A. Reno. *Coefficients for Calculating Thermodynamic and Transport Properties of Individual Species*. National Aeronautics and Space Administration, 1993. NASA Technical Memorandum 4513.
- [64] M. Mehl, H.J. Curran, W.J. Pitz, and C.K. Westbrook. iso-octane, version 3. Lawrence Livermore National Laboratory, 2009.

- [65] A. Melvin and J.B. Moss. Evidence for the failure of the flame stretch concept for premixed flames. *Combustion Science and Technology*, 7(5):189–196, 1973.
- [66] L Monchick and E.A. Mason. Transport properties of polar gases. *J. Chem. Phys.*, 35(5):1676–1697, 1961.
- [67] M. Nakahara and H. Kido. A study of the premixed turbulent combustion mechanism taking the preferential diffusion effect into consideration. *Memoirs of the Faculty of Engineering, Kyushu University*, 58(2):55–82, 1998.
- [68] J. Nearing. *Mathematical tools for physics*. University of Miami, 2010.
- [69] OpenFOAM: The open source CFD toolbox. www.openfoam.com.
- [70] Green growth and the future of aviation. Technical report, Organisation for Economic Co-operation and Development, 2012. 27th Round Table on Sustainable Development.
- [71] N. Peters. *Turbulent Combustion*. Cambridge Monographs on Mechanics. Cambridge University Press, 2000.
- [72] T.J. Poinso. Computational turbulent combustion. CEFRC Combustion Summer School, www.princeton.edu/cefrccombustion-summer-school/archived-programs/2013-session/lecture-videos, 2013.
- [73] T.J. Poinso, T. Echekeki, and M.G. Mungal. A study of the laminar flame tip and implications for premixed turbulent combustion. *Combustion science and technology*, 81(1-3):45–73, 1992.
- [74] T.J. Poinso and S.K. Lelef. Boundary conditions for direct simulations of compressible viscous flows. *Journal of computational physics*, 101(1):104–129, 1992.
- [75] T.J. Poinso and D. Veynante. *Theoretical and Numerical Combustion*. R.T. Edwards, 2001.
- [76] B.E. Poling, J.M. Prausnitz, and J.P. O’Connell. *The Properties of Gases and Liquids*. McGraw Hill Professional, 5th edition, 2004.
- [77] R. Prud’homme. *Flows of Reactive Fluids*. Fluid Mechanics and Its Applications. Birkhäuser Boston, 2010.
- [78] R. Prud’homme. *Flows and Chemical Reactions*. ISTE. Wiley, 2013.
- [79] H.P. Schmid. *Ein Verbrennungsmodell zur Beschreibung der Wärmefreisetzung von vorgemischten turbulenten Flammen*. PhD thesis, Karlsruhe Institute of Technology, 1995.

- [80] L. Selle, T.J. Poinso, and B. Ferret. Experimental and numerical study of the accuracy of flame-speed measurements for methane/air combustion in a slot burner. *Combustion and Flame*, 158(1):146–154, 2011.
- [81] J.O. Sinibaldi, J.F. Driscoll, C.J. Mueller, J.M. Donbar, and C.D. Carter. Propagation speeds and stretch rates measured along wrinkled flames to assess the theory of flame stretch. *Combustion and flame*, 133(3):323–334, 2003.
- [82] Steinbruch centre for computing forschungshochleistungsrechner forHLR II. www.scc.kit.edu/dienste/forhldr2.php, 2016.
- [83] SUNDIALS: Suite of nonlinear and differential/algebraic equation solvers. <http://computation.llnl.gov/casc/sundials/main.html>.
- [84] C.J. Sung and C.K. Law. Ignition of oscillatory counterflowing nonpremixed hydrogen against heated air. *Combustion science and technology*, 129(1-6):347–370, 1997.
- [85] C.J. Sung and C.K. Law. Structural sensitivity, response, and extinction of diffusion and premixed flames in oscillating counterflow. *Combustion and flame*, 123(3):375–388, 2000.
- [86] C.J. Sung, A. Makino, and C.K. Law. On stretch-affected pulsating instability in rich hydrogen/air flames: asymptotic analysis and computation. *Combustion and flame*, 128(4):422–434, 2002.
- [87] T. Tahtouh, F. Halter, and C. Mounaïm-Rousselle. Measurement of laminar burning speeds and markstein lengths using a novel methodology. *Combustion and Flame*, 156(9):1735–1743, 2009.
- [88] T. Takaiishi, A. Numata, R. Nakano, and K. Sakaguchi. Approach to high efficiency diesel and gas engines. Technical report, Mitsubishi Heavy Industries, Ltd, 2008. Technical Review Vol. 45 No. 1.
- [89] H. Tennekes and J.L. Lumley. *A First Course in Turbulence*. Pe Men Book Company, 1972.
- [90] J.H. Tien and M. Matalon. On the burning velocity of stretched flames. *Combustion and Flame*, 84(3):238–248, 1991.
- [91] K. Tsuboi, R. Matsugi, and E. Tomita. Evaluation of the local burning velocity using DNS data of turbulent premixed flames. *Natural Science*, 2014, 2014.
- [92] S.R. Turns. *An introduction to combustion: concepts and applications*. McGraw-Hill, 2007.

- [93] H.Y. Wang, C.K. Law, and T. Lieuwen. Linear response of stretch-affected premixed flames to flow oscillations. *Combustion and flame*, 156(4):889–895, 2009.
- [94] M. Weiß. *Untersuchung von Flammenfrontstreckungseffekten auf die sphärische Flammenausbreitung laminarer und turbulenter Brennstoff/Luft-Gemische*. PhD thesis, Karlsruhe Institute of Technology, 2008. Universitätsverlag Karlsruhe.
- [95] M. Weiß, N. Zarzalis, and R. Suntz. Experimental study of markstein number effects on laminar flamelet velocity in turbulent premixed flames. *Combustion and Flame*, 154(4):671–691, 2008.
- [96] H.G. Weller, G. Tabor, H. Jasak, and C. Fureby. A tensorial approach to computational continuum mechanics using object-oriented techniques. *Computers in physics*, 12(6):620–631, 1998.
- [97] G. Williams. *Combustion theory*. Citeseer, 2nd edition, 1985.
- [98] F. Wu, W. Liang, Z. Chen, Y. Ju, and C.K. Law. Uncertainty in stretch extrapolation of laminar flame speed from expanding spherical flames. *Proceedings of the Combustion Institute*, 35, 2015.
- [99] T. Yokomori and M. Mizomoto. Flame temperatures along a laminar premixed flame with a non-uniform stretch rate. *Combustion and flame*, 135(4):489–502, 2003.
- [100] K.M. Yu, C.J. Sung, and C.K. Law. Some aspects of the freely propagating premixed flame in a spatially periodic flow field. *Combustion and flame*, 97(3-4):375–383, 1994.
- [101] F. Zhang, H. Bonart, T. Zirwes, P. Habisreuther, H. Bockhorn, and N. Zarzalis. Direct numerical simulation of chemically reacting flows with the public domain code OpenFOAM. In W.E. Nagel, D.H. Kröner, and M.M. Resch, editors, *High Performance Computing in Science and Engineering '14*, pages 221–236. Springer International Publishing, 2015.
- [102] T. Zirwes. Weiterentwicklung und Optimierung eines auf OpenFOAM basierten DNS Löser zur Verbesserung der Effizienz und Handhabung. Bachelor's thesis, Karlsruhe Institute of Technology, Germany, 2013. URN: [urn:nbn:de:swb:90-375385](https://nbn-resolving.org/urn:nbn:de:swb:90-375385).